REPORT DOCUMENTATION PAGE		Form Approved OMB NO. 0704-0188

1. REPORT DATE (DD-MM-YYYY) 29-06-2016	2. REPORT TYPE Final Report	3. DATES COVERED (From - To) 29-Feb-2012 - 29-Feb-2016

4. TITLE AND SUBTITLE	5a. CONTRACT NUMBER
Final Report: A New Route Toward Systematic Control of Electronic Structures of Graphene and Fabrication of Graphene Field Effect Transistors	W911NF-12-1-0071
	5b. GRANT NUMBER
	5c. PROGRAM ELEMENT NUMBER 206022

6. AUTHORS	5d. PROJECT NUMBER
Nezih Pala	
	5e. TASK NUMBER
	5f. WORK UNIT NUMBER

7. PERFORMING ORGANIZATION NAMES AND ADDRESSES	8. PERFORMING ORGANIZATION REPORT NUMBER
Florida International University Office of Research & Economic Development 11200 SW 8th Street Miami, FL 33199 -0001	

9. SPONSORING/MONITORING AGENCY NAME(S) AND ADDRESS (ES)	10. SPONSOR/MONITOR'S ACRONYM(S) ARO
U.S. Army Research Office P.O. Box 12211 Research Triangle Park, NC 27709-2211	11. SPONSOR/MONITOR'S REPORT NUMBER(S) 60534-EL-REP.27

12. DISTRIBUTION AVAILIBILITY STATEMENT

Approved for Public Release; Distribution Unlimited

13. SUPPLEMENTARY NOTES

14. ABSTRACT

This project aims to (i) control graphene electronic structure by perturbing it using nanoparticles; (ii) fabricate graphene field-effect transistors and demonstrate their superior performances; (iii) investigate the THz and sub-THz characteristics of graphene layers.

We have demonstrated engineering the bandgap of single layer Graphene by decorating with randomly distributed zinc oxide (ZnO) and gold nanoparticles. The proximity of nanoparticles and Graphene break Graphene's sublattice symmetry and opens up a bandgap. Graphene with significant bandgap introduced by the proposed methods could

15. SUBJECT TERMS

Graphene, Field Effect Transistors, Sensors

16. SECURITY CLASSIFICATION OF:			17. LIMITATION OF ABSTRACT	15. NUMBER OF PAGES	19a. NAME OF RESPONSIBLE PERSON Nezih Pala
a. REPORT UU	b. ABSTRACT UU	c. THIS PAGE UU	UU		19b. TELEPHONE NUMBER 305-348-3016

Report Title

Final Report: A New Route Toward Systematic Control of Electronic Structures of Graphene and Fabrication of Graphene Field Effect Transistors

ABSTRACT

This project aims to (i) control graphene electronic structure by perturbing it using nanoparticles; (ii) fabricate graphene field-effect transistors and demonstrate their superior performances; (iii) investigate the THz and sub-THz characteristics of graphene layers.
We have demonstrated engineering the bandgap of single layer Graphene by decorating with randomly distributed zinc oxide (ZnO) and gold nanoparticles. The proximity of nanoparticles and Graphene break Graphene's sublattice symmetry and opens-up a bandgap. Graphene with significant bandgap introduced by the proposed methods could be used for devices intended for high speed digital and logic applications.
We also demonstrated a novel geometry field effect transistor with graphene as channel having a hybrid contact that consists of ohmic Source/Drain and its extended part towards the Gate, which is capacitively coupled to the channel. Minimization of access region length along with the paralleling of ohmic contact's resistance and resistive part of capacitively coupled contact's impedance lower the overall Source/Drain resistance, which results in an increases current gain cut-off frequency.
We also performed theoretical investigation of graphene based FET structures for resonant absorption of THz radiation by the plasmons excited in the high sheet concentration and high carrier mobility active layers.

Enter List of papers submitted or published that acknowledge ARO support from the start of the project to the date of this printing. List the papers, including journal references, in the following categories:

(a) Papers published in peer-reviewed journals (N/A for none)

<u>Received</u>   <u>Paper</u>

08/27/2014 7.00 Duyoung Choi, Cihan Kuru, Chulmin Choi, Kunbae Noh, Soon-Kook Hong, Santanu Das, Wonbong Choi, Sungho Jin. Nanopatterned Graphene Field Effect Transistor Fabricated Using Block Co-polymer Lithography,
Materials Research letters, (01 2014): 0. doi: 10.1080/21663831.2013.876676

08/27/2014 13.00 Phani Kiran Vabbina, Ajeet Kaushik, Nimesh Pokhrel, Shekhar Bhansali, Nezih Pala. Electrochemical cortisol immunosensors based on sonochemically synthesized zinc oxide 1D nanorods and 2D nanoflakes,
Biosensors and Bioelectronics, (01 2015): 0. doi: 10.1016/j.bios.2014.07.026

08/27/2014 12.00 Michael Shur, Mustafa Karabiyik, Chowdhury Al-Amin, Nezih Pala, Phani Kiran Vabbina, Santanu Das, Wonbong Choi, Tanuj Saxena. Controlled Synthesis of Single-Crystalline ZnO Nanoflakes on Arbitrary Substrates at Ambient Conditions,
Particle & Particle Systems Characterization, (02 2014): 0. doi: 10.1002/ppsc.201300208

08/27/2014 11.00 Phani Kiran Vabbina, Mustafa Karabiyik, Raju Sinha, Nezih Pala, Wongbong Choi, Chowdhury Al-Amin. Improving High-Frequency Characteristics of Graphene FETs by Field-Controlling Electrodes,
IEEE Electron Device Letters, (09 2013): 0. doi: 10.1109/LED.2013.2272071

08/27/2014 10.00 C. Al-Amin, M. Karabiyik, P.K. Vabbina, R. Sinha, N. Pala. Field controlled RF Graphene FETs with improved high frequency performance,
Solid-State Electronics, (05 2014): 0. doi: 10.1016/j.sse.2014.03.003

08/27/2014 9.00 Santanu Das, Debrupa Lahiri, Arvind Agarwal, Wonbong Choi. Interfacial bonding characteristics between graphene and dielectric substrates,
Nanotechnology, (01 2014): 0. doi: 10.1088/0957-4484/25/4/045707

08/27/2014 8.00 Santanu Das, Moonkyung Kim, Jo-won Lee, Wonbong Choi. Synthesis, Properties, and Applications of 2-D Materials: A Comprehensive Review,
Critical Reviews in Solid State and Materials Sciences, (04 2014): 231. doi: 10.1080/10408436. 2013.836075

08/29/2013 2.00 C. Al-Amin, N. Pala, M. Karabiyik. Deep Sub-Wavelength Multimode Tunable In-Plane Plasmonic Lenses Operating at Terahertz Frequencies,
IEEE Transactions on Terahertz Science and Technology, (09 2013): 0. doi: 10.1109/TTHZ. 2013.2273415

08/31/2015 16.00 Santanu Das, Wonbong Choi, Nezih Pala, Nitin Choudhary, Al-Amin. Chowdhury, Raju Sinha, Mustafa Karabiyik, PhaniKiran Vabbina. Highly Sensitive Wide Bandwidth Photodetector Based on Internal Photoemission in CVD Grown p-Type MoS,
ACS Applied Materials & Interfaces, (07 2015): 15206. doi: 10.1021/acsami.5b00887

08/31/2015 17.00 Duyoung Choi, Cihan Kuru, Chulmin Choi, Kunbae Noh, Sookhyun Hwang, Wonbong Choi, Sungho Jin. Unusually High Optical Transparency in Hexagonal Nanopatterned Graphene with Enhanced Conductivity by Chemical Doping,
Small, (07 2015): 3143. doi: 10.1002/smll.201402784

TOTAL: 10

Number of Papers published in peer-reviewed journals:

(b) Papers published in non-peer-reviewed journals (N/A for none)

Received   Paper

       TOTAL:

Number of Papers published in non peer-reviewed journals:

(c) Presentations

Number of Presentations: 0.00

Non Peer-Reviewed Conference Proceeding publications (other than abstracts):

Received   Paper

06/24/2016 23.00 . Numerical analysis of terahertz plasmonic ring resonators,
                   SPIE Defense, Security, and Sensing. 22-APR-14, Baltimore, Maryland, USA. : ,

06/24/2016 24.00 . Dispersion studies in THz plasmonic devices with cavities,
                   SPIE Sensing Technology + Applications. 22-APR-14, Baltimore, Maryland, USA. : ,

06/24/2016 25.00 . Bandgap engineering of graphene decorated with randomly distributed ZnO nano-seed,
                   SPIE Defense + Security. 20-APR-16, Baltimore, Maryland, United States. : ,

       TOTAL: **3**

Number of Non Peer-Reviewed Conference Proceeding publications (other than abstracts):

Peer-Reviewed Conference Proceeding publications (other than abstracts):

<u>Received</u>   <u>Paper</u>

06/24/2016 14.00 Chowdhury Al-Amin, Raju Sinha, Nezih Pala, Wonbong Choi. Novel graphene FETs with field-controlling
electrodes to improve RF performance,
SPIE Defense + Security. 22-APR-14, Baltimore, Maryland, USA. : ,

06/24/2016 15.00 Phani Kiran Vabbina, Ajeet Kaushik, Kathryn Tracy, Shekhar Bhansali, Nezih Pala. Zinc oxide
nanostructures for electrochemical cortisol biosensing,
SPIE Sensing Technology + Applications. 22-MAY-14, Baltimore, Maryland, USA. : ,

06/24/2016 18.00 Chowdhury Al-Amin, Mustafa Karabiyik, Raju Sinha, Nezih Pala. Lowering contact resistance of graphene
FETs with capacitive extension of ohmic contacts for enhanced RF performance,
SPIE Defense + Security. 20-APR-15, Baltimore, Maryland, United States. : ,

   TOTAL: **3**

Number of Peer-Reviewed Conference Proceeding publications (other than abstracts):

(d) Manuscripts

<u>Received</u>   <u>Paper</u>

   TOTAL:

Number of Manuscripts:

Books

<u>Received</u>   <u>Book</u>

   TOTAL:

TOTAL:

Patents Submitted

Patents Awarded

Awards

Best Graduate Student Paper Award in Nanomaterials (3rd place)
P. Bhadrachalam, R. Subramanian, K. Cho, J. Kim, S.J. Koh, "Effect of Phonon Emission and Absorption in Electron Tunneling through Double Quantum Dots", TMS Annual Meeting, San Antonio, Texas, March 2013

Chowdhury Al-Amin
1st place in Electrical and Computer Engineering at the 2013 Florida International University Scholarly Forum, March 2013

Chowdhury Al-Amin
Award for Distinguished Scientific Contributions to the First Statewide Graduate Student Research Symposium at University of South Florida, April 2013

Graduate Students

NAME	PERCENT_SUPPORTED	Discipline
Chowdhury Al-Amin	0.80	
Santanu Das	0.40	
Pradeep Bhadrachalam	0.20	
Phani Kiran Vabbina	0.60	
FTE Equivalent:	**2.00**	
Total Number:	**4**	

Names of Post Doctorates

NAME	PERCENT_SUPPORTED
FTE Equivalent:	
Total Number:	

Names of Faculty Supported

NAME	PERCENT_SUPPORTED	National Academy Member
Nezih Pala	0.14	
Won Bong Choi	0.01	
FTE Equivalent:	**0.15**	
Total Number:	**2**	

Names of Under Graduate students supported

NAME	PERCENT_SUPPORTED	Discipline
Meilyn Planas	0.00	Electrical Engineering
FTE Equivalent:	**0.00**	
Total Number:	**1**	

Student Metrics
This section only applies to graduating undergraduates supported by this agreement in this reporting period

The number of undergraduates funded by this agreement who graduated during this period: 1.00

The number of undergraduates funded by this agreement who graduated during this period with a degree in science, mathematics, engineering, or technology fields:...... 1.00

The number of undergraduates funded by your agreement who graduated during this period and will continue to pursue a graduate or Ph.D. degree in science, mathematics, engineering, or technology fields:...... 1.00

Number of graduating undergraduates who achieved a 3.5 GPA to 4.0 (4.0 max scale):...... 1.00

Number of graduating undergraduates funded by a DoD funded Center of Excellence grant for Education, Research and Engineering:...... 0.00

The number of undergraduates funded by your agreement who graduated during this period and intend to work for the Department of Defense 1.00

The number of undergraduates funded by your agreement who graduated during this period and will receive scholarships or fellowships for further studies in science, mathematics, engineering or technology fields:...... 0.00

Names of Personnel receiving masters degrees

NAME
Total Number:

Names of personnel receiving PHDs

NAME
Chowdhury Al-Amin
Pani Kirna Vabbina
Santanu Das
Total Number: 3

Names of other research staff

NAME	PERCENT_SUPPORTED
FTE Equivalent:	
Total Number:	

Sub Contractors (DD882)

1 a. University of North Texas   **1 b.** 1155 Union Circle #305250

Denton   TX   762035017

Sub Contractor Numbers (c): 800001753-02

Patent Clause Number (d-1):

Patent Date (d-2):

Work Description (e): Systematic control of electronic structure of graphenes by using controlled synthesis tech

Sub Contract Award Date (f-1): 12/6/12 12:00AM

Sub Contract Est Completion Date(f-2): 10/1/14 12:00AM

---

1 a. University of North Texas   **1 b.** Office of Sponsored Projects

PO Box 305250

Denton   TX   762035017

Sub Contractor Numbers (c): 800001753-02

Patent Clause Number (d-1):

Patent Date (d-2):

Work Description (e): Systematic control of electronic structure of graphenes by using controlled synthesis tech

Sub Contract Award Date (f-1): 12/6/12 12:00AM

Sub Contract Est Completion Date(f-2): 10/1/14 12:00AM

---

1 a. University of Texas at Arlington   **1 b.** Grant and Contract Services

701 South Nedderman Drive

Arlington   TX   760190145

Sub Contractor Numbers (c): 800001753-01

Patent Clause Number (d-1):

Patent Date (d-2):

Work Description (e): Develop a new technique that enables systematic control of electronic structure of graphe

Sub Contract Award Date (f-1): 4/25/12 12:00AM

Sub Contract Est Completion Date(f-2): 2/28/14 12:00AM

---

1 a. University of Texas at Arlington   **1 b.** P. O. Box 19145

Arlington   TX   760190145

Sub Contractor Numbers (c): 800001753-01

Patent Clause Number (d-1):

Patent Date (d-2):

Work Description (e): Develop a new technique that enables systematic control of electronic structure of graphe

Sub Contract Award Date (f-1): 4/25/12 12:00AM

Sub Contract Est Completion Date(f-2): 2/28/14 12:00AM

Inventions (DD882)

Scientific Progress

See Attachment

Technology Transfer

N/A

ARO Grant # W911NF-12-1-0071

A New Route toward Systematic Control of Electronic Structures of Graphene and Fabrication of Graphene Field Effect Transistors

Final Report
May 31, 2016

Nezih Pala, PI
Florida International University

This page is intentionally left blank

Abstract

The primary objective of this research effort is to investigate reliable techniques of controlling energy bandgap of graphene with an ultimate goal of realizing integrated circuit of graphene based electronic devices and plasmonic properties for possible THz applications. Graphene has attracted considerable attention due to its unique electrical and optical properties in the recent years. However, there exists one critical obstacle that has so far prevented the graphene from being implemented into electronic device applications; the pristine graphene do not have band gaps that are essential for switching and transistor operation. We will tackled this challenge by systematically attaching nanoparticles on a graphene surface. With the capability of systematic bandgap control, we aimed at fabricating graphene-FETs and investigate their electrical characteristics, with an ultimate goal of realizing integrated circuits of graphene-based transistors. Superior charge transport properties of graphene can be exploited to fabricate very high speed FETs for conventional digital switching and radiofrequency (RF) applications as well as novel THz plasmonic applications to meet the needs of DoD's future electronics. Specifically, this project targeted the following objectives:

1. Develop a new technique that enables systematic control of electronic structure of graphenes. Specifically, demonstrate that the band gap of graphenes can be created and controlled by placement of nanoparticles on a graphene and/or creation of nano-scale holes (antidots) through electrical perforation.
2. Investigate electrical and optical properties of the synthesized graphene layers with band gap. High field transport properties, which have not been studied for large-area graphenes so until now, will particularly be studied.
3. Fabricate graphene field-effect transistors and detectors and demonstrate their superior performances.
4. Investigate the THz characteristics of the synthesized graphene layers and explore their potential for THz applications.

During the course of the project we completed the following studies
1. Developed graphene synthesis, transfer, processing, integration with other 2D materials (e.g. MoS_2) and characterization techniques
2. Demonstrated unusually high optical transparency in hexagonal nanopatterned graphene with enhanced conductivity by chemical doping
3. Demonstrated graphene band gap opening by decoration with nanoparticles.
4. Designed and studied graphene FETs with low-resistance hybrid contacts for improved high frequency performance
5. Investigated graphene plasmonic devices and metasurfaces for THz
6. Demonstrated highly sensitive wide bandwidth photodetector based on internal photoemission in CVD grown p-type MoS2/graphene Schottky junction

This project resulted 18 journal and 6 conference papers and provided supports for 4 graduate students.

Table of Contents

3. Scientific Progress

Graphene, a monolayer of sp^2-bonded carbon atoms in a honeycomb crystal lattice, has attracted considerable attention due to its unique electrical and optical properties.[1,2] Intrinsic graphene is a semi-metal or zero bandgap semiconductor and it's unique electronic properties produce an unexpectedly high opacity for an atomic monolayer, with a startling absorbance ratio of 2.3% of white light.[3] Electrical characterization has shown a remarkably high electron mobility at room temperature, with experimentally reported values in excess of 15,000 $cm^2V^{-1}s^{-1}$. The corresponding resistivity of the graphene sheet would be 10^{-6} Ohm−cm, less than the resistivity of silver, the lowest resistivity substance known at room temperature.[4] The graphene also has extremely high saturation density of electrons and holes; a sheet electron/hole density on the order of 10^{13} cm^{-2} can be easily obtained, which is more than one order of magnitude higher than that found in conventional semiconductor materials.[4] Due to its exceptional electrical property, graphene has been attracted for future electronics such as ballistic transistors, components of integrated circuits, transparent conducting electrodes and an efficient sensor. Graphene has a high electron (or hole) mobility as well as low noise characteristics, ideal properties for the channel in a FET. Its 2D structure, when combined with its excellent electrical property and low noise characteristics, makes graphene an excellent sensor - its entire volume is exposed to the surrounding, making detection of adsorbed molecules extremely efficient. The high electrical conductivity and high optical transparency make graphene a candidate for transparent conducting electrodes, required for applications such as touch-screens, liquid crystal displays, organic photovoltaic cells and OLEDs.

Despite many attractive features above, however, there exists one critical obstacle that has so far prevented the graphenes from being implemented into electronic device applications; the pristine graphenes do not have band gaps that are essential for switching and transistor operation. The gapless energy spectrum of graphene is obstacle for creating transistor digital circuits based on graphene-FETs due to the nature of ambipolar behavior and relatively strong interband tunneling in the FET off-state,[5,6,7] resulting in poor on/off ratios. Creating the band gap in the graphene electronic structure has therefore been one of the central research efforts. One major approach has been to perturb the graphene electronic structure through confinement effect, such as in graphene nanoribbons.[8,9,10] The band gap creation from this approach, however, is difficult to control since the electronic structure of the graphene nanoribbons is very sensitive to their width, edge geometry,

---

[1] Chen, J. H. et al. "Intrinsic and Extrinsic Performance Limits of Graphene Devices on SiO$_2$", *Nature Nanotech*, Vol. 3, pp. 206-209 (2008).

[2] "Carbon Wonderland", *Scientific American*, April 2008.

[3] R. R. Nair, P. Blake, A. N. Grigorenko, K. S. Novoselov, T. J. Booth, T. Stauber, N. M. R. Peres, A. K. Geim "Fine Structure Constant Defines Visual Transparency of Graphene", *Science* **320**: 1308, (2008).. doi:10.1126/science.1156965

[4] A.K.Geim, K.S.Novoselov, *Nature Mater.,* Vol. 6, pp. 183-91, (2007).

[5] V. Ryzhii *et al*., *Appl. Phys. Exp*. Vol. 1, p. 013001 (2008).

[6] V. Ryzhii *et al*., *J. Appl. Phys*. Vol. 103, p. 094510 (2008).

[7] V. Ryzhii *et al*., *Phys. Stat. Solidi (a)* Vol. 205, p.1527 (2008).

[8] K. Nakada *et al*. *Phys. Rev. B* Vol. 54, 17954 (1996).

[9] B. Obradovic *et al*., *Appl. Phys. Lett*. Vol. 88, 142102 (2006).

[10] G. Liang et al.: IEEE Trans. Electron Devices Vol. 54, 677 (2007).

and chemical functionalization.[11] Another approach is to use graphene bilayers,[12,13,14] which is known to open the energy bandgap. The other approach relies on creation of defects on a graphene layer, either through adsorption of atoms/molecules or creation of antidots.[11, 15] The bandgap opening may degrade the electron transport properties; its energy dispersion becomes parabolic, yielding a non-zero effective mass. Therefore, an optimum condition –reliable bandgap opening - needs to be systematically studied.

Superior charge transport properties of graphene can be exploited to fabricate very high speed FETs for both conventional digital switching and radiofrequency (RF) applications as well as novel THz plasmonic applications. An ideal FET for digital applications must have excellent switching capabilities which are usually characterized by subthreshold swing, S and large transconductance g_m, as well as a large on/off current ratio. In a conventional FET these requirements are provided by a semiconducting channel with a non-zero finite bandgap. However, as it was mentioned above, the zero bandgap of large area graphene precludes the creation of high speed graphene-FETs for digital applications. Despite this major challenge, graphene and related devices are considered to be a promising solution for the post-CMOS era. Indeed, the latest ITRS roadmap strongly recommends intensified research into graphene and even contains a research and development schedule for carbon- based nanoelectronics.[16] For RF applications, although a large on/off current ratio is not required, saturation of drain current is essential to achieve maximum possible operating frequencies. This requirement is not satisfied in large area graphene, again, because of the lack of a band gap.

Apart from the conventional FETs (digital and RF) which are limited by the transient time of carriers, a new family of devices which exploit the high frequency of collective oscillations of charge carrier densities (plasmons) in a 2D layers have been proposed. The resonant frequency of plasmons in graphene layers corresponds to THz frequencies which would allow tunable detection and filtering of THz radiation. Terahertz technologies utilize electromagnetic radiation in the frequency range between 300 GHz and 10 THz. Potential applications for terahertz technology in biology, chemistry, medicine, astronomy and security are wide ranging. THz wavelengths have several properties that could promote their use as sensing and imaging tool. THz radiation can penetrate non-metallic materials such as fabric, leather and plastic which makes it useful in security screening for concealed weapons and they do not cause ionization which could be hazardous for biological tissues. [17] The THz frequencies correspond to energy levels of molecular rotations and vibrations of DNA[18] and proteins,[19] as well as explosives,[20] and these may provide characteristic fingerprints to differentiate biological tissues in a region of the spectrum not previously explored for medical use or detect and identify trace amount of explosives. THz

[11] Balog, R. *et al. Nature Materials* **9**, 315-319 (2010).
[12] T. Ohta *et al.*, *Science* Vol. 313, 951 (2006).
[13] E. McCann, *Phys. Rev. B* 74, 161403(R) (2006).
[14] J.B. Oostinga *et al.*, *Nature Mat.* Vol.7, 151 (2008).
[15] T. G. Pedersen, *et al. Phys. Rev. Lett.* 100, 136804 (2008).
[16] *The International Technology Roadmap for Semiconductors* http://www.itrs.net/Links/2009ITRS/Home2009.htm (Semiconductor Industry Association, 2009).
[17] D. Arnone, *et al.*, *Physics World*, pp. 35–40, (2000).
[18] A. Markelz, *et al.*, *Chemical Physics Letters*, Vol. 320, pp. 42–48, (2000).
[19] M. Walther, *et al.*, *Chemical Physics Letters*, Vol. 332, pp. 389–395, (2000).
[20] Hai-Bo Liu, *et al.*, *Optics Express*, Vol. 14, Issue 1, pp. 415-423

radiation has also been used in the characterization of semiconductor materials,[21,22,23] and in testing and failure analysis of VLSI circuits.[24,25] THz frequencies are also very attractive for communication applications for the large bandwidth at these frequencies which could provide very high data transmission rates. On the down side, strong atmospheric absorption due to the water vapor together with the low available power of the current THz sources limits the range of communication. The strong atmospheric attenuation, however, does not pose a real threat for a number of communication applications. Space communication, for instance, can benefit from the high data transmission rates and smaller antenna size required for THz frequencies which would make possible the development of smaller, lighter therefore satellites with longer lifetime. Large bandwidth of THz frequencies can also be used to for short-range indoor communication exceeding Gigabit/s transmission rates. Rayleigh scattering of electromagnetic radiation is many orders of magnitude less for THz wavelengths than for the alternative infrared frequencies. One unique and promising potential for THz frequencies is the on-chip and communication, especially systems-on-chip (SoC) applications. With the ever increasing complexity of integrated circuits, larger and larger number of functional and storage cores are squeezed into a single die. Interconnect delays do not scale as well as local wires with respect to gate delays and global interconnects have and increasing impact on the performance of overall SoCs. A radical alternative to the existing metal/dielectric interconnect infrastructures is to use transmission of signals via wireless interconnects. If the THz frequencies are employed for on-chip communication, corresponding antenna sizes decrease occupying much less chip real estate. Nanowires and carbon nanotubes (CNTs) can serve as antenna structures in such applications. CNT bundles are predicted to enhance performance of antenna modules by up to 40dB in radiation efficiency and provide excellent directional properties in far field patterns and can achieve a bandwidth of 500GHz and hence can achieve much higher data rates.

This completed research tackled the above described challnges. During the course of the project we completed the following studies

1. Developed graphene synthesis, transfer, processing, integration with other 2D materials (e.g. MoS_2) and characterization techniques
2. Demonstrated unusually high optical transparency in hexagonal nanopatterned graphene with enhanced conductivity by chemical doping
3. Demonstrated graphene band gap opening by decoration with nanoparticles.
4. Designed and studied graphene FETs with low-resistance hybrid contacts for improved high frequency performance
5. Investigated graphene plasmonic devices and metasurfaces for THz
6. Demonstrated highly sensitive wide bandwidth photodetector based on internal photoemission in CVD grown p-type MoS2/graphene Schottky junction

This project resulted 18 journal and 6 conference papers and provided supports for 4 graduate students.

---

[21] S. D. Ganichev, *et al.*, *Materials Science in Semiconductor Processing*, vol. 4, pp. 281-284,(2001).

[22] D. M. Mittleman, *et al.*, *Applied Physics Letters*, vol. 71, pp. 16-18, (1997).

[23] W. Zhang, *et al.*, *Applied Physics Letters*, vol. 82, pp. 2841-3, (2003).

[24] W. Stillman, *et al.*, IEEE Sensors 2007 The 6th IEEE Conference on Sensors, Atlanta, GA October 28-31, 2007

[25] M. Yamashita, *et al.*, *Optics Express*, vol. 13, pp. 115-120, (2005).

3.1 Graphene Synthesis, Transfer, Processing and Characterization Techniques

3.1.1 Growth and Characterization of Layer and Grain Controlled Graphene

Graphene has been proposed as a material for heat dissipation owing to its extremely high thermal conductivity. It was reported that the incorporation of graphene or few-layer graphene (FLG) layers with proper heat sinks can substantially lower the temperature of the localized hot spots. If studied critically, the number of graphene layer transferred to the substrate could significantly affect the adhesion properties. There may be a trade-off between the thermal conductivity and adhesion forces depending on the number of graphene layers used. Therefore, it is important to optimize growth of graphene exhibiting the best thermal and mechanical properties simultaneously.

To address this issue, Dr. Choi's team used two types of thermal chemical vapor deposition (CVD) systems to control the growth of graphene sheets: low pressure CVD (LPCVD) (Figure 3.1.1a) and atmospheric pressure CVD (APCVD) (Figure 3.1.1b). Commercial grade Cu foils (99.9% Purity, 25-50 µm-thick, NIMROD Hall) were electropolished using a home-built electrochemistry cell to suppress nucleation sites (Figure 3.1.1c). The ambience of LPCVD furnace was kept under the constant flow of inert gas (Ar) and $CH_4 : H_2$ (ranging from 1:5 to 1:50) was used as a precursor gas mixture for graphene growth at 1000°C–1035°C for 5 to 60 minutes. After the furnace was cooled down to room temperatures as following our own cooling process, the samples were taken out for further structural characterizations and transfer process.

Figure 3.1.1: (a) LPCVD and **(b)** APCVD systems for graphene growth. **(c)** Photograph of Cu foils before/after electropolishing.

We have studied the effect of process parameters on the growth of graphene on polycrystalline Cu by LPCVD. To promote the graphene nucleation, we performed experiments where we used the different growth process. As shown in Figure 3.1.2, grain sizes and surface coverage of graphene over Cu substrate were increased as well as the number of graphene layers could be controlled by our growth process.
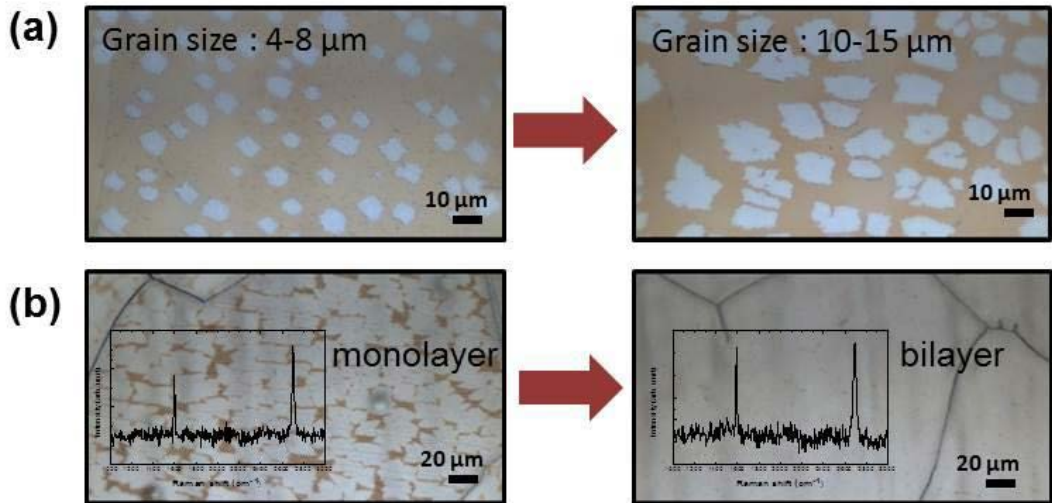
Figure 3.1.2: Optical images of partially grown graphene under different growth condition. Scale bars are 20 μm in **(a)** and 10 μm in **(b)**, respectively. Inset in **(b):** Raman spectra of graphene on Cu substrate.

There are several factors like roughness, surface bonding, defects and grain boundaries presented in the graphene layers which simultaneously affect the electrical, thermal and mechanical properties of graphene and therefore significant correlations could be established among them.

Figure 3.1.3 shows the SThM images of as-transferred graphene for thermal analysis; wrinkle formation of graphene is unavoidable during various processes involved in device fabrication and will degrade the electrical and thermal conductivity of graphene due to charge trapping and scattering in wrinkles. High thermal contrast between wrinkles and sheet is observed in figure 3.1.3 (b). Since the wrinkles exhibit high temperature throughout graphene surface, it is important to eliminate them as much as possible for an efficient heat removal.
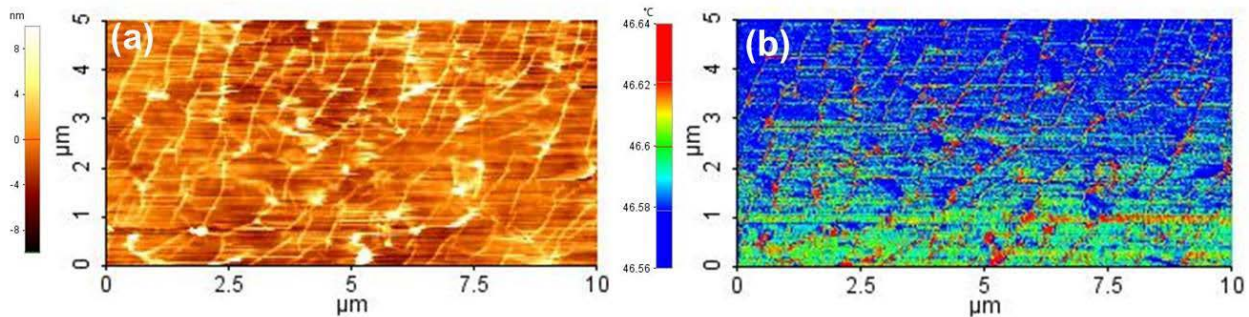

Figure 3.1.3: (a) Topography and **(b)** thermal image of as-transferred graphene by SThM.

5
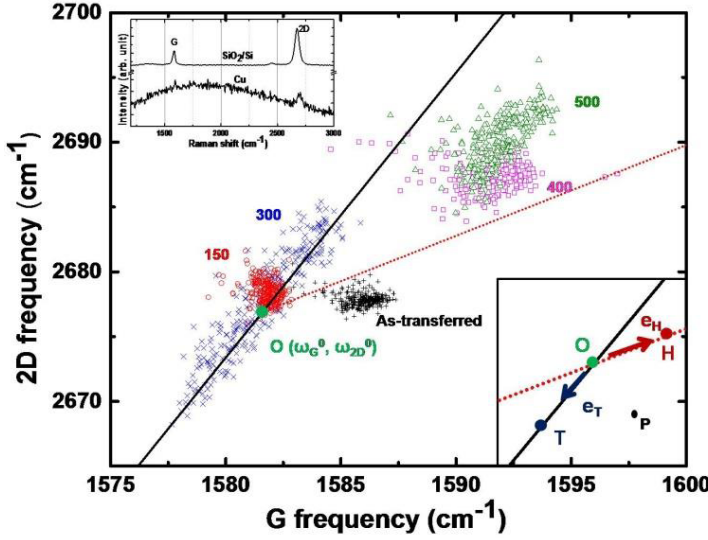
Figure 3.1.4: Raman spectral analysis of graphene on SiO_2/Si substrate before and after annealing, ranging from 150°C to 500°C in vacuum. The green circle (denoted **O**) obtained from a free standing graphene sample represents ($\omega_{G0}, \omega_{2D0}$) no strain or charge doping. The black line represents a prediction of (ω_G, ω_{2D}) for charge-neutral graphene under randomly oriented uniaxial stress. The red dashed line is an average of experimental (ω_G, ω_{2D}) for strain-free graphene with varying density of holes (n). Lower inset: decomposition of the effects of hole doping and strain using a vector model. Any given (ω_G, ω_{2D}), **OP**, can be decomposed into **OH** along the 'strain-free' unit vector, **e$_H$** for hole doping, and **OT** along the 'charge-neutral' unit vector, **e$_T$** for tensile strain (-**e$_T$** for compressive strain), respectively. Upper inset: Raman spectra of graphene grains on Cu foil and transferred onto SiO_2/Si substrate.

We further studied the effect of interfacial strain induced at graphene/substrate on heat spreading by Raman spectroscopy. Figure 3.1.4 shows the correlation between the frequencies of the G(ω_G) and 2D(ω_{2D}) modes obtained from transferred graphene with annealing temperature, ranging from room temperature to 500ºC. The green circle (denoted O**)** in Figure 3.1.4 indicates the average of 2D and G frequencies ($\omega_{G0}, \omega_{2D0}$) of a freestanding graphene (1581.6 ± 0.2, 2676.9 ± 0.7), which is free from strain or charge doping. It is shown that hundreds of data points from an as-transferred graphene sample on SiO_2/Si placed in the range between (1585.8±1.6, 2678.0±1.7), mostly along OH axis, representing oxygen doping and the same for strain. Namely, as-transferred sample may be slightly affected by oxygen or moisture during transfer process. Accordingly slight tensile strain is sustained in graphene, which can be attributed to the transfer process of PMMA coating and removing. As annealing temperature increased, the data points shifted towards **eH** vector for hole doping and –eT vector for compressive strain. Therefore, during annealing the transferred graphene releases its tensile strain and undergoes compression, as well as introduce hole doping in graphene.

3.1.2 Transfer of Graphene on to SiO_x /Si and Glass

Thermal CVD grown graphene on Cu foil was placed floated on a Cu etchant ($FeCl_3$) in order to etch away the Cu foil. The total time required for etching of Cu foil is 40 min and 20 min for 54 μm and 25 μm Cu foil respectively. The floated graphene on the top of the $FeCl_3$ solution was transferred carefully on a FTO substrate subsequently washing with water, acetone, and IPA as shown in schematic Figure 3.1.5a. Figure 3.1.5d and e demonstrates the picture of FTO glass

before and after graphene transfer respectively. Similarly, the same floated graphene samples can be transferred on to any other dielectric substrates like Al_2O_3, SiO_2/Si, quartz and sapphire.
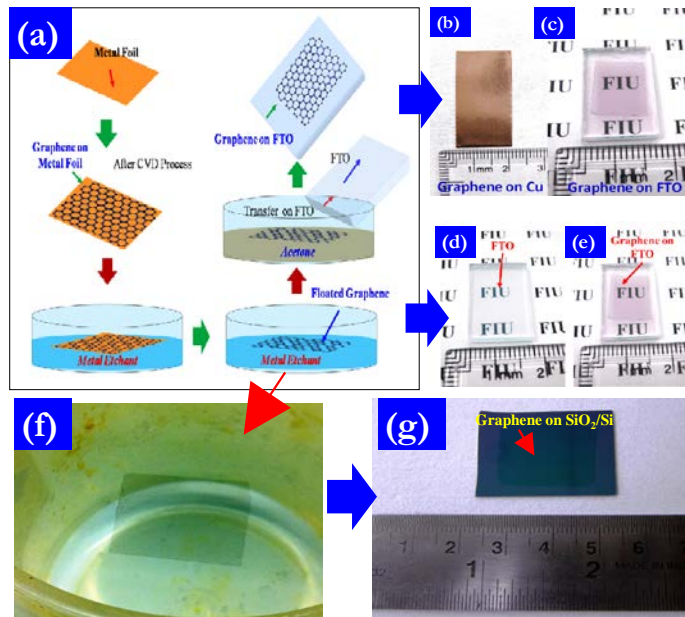

Figure 3.1.5: Chemical transfer of graphene on different substrates: **(a)** schematic represents the process flow charts of the chemical transfer of graphene from metal substrates to any other substrates. **(b)** Graphene grown on Cu foil; **(c)** graphene transfer on glass substrates using chemical transfer process; **(d) & (e)** illustrates the glass substrates before and after graphene transfer respectively; **(f)** floated graphene on water; **(g)** transferred graphene layers on SiO_2(300 nm)/Si substrates as large as 40 mm x 30 mm.

3.1.3 Interfacial Bonding Characteristics Between Graphene and Dielectric Substrate

Achieving strong adhesion between graphene and Si/SiO_2 substrates is crucial to make reliable graphene based electronics and electro-optic devices. We report the enhanced adhesion energy by vacuum annealing and its quantification of graphene-SiO_x/Si substrate adhesion energy by using the nanoscratch technique coupled with Raman spectroscopy and X-ray photoelectron spectroscopy (XPS). We found that the adhesion energy of as transferred graphene on SiO_x/Si substrate is ~ 2.978 Jm^{-2}. By applying different annealing protocols of rapid thermal annealing (RTA) and vacuum annealing (VA), the adhesion energy of graphene - SiO_x/Si is increased to 10.09 and 20.64 Jm^{-2}, respectively. The increase in adhesion energy is owing to the formation of chemical bonds between the graphene and SiO_x at high temperature.

3.1.4 Nanoscratch Study

Nano-scratch studies were carried out at the sharp interfaces of graphene-SiO_x/Si substrates (as shown in Figure 3.1.6) to measure the adhesion energy using a standard Berkovich tip. In brief, nano-scratch technique is a high precision nano-scale scratching methodology where each scratch is started from the bare substrate and move over the graphene interface inside the graphene region. Indenter tip encounters almost constant counter force when travelling through the bare substrate, which arises from the counter force exerted on the tip required to disintegrate the atomic bonds in substrate. Nonetheless, when indenter tip starts penetrating the graphene interface, the lateral force

starts increasing which is due to the additional force required to peel off graphene layers from the substrate surface and/or disintegrating of the graphene. It is clearly shown that the indenter-tip started travelling from the bare substrate and continued through the graphene region. Graphene is entirely peeled off from the substrate and repositioned at the side of the scratch. During the nano-scratch experiment, indenter tip was positioned approximately 5 μm away from the interface and allowed to travel up to 10 μm inside of the graphene region which creates a total scratch length of 15 μm. The additional lateral force encountered by the indenter tip during travelling inside the graphene region consists of three basic domain; graphene-substrate bonds, graphene-graphene interlayer van der Waals bonds and inter-planar carbon-carbon (C-C) bonds. Furthermore, the energy required for breaking the interlayer van der Waals bonds and in plane C-C bonds were deducted from the total measured de-bonding energy. Thus, the resultant de-bonding energy was divided by the nano-scratch area which results in a graphene-substrate adhesion energy per unit area.
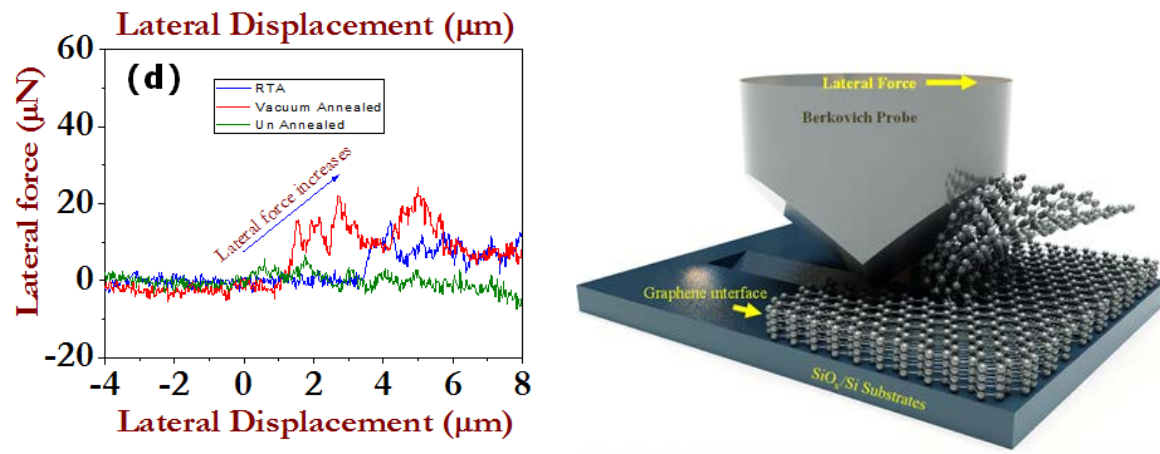

Figure 3.1.6: Characteristics load vs. displacement plots of an unannealed, rapidly thermal annealed and vacuum annealed graphene on SiO_x/Si respectively. The highest adhesion energy of vacuum annealed graphene on SiO_2/Si compared to the others is shown in this figure.

Figure 3.1.6 delinated the lateral force vs. displacement curves for three different samples of unannealed (UA), RTA and vacuum annealed (VA) graphene on SiO_x/Si, respectively. For the UA-graphene the change in the lateral force is almost negligible which reflects the presence of weak bonding such as van der Waals bonds. In contrast, the F-D curve for RTA and VA graphene shows a considerable changes in lateral force. This sharp distinction between annealed and un annealed graphene revealed that chemical bond formation occurred due to chemical interactions among the interfacial C and O at elevated temperature. Figure 3.1.6 shows the highest adhesion energy of VA graphene compared to the RTA and UA graphene. Our calculation shows that the adhesion energy of UA-graphene, RTA-graphene and VA-graphene is 2.978 Jm^{-2} (± 1.24 Jm^{-2}), 10.04 Jm^{-2} (± 4.05 Jm^{-2}) and 20.64 Jm^{-2} (± 7.04 Jm^{-2}) respectively. Henceforth, the results shows that the 3 fold and 7 fold increase in adhesion energy of RTA graphene and VA graphene respectively compared to the UA graphene. We believe that this enhancements in the graphene substrate adhesion energy are due to the formation of chemical bonds associated with several interfacial chemical and structural reconstructions between graphene and SiO_x.
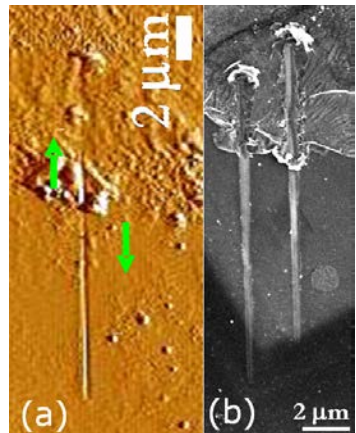
Figure 3.1.7: (a) Scanning probe micrograph (SEM) of a single nanoscratch at the boundary of graphene-SiO$_2$/Si showing that the nanoscratch started at the bare surface and penetrate all the way through the graphene layer, scraping graphene layers from the surface. **(b)** SEM shows the the nano-scratched region at the graphene-SiO$_x$/Si boundary.

3.1.5 Fabrication of Electrostatic Guiding Structure for Controlled Placement of Single Nanoparticles

In our approach, the Au nanoparticles (AuNPs) are placed by electrostatically guiding them to the desired substrate positions. Here, the design of the electrostatic guiding structure is important to place the AuNPs on a single-particle level (that is, to place exactly one nanoparticle to a target position). To investigate the effect of electrostatic guiding structure on single-particle-level placement, we fabricated model electrostatic guiding structures using e-beam lithography and associated pattern definition techniques. Figure 3.1.8 shows some of these patterns fabricated. Using these model structures, we are currently studying the effect of the dimension of the guiding structure (e.g., hole sizes, pitches between the holes) on nanoparticle-substrate interactions.


(a)   (b)
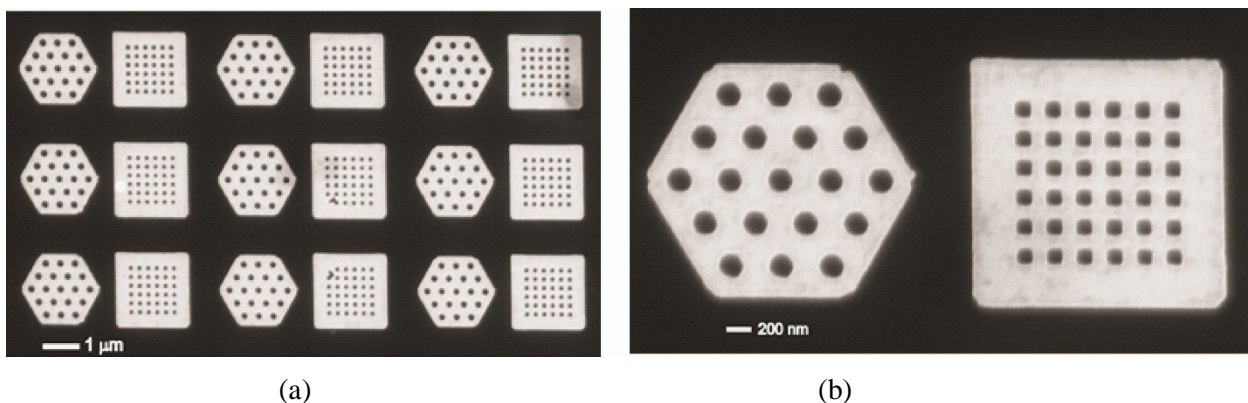
Figure 3.1.8: SEM images of electrostatic guiding structures for single-particle-level placement of nanoparticles. Bright areas: Au; Dark areas: SiO$_2$.

9

3.1.6 Study of Formation of Self-Assembled Monolayers (SAMs) to Control Electrostatic Charges on the Patterned Surface Structure

In our approach, the nanoparticle placement is carried out by controlling the electrostatic interactions between the substrate structure and the (charged) nanoparticles. The surface charges on the guiding structures are manipulated by forming self-assembled monolayers (SAMs) of organic molecules having different charge states. For the silicon oxide area, we functionalize the surface using positively charged molecules, 3-aminopropyltriethoxysilane (APTES: $(C_2H_5O)_3$-Si-$(CH_2)_3$-NH_2). The APTES SAMs are positively charges in aqueous solution and attracts negatively charged nanoparticles; schematic in Fig. 3.1.9(a). It turned out that the formation of APTES SAMs is complicated and requires well-controlled process parameters, such as the nature of solvent, water content in a solvent, rinsing conditions, post-curing procedure, etc. We have been investigating the effect of these parameters and are optimizing the best conditions for the APTES SAMs formation. Figure 3.1.9(b) shows an SEM image demonstrating AuNP attachment on a SiO_2 substrate that was properly functionalized with APTES SAMs.


<center>(a)   (b)</center>
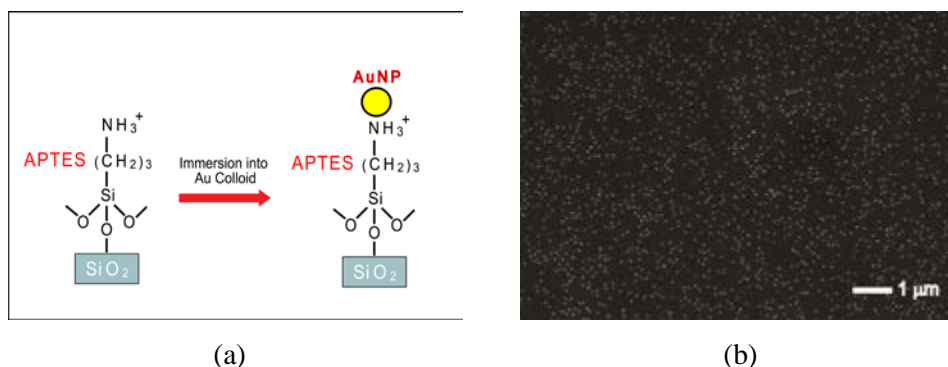
Figure 18.1.9: Formation of APTES SAMs and AuNP attachment. **(a)** A schematic for APTES SA formed on a SiO_2 substrate and AuNP attachment on it. **(b)** SEM image showing the AuNP (30 n attachment on APTES-functionalized SiO_2 substrate.

3.1.7 Control of the Electrostatic Charge of Nanoparticles using DNA Conjugation

The nanoparticle placement can be engineered by controlling the electrostatic interactions between the charged nanoparticles and functionalized substrate guiding patterns. To control the amount of the electrical charges on the AuNP surface, we utilized single-stranded DNA (ssDNA) to functionalize AuNP surfaces. Since DNA is negatively charged through its phosphate backbone, we aim to control the total charge of an AuNP by adjusting the amount of ssDNA attached on a AuNP. Figure 3.1.10 shows a schematic of functionalizing AuNPs using ssDNA. We first functionalized the AuNPs with FSN ($F(CF_2CF_2)_{3-8}CH_2CH_2O(CH_2CH_2O)_xH$), Fig. 3.1.10 (b). Then, the thiolated ssDNA was introduced, which replaced some portion of FSN on the AuNP surface, Fig. 3.1.10 (c). We controlled the amount of ssDNA attached on a AuNP by adjusting the NaCl concentration in the conjugation solution; higher NaCl concentration led to higher number of ssDNA on AuNP due to reduced electrostatic repulsion between ssDNA molecules (through ion screening). The DNA-conjugated AuNPs were stable and did not suffer any agglomerations.

<center>10</center>
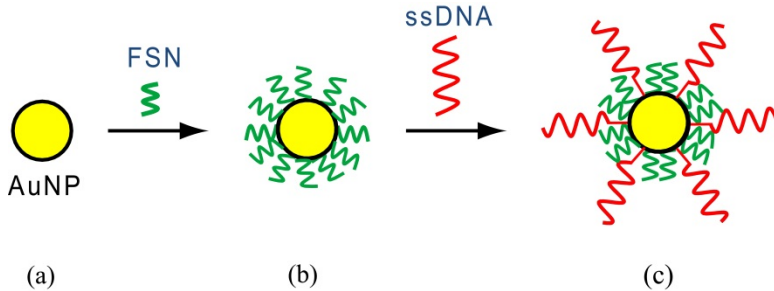
Figure 3.1.10: Control of nanoparticle charges using DNA conjugation. (a) AuNP coated with citric or tannic acid. (b) Introduction of FSN replaces the citric/tannic acid, producing FSN coated AuNPS. (c) Introduction of thiol-terminated ss-DNA replaces a portion of FSN molecules, producing ss-DNA/AuNP conjugates.

3.1.8 Synthesis of large scale and thickness modulated MoS2

Two dimensional (2D) MoS_2 is a promising material for next-generation electronic and optoelectronic devices due to its unique properties of large bandgap, good mobility and quantum confinement that results in high current on/off ratios and ultra-low power dissipation while providing transparency and flexibility. The transition from an indirect bandgap in the bulk to a direct bandgap in monolayer MoS_2 open avenues for engineering energy bandgaps. Although MoS_2 has shown excellent properties, wafer scale production with layer control from single to few layers has yet to be demonstrated. The present study explored the large scale and thickness-modulated growth of atomically thin MoS_2 on Si/SiO_2 substrates. Our process exhibited wafer-scale fabrication and successful thickness modulation of MoS_2 layers from monolayer (0.72nm) to multilayer (12.69nm) with high uniformity. Electrical measurements on MoS_2 field effect transistors (FETs) revealed a p-type semiconductor behavior with much higher field effect mobility and current on/off ratio as compared to previously reported MoS_2-FETs and commercially available amorphous silicon (a-Si) thin film transistors. Our results show that sputter-CVD is a viable method to synthesize large area, high quality MoS2 atomic layers that can be adapted in conventional Si-based microfabrication technology and future flexible, high temperature and radiation-hard electronics/optoelectronics.
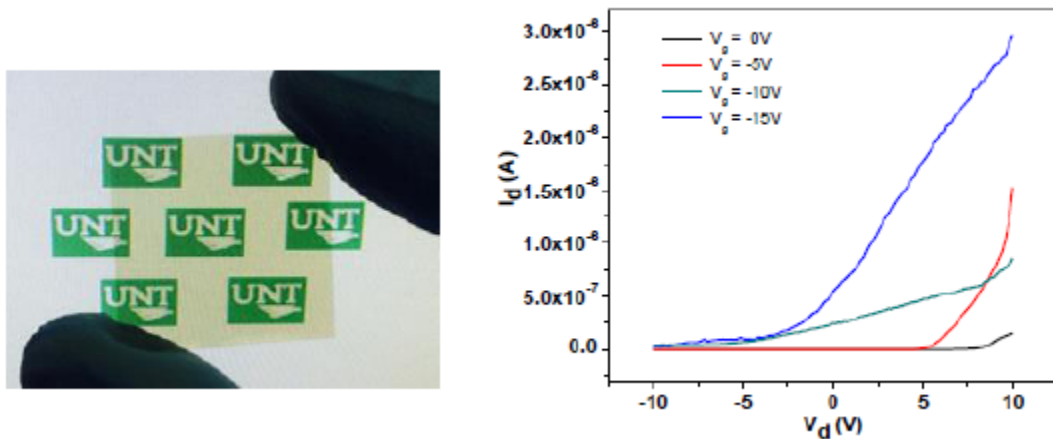

Figure 3.1.11: Large scale MoS2 film synthesized by thermal CVD method and its IV characteristic

3.1.9 Controlled Synthesis of Single-Crystalline ZnO Nanoflakes on Arbitrary Substrates at Ambient Conditions

Semiconductor nanostructures have attracted considerable research interest due to their peculiar physical properties and potential applications in electronics and energy related devices. In this regard, Zinc Oxide (ZnO) nanostructures have received particular attention for many potential applications such as light emitting and detection devices in UV-Visible spectral range, electromecahnical coupled sensors, transducers and energy generators for nano devices. ZnO nanostructures also finds its applications in gas sensors, optoelectronics devices and biomedical applications. Considering the promising properties and potential applications of ZnO nanoparticles, many techniques have been developed to synthesize various 1D-ZnO nanostructures such as rods, belts, tubes etc. However, there has been limited reports on synthesis of two dimensional (2D) ZnO nanostructures and there is a lack of thorough understanding of synthesis mechanism and systematic control over the synthesis process. On the other hand, sonochemical method promises to be a good alternative to synthesize nanostructures at ambient conditions. The method is rapid, inexpensive, low-temperature catalyst-free process, CMOS compatible and environmentally benign. However, most of the effort in sonochemical synthesis so far has been focused on synthesizing 1D ZnO nanostructures such as nanorods and nanoribbons and to our knowledge no report is available on sonochemistry based synthesis of morphology controlled 2D ZnO nanoflakes on different substrates.

We studied the synthesis of single-crystalline 2D ZnO nanoflake structures using a simple sonochemical reaction in aqueous solutions on arbitrary substrates at ambient conditions. We used Si, graphene/Si and graphene/PET as the substrates for 2D morphology controlled ZnO nanostructure growth. Graphene is a 2D carbon nanostructure which has been studied extensively in recent years due its remarkable mechanical, optical and electronic properties. These properties makes graphene a promising candidate for many potential applications including electronic and optical devices. Graphene electrodes with nanostructures can also be applied as synergistic electrodes for different flexible and transparent conducting devices. The growth mechanism of the synthesized 2D ZnO nanostructures is studied in detail with the help of scanning electron microscopy (SEM), high resolution transmission electron microscopy (HRTEM) and selected area electron diffraction (SAED). Based on the data we believe that ZnO nanoflakes are oriented along (0001) plane and grow laterally along $(01\bar{1}0)$ plane. Furthermore, the electrical and optical data show excellent conduction and transmission properties respectively. Our synthesis method is a low cost, low temperature, scalable and potentially high throughput process which can be further extended for the synthesis of wide range of other 2D materials for different applications in electronics and optoelectronics devices.

We used Zinc nitrate hexahydrate (ZNH, $Zn(NO_3).6H_2O$) and hexamethylenetetramine (HMT, $(CH_2)_6.N_4$) (both from Sigma Aldrich) for sonochemical synthesis of ZnO nanoflakes. ZNH provides Zn^{2+} ions and H_2O molecules in the solution provide O^{2-} ions. HMT has been used as a shape inducing polymer in ZnO nanowire growth as polymer as it attaches to the non-polar facets of ZnO cutting the supply of Zn^{2+} ions, thus allowing the growth of ZnO in only <0001> direction. However the shape of the nanostructures strongly depend on the concentration of ZNH/HMT solutions which affects the precipitation mechanism of the oxide. It was observed that as the concentration of ZNH/HMT aqueous solution increased the length of the ZnO nanorods decreased. In the present case, the concentration of the precursors is increased by 10-20 times and the

sonication amplitude is increased by 20% compared to the earlier process. The process temperature does not exceed 70 $^{\circ}$C, as amplitude of the sonication is increased. At the higher concentrations used in this process and fast reaction rates achieved under sonication, HMT releases large amounts of OH$^-$ and NH^{4+} ions in a short period of time. At this higher concentrations, precipitation of Zn^{2+} ions occurs at faster rate than required for HMT assisted oriented growth of ZnO nanostructures resulting in growth of non-polar planes of ZnO along with polar (0001) plane forming parallelogram shaped 2D ZnO nanoflakes.
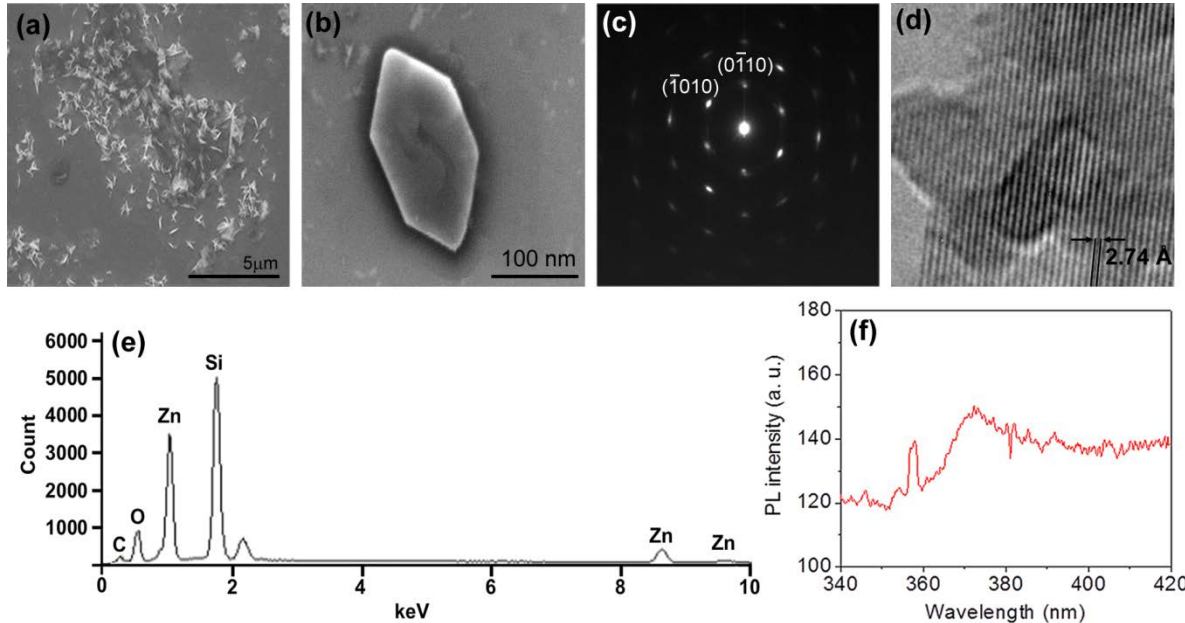

Figure 3.1.12: **(a)** ZnO sheet structures grown on Si substrate at 30 seconds, **(b)** After 1 minute hexagonal structures are observed. **(c)** SAED pattern shows a single-crystalline wurtzite structure oriented in <0001> direction and lateral growth direction perpendicular to $(0\bar{1}10)$ **(d)** HRTEM at the edge of flake with fringes almost parallel to the edge and fringe spacing of 2.74 Å which is close to 2.82 Å of $(10\bar{1}0)$ plane **(e)** EDS data for ZnO nanoflakes which shows that the grown nanoflakes are purely ZnO. **(f)** PL spectrum of the ZnO nanoflakes on Graphene shows a peak at 376 nm which is agreement with the bandgap of ZnO. The peak intensity is not strong since the flakes are extremely thin.

Fig. 3.1.12(a-b) show the SEM pictures of the ZnO nanoflake growth on Si substrate at 30 seconds and 1 minute. 2D ZnO nanoflakes grow from sheet structures to hexagonal crystal structure which further stabilizes into parallelogram-like structures. To further understand the growth mechanism of nanoflakes, detailed SAED and HRTEM studies were performed using an electron microscope with 300 KeV electron beam. The SAED analysis is carried out using commercial software (Single Crystal). The SAED pattern in Fig. 3.1.12 (c) and HRTEM picture in Fig. 3.1.12 (d) confirm the single-crystalline wurtzite structure of the 2D ZnO nanoflakes oriented in [0001] direction. The HRTEM images are taken at the major edge of the flake show that the fringes are almost parallel to the edge with a lattice spacing of 2.74 Å. The lattice spacing is a representative of $(10\bar{1}0)$ plane which corresponds to the longest edge. The SAED measurements indicate that the 2D ZnO nanoflakes exhibit hexagonal wurtzite structure with a = 3.25 Å and c = 5.21 Å, oriented along (0001) plane and lateral growth direction perpendicular to the $(01\bar{1}0)$ plane. The elemental composition of the nanoflakes is verified by EDS data presented in Fig. 3.1.12 (e) which shows that the nanoflakes are purely ZnO with no observed impurities. The small carbon peak observed

in EDS is from the carbon deposition during SEM measurement setup. Furthermore, photoluminescence (PL) spectra of ZnO nanoflakes on Graphene shown in Fig. 3.1.12(f) presents an emission line at 376 nm which is characteristic for ZnO. The peak is relatively low due to extremely thin nature of the nanoflakes. The 376 nm PL peak is attributed to the free-exciton annihilation in ZnO. The PL system used in this study upconverts the frequency (harmonic conversion) from green light at 532 nm which causes high intensity stray green light making it difficult to observe green PL emission due to traps. However, deep-level or trap-state emission at around 530 nm, related to the recombination of electrons in singly occupied oxygen vacanices with photo-excited holes in the valence band has been reported by Vaneusden et al.

We increase the synthesis time from 1 min. to 1 hour for different samples keeping the cycles to one to study the growth dynamics of the flakes. The morphologies of the samples were investigated using JEOL 7000 FSEM and Multimode Nanoscope IIID AFM from Bruker (Veeco). Fig. 3.1.13 (a-d) show the time evolution of the growth process for ZnO nanoflakes on Si substrate at 1 min., 3 min., 15 min. and 30 min. Based on the SEM, HRTEM and SAED data, we infer that the growth rates are varied with different directions result in the growth process which could be depicted in Fig. 3.1.13 (e). Initially the ZnO sheets are self-organized in hexagonal single-crystalline structures and the crystal continues to grow in the direction of $(01\bar{1}0)$ plane forming a more stable parallelogram shaped structure with the surface normal in <0001> orientation and longest edge in $(10\bar{1}0)$ plane. For the pronlonged time of synthesis, flakes do not grow in lateral directions beyond amaximum average dimension but new flakes are formed over the old ones forming a multi-layer stack. Fig. 3.1.13 (f) summarizes the change of dimension and thickness of the flakes by the growth period. The change in the thickness with respect to growth time was measured by using AFM while lateral dimensions are measured by SEM. Sizes of several flakes have been averaged to have statistically reliable data. The thickness of the nanoflake layer varies from 15 nm of single flake to 300 nm of a stack several of several flakes for a growth time of 10 minutes and 2 cycles of 30 minutes, respectively. However, the thickness of a single nanoflake remains constant around 15-20 nm irrespective of the time of synthesis as shown in Fig. 3.1.13 (f). This is in agreement with the process described above and the mechanism shown in Fig. 3.1.13 (e). The dimensions of the largest 2D ZnO nanoflake increase rapidly from 0.76 µm for growth time of 1 minute to ~10 µm at 15 minutes and remain the same as the time is increased. Furthermore, from Fig. 3.1.13 (d) we can see that the density of the nanostructures increases with the number of cycles, while the dimensions varied with the sonochemical reaction time. Therefore by controlling the time and cycles of synthesis the dimensions, thickness and density of 2D ZnO nanoflakes can be controlled efficiently using the method of sonochemical reactions which solely depends upon the solution pH, concentration, time and power.

Three different samples were prepared to study the I-V characteristics of single nanoflake and their variation with respect to thickness. First sample Z-3 has the growth time of 3 minutes, sample Z-5 has 5 minutes, and sample Z-15 has the growth time of 15 minutes. In order to study the conductivity of the individual flakes, electrical contacts were deposited using a focused ion beam (FIB) and I-V characteristics were measured using a probe station (The Micromanipulator and results analyzed by Semiconductor parameter analyzer, Model No. Agilent 4156 A) attached with Micromanipulator tip (model 7A-M). As shown in the Fig. 3.1.13(g), I-V curves slightly superlinear behavior and the conductivity increases with the increasing thickness of nanoflakes which increases as the synthesis time increases. Superlinear behavior is attributed to space-charge-

limited current (SCLC) which is commonly observed in nanostructures of various materials including ZnO nanowires. When the number of carriers injected from contacts are greater than the free carriers in the semiconductors, the current is limited by the buildup of injected space charge. Since SCLC is sensitive to the density of trap states, and their energy depth, it can be prominently observed 2D structures with large surface to volume ratio. Another sample was prepared by 3 cycles of 15 minutes giving a continuous film of nanoflakes over SiO_2/Si substrate to measure the photoconductivity. Fig. 3.1.13(h) presents the current-voltage characteristics in dark and under the illumination of 360 nm UV light. We observe more than 10 fold increase in conductivity in the presence of UV light confirming the photoconductive nature of ZnO nanoflakes.
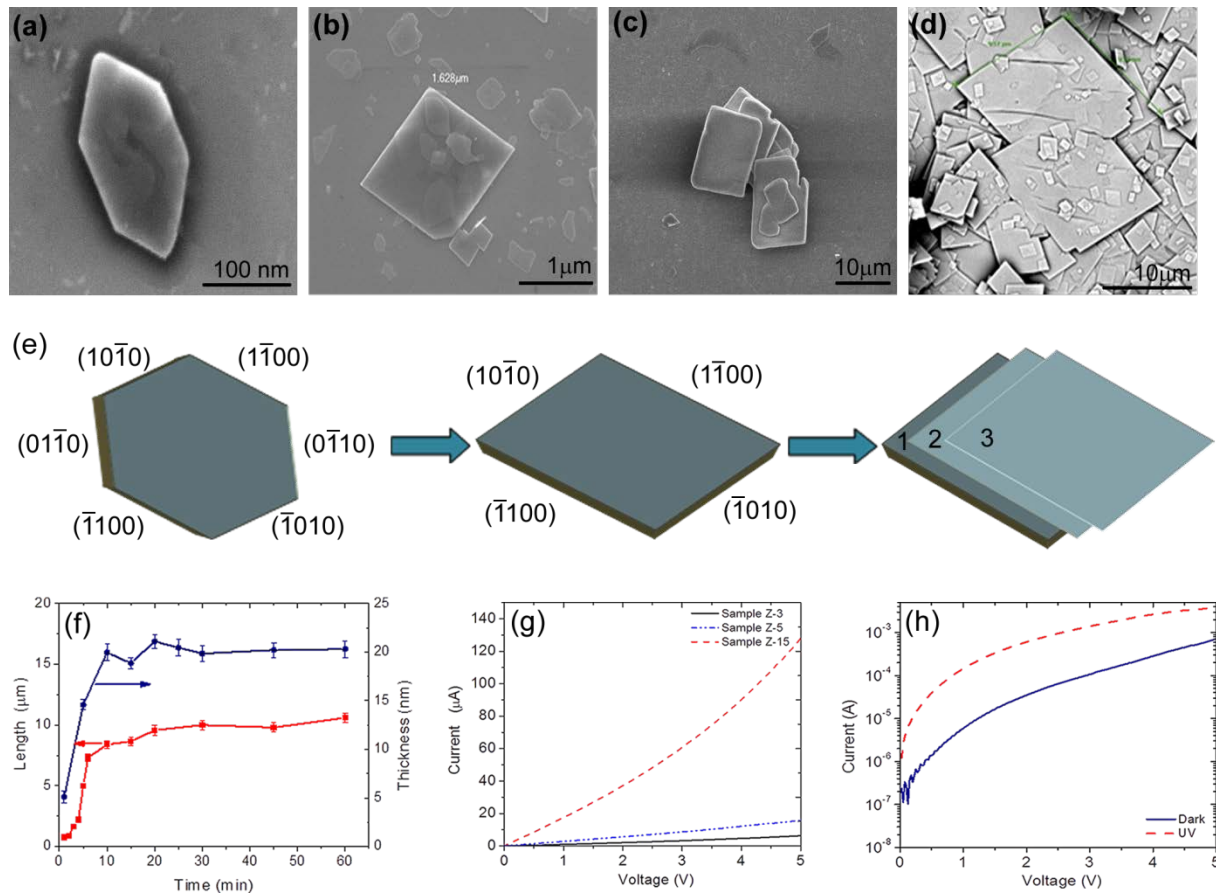

Figure 3.1.13: Size of flakes grown on Si substrate over the time **(a)** After 1 minute hexagonal structures are observed. **(b)** After 3 minutes of synthesis the crystal forms in to a parallelogram structure. **(c)** 15 minutes and longer synthesis time results in stacks of nanoflakes. **(d)** 30 minutes 4 cycles show that stacks of nanoflakes form a continuous film with the increasing thickness by the time. **(e)** Schematic of the growth mechanism of ZnO nanoflakes showing the growth from hexagonal structure to parallelogram structure and further increase in thickness as new layers are formed **(f)** Evolution of length and thickness of the flakes by time showing that the lateral dimensions of the flakes increases rapidly to around 10 µm at around 15 minutes and then stabilizes. The thickness of the single flakes remains constant around 20 nm. **(g)** I-V for samples of growth time, 3 minutes, 5 minutes, 15 minutes shows that the conductivity of the flakes increases with the time of synthesis as the thickness increases and new layers are added with time **(h)** I-V for continuous film of ZnO nanoflakes with growth time 15 minutes and 3 cycles. Show a tenfold increase in conductivity in presence of UV light.

To study the effect of substrate on the growth, the process was repeated on several substrates including, SiO$_2$/Si, Cu, Al, Ni and Fe alloys, Polyethylene tetrapthalate (PET) and Graphene (Fig. 3.1.14(a-d)). Uniform growth is observed on all the substrates except on Al where vertical nanowall growth is more pronounced and on Cu where a combination of both walls and flakes grows. The reason for wall growth on Al is described earlier. For the others, nanostructure morphology is largely independent of substrate while the rate of growth and the density changes with the substrate used. Ni and Fe alloys and graphene result high growth rate and density while SiO$_2$ and PET result lower growth rate and density for the same growth conditions. Among all the substrates used Graphene is of special interest owing to its unique electrical and optical properties. Moreover, growing oxides over Graphene could provide additional functionality to Graphene in electronic and optoelectronic applications. The Graphene used is CVD grown and the growth process is discussed in supplementary data. We observed consistent growth of ZnO flakes on Graphene over Si substrate as presented in SEM pictures in Fig. 3.1.14 (a-d). The micro –Raman spectroscopy in Fig. 3.1.14(e) shows two dominant peaks at 1578 cm^{-1} and 2695 cm^{-1} corresponding to G and 2D bands respectively confirms the presence of single layer Graphene. Comparing the Fig. 10(a) and (c) which show the growth of nanoflakes on SiO$_2$ and Graphene on SiO$_2$ respectively, for a growth period of 3 minutes, we observe that the density of growth on Graphene is markedly high. This could be attributed to the similar hexagonal atomic configuration in the 'c' plane of both materials which acts as good template for the growth of hexagonal ZnO structures. Also the high conductivity of the Graphene might have accelerated the growth of ZnO nanoflakes. Current- voltage characteristics measured to study the effect of Graphene are shown in Fig. 3.1.14 (f). I-V curves for Graphene 2D ZnO nanoflakes hybrid structure are presented. We observe that the conductivity of the resulting hybrid structure increases by 1000 times when compared to simple 2D ZnO nanoflake. In the presence of the UV light the conductivity increases when compared to the conductivity in dark. The rise in conductivity in the presence of UV light shows the photoconductivity in UV spectrum which is characteristic of ZnO. ZnO is also highly transparent in visible spectrum which makes it viable candidate as electrode in solar cell applications. The transmittance of the continuous ZnO flake layer grown on Graphene-over-Si substrate is presented in Fig. 3.1.14 (g) which shows transmittance exceeding 80% in the visible ($\lambda > 400$ nm) range and strong absorption in UV ($\lambda < 300$ nm) range.

In conclusion, we have successfully synthesized ZnO nanoflakes on different substrates at ambient conditions using sonochemistry. The process is a low temperature, scalable and potentially high throughput process which can control the morphology of ZnO nanoflakes with different synthesis parameters. Moreover, our sonochemical synthesis method is much faster than conventional hydrothermal methods, environmentally benign and CMOS compatible. Structural analysis revealed that the synthesized ZnO nanoflakes have hexagonal wurtzite structure oriented in <0001> direction and lateral growth direction perpendicular to (01$\bar{1}$0) plane. Electrical and optical measurements show that the as-synthesized nanostructures exhibit markedly higher electrical conductivity compared to ZnO nanowalls and nanorods. 2D ZnO nanostructures also exhibit high transparency close to 80% in visible and infrared region. Hence, single-crystalline ZnO nanoflakes can be used in many electronic and optoelectronic applications including transparent electrodes in photovoltaic cells, photodetectors, biosensors and flexible transistors.
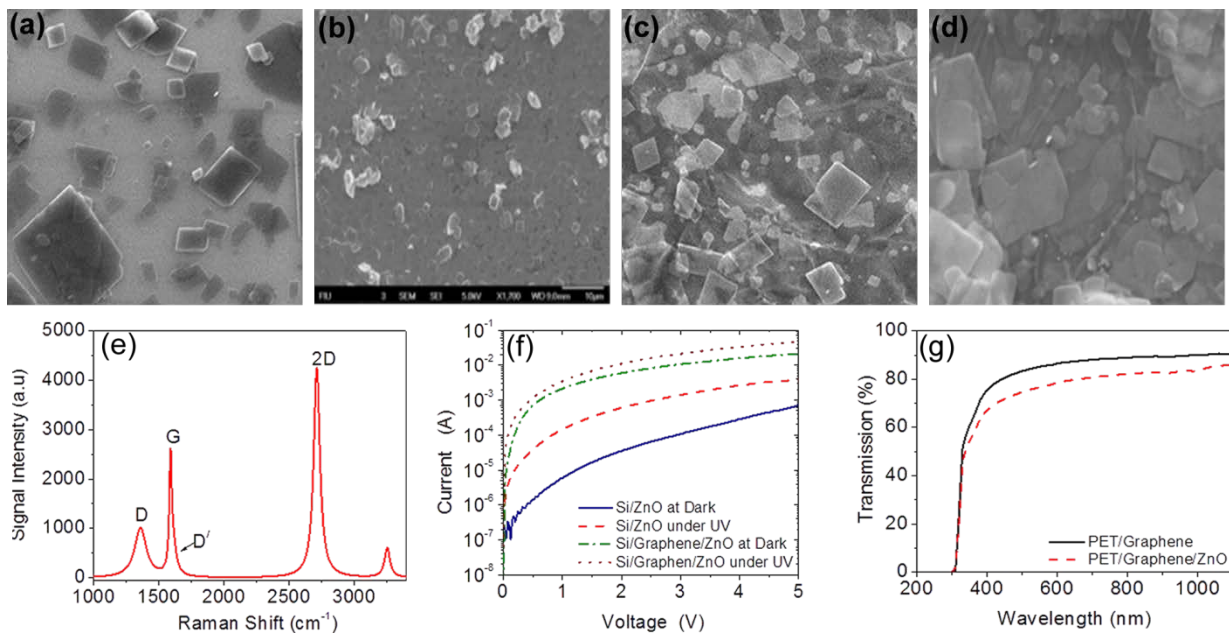
Figure 3.1.14: ZnO nanoflakes on **(a)** SiO$_2$ substrate, **(b)** Graphene/ Si **(c)** Graphene over SiO$_2$ **(d)** Graphene over PET. **(e)** Raman spectrum of the graphene on Si substrates confirms the presence of single layer graphene. **(f)** Electrical conductivity comparison in the presence of Graphene and without Graphene show that the conductivity increases for the hybrid structure ZnO-Graphene by more than 10 times when compared to just ZnO **(g)** Comparison of Transmission for Graphene and ZnO-Graphene hybrid structure.

3.2 Unusually High Optical Transparency in Hexagonal Nanopatterned Graphene with Enhanced Conductivity by Chemical Doping

The transparent conductor, indium tin oxide (ITO), is widely utilized in displays, touch-panels, light emitting diodes, and solar cells. Although the ITO exhibits desirably high optical transparency (T) and low sheet resistance (R_s), the limited supply of indium with increasing price has raised concerns on long-term supply of ITO material. Therefore, it is desirable to find potential replacement materials based on less critical elements. In addition, the trend is such that future displays are likely to become larger and many of them will probably be based on a flexible plastic substrate material. Thus, prospective displays would require more flexible transparent electrodes that can be produced at low temperature and over large areas at low cost. There are several novel materials for alternative transparent conductive electrodes, for example, carbon nanotubes (CNTs), metallic nanowires, thin metal films, and graphene. Compared with commercial ITO layer, these new candidates make some compromises between optical transparency and electric conductivity.

Graphene has recently emerged as a new material due to its remarkable properties including high charge mobility, high optical transmittance, mechanical strength, and flexibility. These attractive properties can make graphene a promising candidate for a transparent flexible electrode with low sheet resistance and high transparency, which can also be synthesized on a large scale. Potential applications of graphene as electrodes in a wide range of devices including field-effect transistors, touch sensitive screens, liquid crystal displays, light-emitting diodes, flexible field emission display, dye sensitized solar cells, and organic solar cells have been reported. However, to ensure

17

viable applications, the optical versus electrical characteristics of graphene films need to be further improved and tuned by engineering of two critical parameters, i.e., sheet resistance and optical transparency.
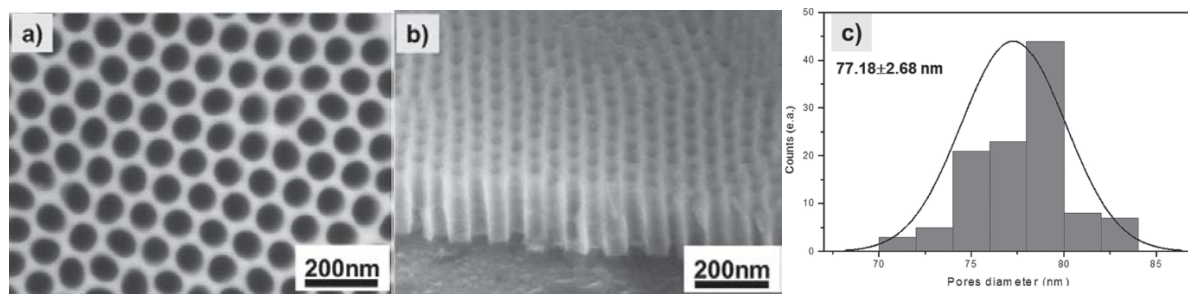

Figure 3.2.1: Scanning electron microscopy (SEM) images. a) AAO template (top view), b) tilted view AAO membrane with <300 nm thickness. c) Histogram of the AAO pore size with average pore size of 77.2 nm (standard deviation ±2.7 nm).

Graphene films having high conductivity and low optical loss may be engineered by doping or surface modifications. As the graphene quality is strongly dependent on the growth conditions, low sheet resistance has not been reproducibly obtained partly because of the poor crystallinity, formation of wrinkles, and small domain sizes of graphene layers. Chemical doping or functionalization has been shown to modulate the conductivity of graphene by controlling the charge carrier density, band gap, or work function. An alternative approach for reducing the sheet resistance is to stack or synthesize a few layers of graphene (FLG). Choi *et al.*[26] and Blake *et al.*[27] prepared higher-temperature- and longer-time grown, thicker graphene films, which, as expected, exhibited reduced sheet resistance but also reduced optical transmittance as the number of graphene layers is increased. Gunes *et al.*[28] proposed a new method of layer-by-layer (LbL) doping to decrease the sheet resistance of graphene films. With this method, sheet resistance was significantly decreased by up to ≈80% with some sacrifice in optical transmittance.
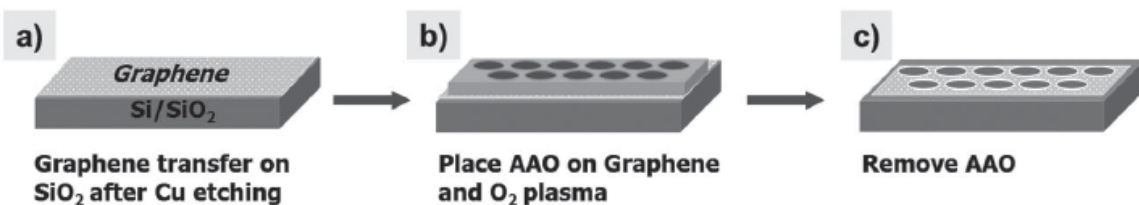

Figure 3.2.2: Schematic of nanopatterned graphene fabrication. a) CVD grown graphene was transferred onto a Si/SiO 2 substrate, b) an AAO template was placed on top of graphene, c) graphene in the exposed area was etched away by O 2 plasma through the AAO pores in the template and then the AAO was removed. Finally, porous graphene on SiO 2 was obtained.

[26] D. Choi , *et al. Mater. Res. Lett.* **2014** , *1* , 1 .
[27] P. Blake *et al*. *Nano Lett.* **2008** , *8* , 1704 .
[28] F. Gunes , *et al. ACS Nano* **2010** , *4* , 4595 .

To solve the drawback of low optical transmittance in FLG, we have introduced a nanohole array in the graphene layer so as to increase the area fraction of graphene-free regions. In order to increase the graphene-free area, ordered nanohole array has been achieved by UV/e-beam lithography and nanoimprint lithography. Although optical, electron, or related lithographic methods can provide precisely located nanoarrays, the overall size of the area that can be patterned into nanodimensions (e.g., below ≈100 nm feature size) in an industrially viable way is often limited due to the delicate handling, expensive, and time-consuming nature of such processes.

To advance a facile process technique for nanopatterned graphene (NPG), we have specifically utilized an anodic aluminum oxide (AAO) mask lithography as it can be scaled to large-area substrates with high-fidelity of patterning, which can be compatible with conventional lithographic processes. With an array of nanoholes introduced, the sheet resistance obviously becomes deteriorated (increased) due to the lost material pathway. However, a substantial portion of the lost electrical conductivity in the nanopatterned graphene formed by facile AAO technique could be recovered by doping, as is demonstrated in this work. Liu *et al.*[29] proposed that nanopatterned graphene can provide large number exposed edges of holes for effective doping sites indicating a possibility of tuning electrical transport properties of graphene.

In this report, we have demonstrated a new approach of controlling a transmittance and conductivity in a sheet of FLG. We have carried out experimental investigations on the optical and electrical performances in FLG before versus after chemical doping. In this work, nitric acid (HNO_3) was used as a molecular adsorbate to reduce the sheet resistance of graphene films. A facile patterning of the graphene has been accomplished by using a self-assembled, free-standing AAO template which is directly transferred onto FLG. To the best of our knowledge, this is the first time that such convenient AAO nanopatterning of graphene has been demonstrated without resorting to a buffer layer like polymer. The fabrication of NPG using the AAO approach can be employed as a novel method for engineering transmittance and conductance of graphene, which can open up other electronics and optoelectronics applications.

The AAO membrane prepared by two step anodization of high-purity aluminum foil exhibited locally periodic array of pores with the pore size being ca. 77.2±2.7 nm (Figure 3.2.1 a). As shown in the tilted image of an AAO membrane in Figure 3.2.1 b, the membrane thickness is ca. 200–300 nm. This self-assembly fabricated AAO membrane was used as a mask during the oxygen plasma etching of graphene for nanohole array formation.

Figure 3.2.2 schematically illustrates the present approach for fabricating NPG. For initial demonstrations, the CVD grown graphene layer on Cu foil was used as the starting material. The copper layer underneath was removed by electrochemical reaction with aqueous 0.1 m ammonium persulfate solution, $(NH_4)_2S_2O_8$. The floating graphene was transferred onto a Si/SiO$_2$ or quartz substrate. We used the Si/SiO$_2$ substrate for electrical measurements of sheet resistance and the quartz substrate to measure the optical transmittance. Silicon and quartz substrates were cleaned by piranha solution to remove any organic contamination and the surface was treated with oxygen plasma to introduce hydrophilic surface. The AAO membrane was placed on graphene and the transferred AAO membrane was used as an etching mask for fabrication of NPG.

[29] J. W. Liu , *et al.*, *Appl. Phys. Lett.* **2011** , *99* ,023111 .
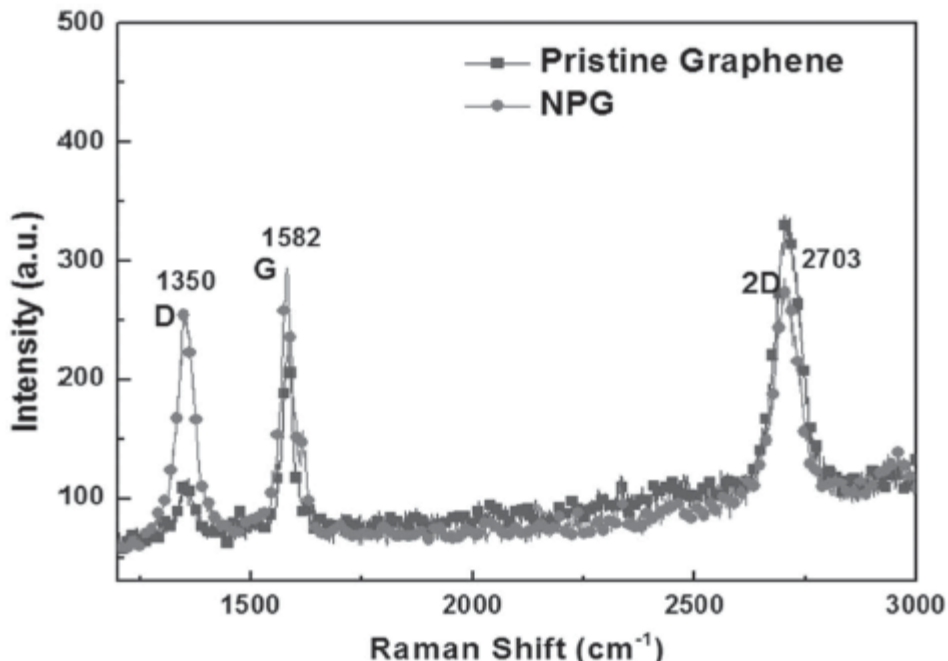
Figure 3.2.3: Comparison of Raman spectra of pristine and nanopatterned graphene (NPG) with their characteristic D, G, and 2D bands shown at the respective positions.

Zeng *et al.*[30] reported that nanometer-sized features on graphene cannot be achieved simply by directly placing the AAO membrane on rGO because of the rigid nature of AAO. Thus, PMMA was employed in their experiment as an adhesion layer between the AAO and graphene. To minimize the void space between graphene and AAO interface, they also annealed graphene/PMMA/AAO in a high temperature vacuum oven. However, we were able to overcome the issue by fabricating a less rigid and thin AAO template (<300 nm-thick), and successfully demonstrated fabrication of nanoholes patterned graphene using this oxide template without polymer buffer layer thus avoiding such complicated processes. The key to this success was the thinness and uniformity of the AAO membrane that we fabricated. After the oxide template was placed on top of graphene, O 2 plasma etching (25 W, 150 mTorr) was employed to generate nanoholes in the graphene layer. Finally, the AAO template was removed using a NaOH solution.

Raman spectroscopy was used as a nondestructive tool for probing the edge structure and the crystallinity of the sp 2 -bonded graphene samples. Figure 3.2.3 demonstrates the comparative Raman spectra of pristine graphene and NPG. The Raman data were taken from different spots on the graphene samples and were found to be uniform. Prior to patterning, the G ($\approx$1580 cm^{-1}) and 2D ($\approx$2680–2700 cm^{-1}) bands were prominent. Raman spectroscopy can also be utilized to determine the number of layers in multilayer graphene and to discriminate between single layer graphene (SLG) versus FLG using the intensity ratios of G band and 2D band. For a single layer graphene, I_G / I_{2D} intensity ratio is known to be $\approx$0.24 which increases with the number of graphene layers thus making it possible to estimate the thickness of graphene layers. Figure 3.2.3 shows that the ratio of I_G / I_{2D} in our graphene is around 0.7 and it can be estimated to be approximately 4–8

[30] Z. Y. Zeng , *et al. Adv. Mater.* **2012** , *24* , 4138 .

layers of graphene. The peak related to the 2D band also provides additional support for relative graphene layer thickness. The 2D peak in our NPG is located at $\approx$2703 cm^{-1}, which corresponds to $\approx$4–8 layers of graphene, which is consistent with the literature; for example, Rafiee et al.[31] have reported that, as the number of layers in graphene films is increased, the 2D peak shifts toward an upper frequency range from $\approx$2 680 cm^{-1} for monolayer graphene to $\approx$2 715 cm^{-1} for the □10 layers graphene. In addition to the difference in the intensity of 2D peak, the full width half maxima (FWHM) of 2D band also increases as the number of graphene layers increases. As the 2D band peak originates from a two phonon double resonance process, it is closely related to the band structure of graphene layers. Verma et al.[32] have successfully used the splitting of the electronic band structure of multilayer graphene to explain the broadening of the 2D band.

Table 3.2.1: Numerical values of optical transmittance T and sheet resistance Rs at 550 nm wavelength for the pristine versus doped NP graphene (see Figures 3.2.5 and 3.2.7), and estimated figure-of-merit values.

Plasma etch patterned	Before doping			After HNO$_3$ doping			I_D/I_G
	T [%]	R_s [ohm sq^{-1}]	$\sigma_{DC/OP}$	T [%]	R_s [ohm sq^{-1}]	$\sigma_{DC/OP}$	
Pristine	84.9	1206	1.8	82.8	859	2.2	0.26
30 s (54% area open)	94.2	16 670	0.4	94.0	2200	2.7	0.35
40 s (54% area open)	98.6	18 020	0.9	97.8	1823	10.2	0.55
50 s (not measured)	98.1	21 030	0.6	97.3	4739	3.1	0.77

For mono- and bilayer graphene, the FWHM of 2D band is $\approx$30 cm^{-1} and for the FLG in our data, it is $\approx$63.24 cm^{-1}. We believe that the 2D peak broadening can be attributed to the number of layer increases in graphene structure. In this work, the transferred graphene consists of about 4–8 layers of graphene sheets, as known in Raman, hence our samples can be referred to as FLG of few layers graphene. The D peak at $\approx$1330 cm^{-1} is related to defects and disorder. This peak is forbidden in perfect graphitic systems and requires a defect for its activation, and so it is observed by the presence of the edges in graphene samples. The integrated intensity ratio of the D band and G band (I_D / I_G) is a parameter sensitive to defect density.

Previous studies have revealed that the intensity of the D band is related to the basal plane disorder and thus, the increased D band (see Figure 3.2.3) in our NPG sheets may represent formation of disorders or defects caused by nanopatterning. We also note that there is an increase in intensity ratio of the I_D / I_G with more plasma etching time for nanopatterning. The intensity ratio of 0.35, 0.55, and 0.77 has been obtained (shown in Table 3.2.1) with increasing etching time from 30 to 40 s then to 50 s, respectively. This trend agrees with the previous report that for lithographically patterned graphene nanoribbons (GNR), I_D / I_G increases with an increase in defect density and decrease in neck width. After nanopatterning of our samples, there was a systematic upshift in the position of G band. The G band position for porous graphene was observed at $\approx$1582 cm^{-1}, which can be compared with the G position of pristine graphene ($\approx$1580 cm^{-1}) in our sample. This upshift in the G band position further confirms the hole doping in the NPG by the formation of oxygen dangling bonds with graphene, as reported by previous research.

[31] J. Rafiee ,et al. Nat. Mater. **2012** , *11* , 217 .
[32] V. P. Verma , et al. Appl. Phys. Lett. **2010** , *96* ,203108 .
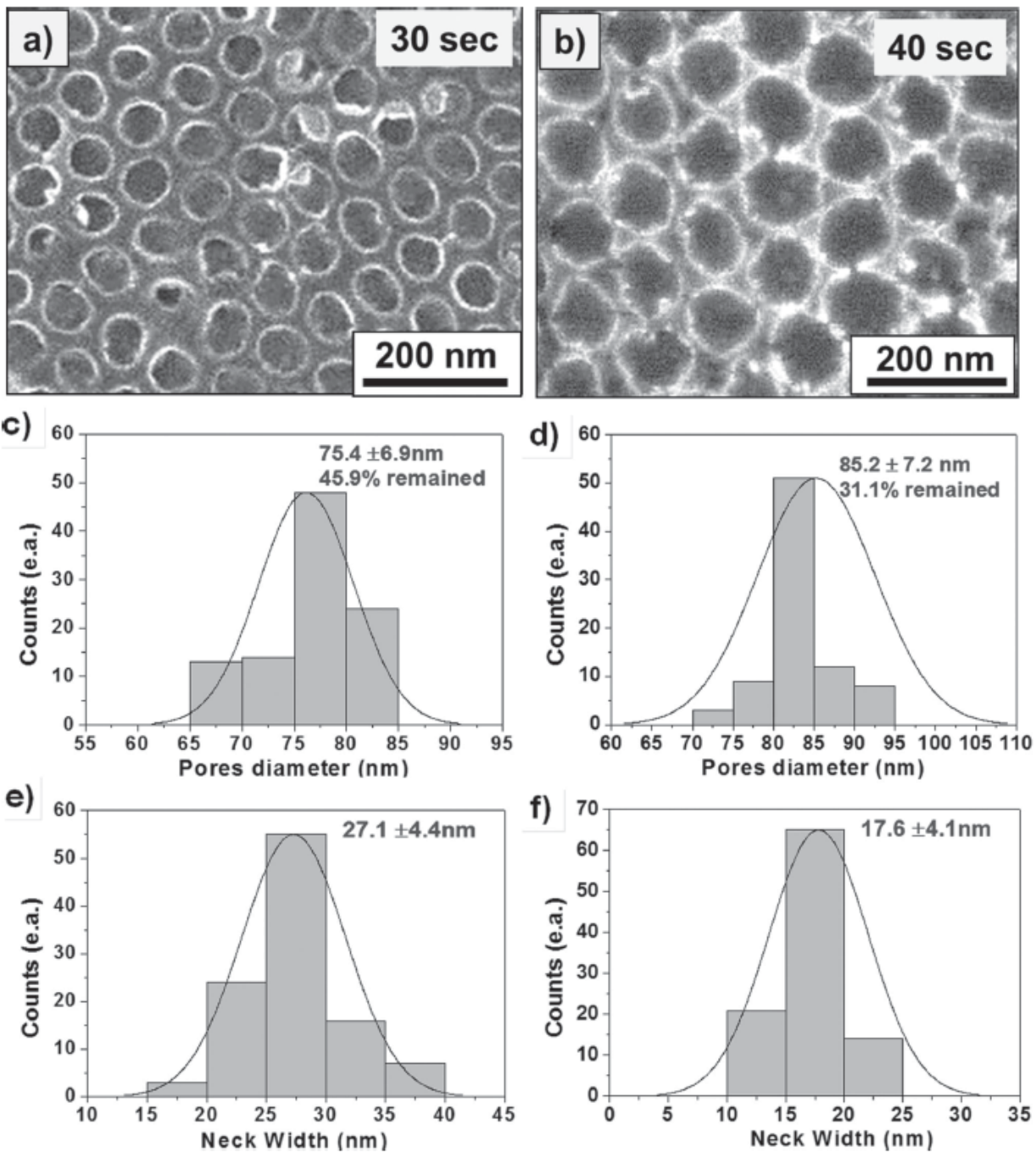
Figure 3.2.4: a,b) SEM images of the NPG surface after removing the AAO mask by 30 and 40 s etching, respectively. The histogram in c) shows that the average pore diameter in a) is 75.4 ±6.9 nm with ca. 46% graphene area remained, while d) shows that the average pore diameter in b) is 85.2 ±7.2 nm with ca. 31% graphene area remained (the average hole periodicity is 106.1 ±1.8 nm in both cases). The histogram in e) shows the neck width in the a) sample of 27.1 ±4.4 nm, and f) shows the neck width in the b) sample of 17.6 ±4.1 nm.

Figure 3.2.4 shows SEM images of the NPG obtained using our AAO templates with a periodicity of 106.11.8 nm. The histograms resulting from the statistical analysis show that a series of NPG samples with adjustable pores diameter have been achieved. The average diameter of pores (D_p) on graphene after controlled etching for 30 s is 75.4 ±6.9 nm. Figure 3.2.4 d shows a NPG with a larger average D_p of 85.2 ±7.2 nm, achieved through an intentional slight over-etching of 40 s. Here, it is demonstrated that the remaining area of networked graphene can be trimmed to 45.9% and 31.1% by adjusting the processing time to 30 and 40 s, respectively, under identical plasma etching condition (O$_2$ fl ow 50 sccm, pressure 150 mTorr, power 25 W). It is therefore possible to tune the coverage of graphene (remaining area of graphene) through etching time and other process parameters during the fabrication process. A control of plasma power can allow a slower plasma etching rate and an improved control of the degree of etching. It is envisioned that a pore widening process such as the controlled oxygen plasma etch could also be utilized to substantially reduce the graphene area and provide an additional control of the sheet resistance and optical properties. These SEM analyses on our graphene layer together with previous studies on graphene oxide samples clearly demonstrate that highly uniform, porous graphene can be obtained with controllable pore size and coverage by the template approach. A histogram was constructed for our samples (see Figure 3.2.4) with all the measured values from the .5 - 0.5 μm area SEM image. The average mode values of nanoconstriction width with corresponding standard deviations were calculated and reported based on the histogram generated in Figure 3.2.4 e,f.

The electrical properties of graphene are most likely affected by patterning of graphene, as was actually observed in this study for the NPG samples prepared by AAO template masking. The sheet resistance values, R_S , of the samples were measured in a four-probe configuration. Even though the sheet resistance can vary depending on the size of grains and amount of grain boundaries in graphene, as well as on defects/ impurities generated during graphene synthesis or transfer, the measured R_S of 1208 Ωsq^{-1} for unpatterned graphene is generally consistent with those reported by Li *et al.*[33] and Verma *et al.* The R_S of NPG samples increases considerably compared to the unpatterned graphene sample as shown in Figure 3.2.5 which plots the change of R_S according to the etching time and doping of NPG. These data show that the creation of NPG does in fact considerably increase the resistance of graphene by a factor of ≈15, well above the level of the original unpatterned graphene samples. R_S increases by 1380%, 1492%, and 1741% as compared to that of the unpatterned graphene for the etching time of 30, 40, and 50 s, respectively, as shown by green upward arrows in Figure 3.2.5.

This ability to control pore size in NPG is very important for controlling electronic properties, because charge transport properties are highly dependent on the width of the critical current pathway. In the case of GNRs, both theoretical and experimental works have shown that the size of the conduction bandgap or sheet resistance is inversely proportional to the ribbon width. Therefore, a narrow pathway width and a denser mesh structure can enable lower current delivery. Our fabrication process shows great versatility in controlling both the neck width and the coverage of graphene which can be tuned through controlled plasma etching or over-etching during the fabrication process.

[33] X. Li *et al. Nano Lett.* **2009** , *9* , 4359 .
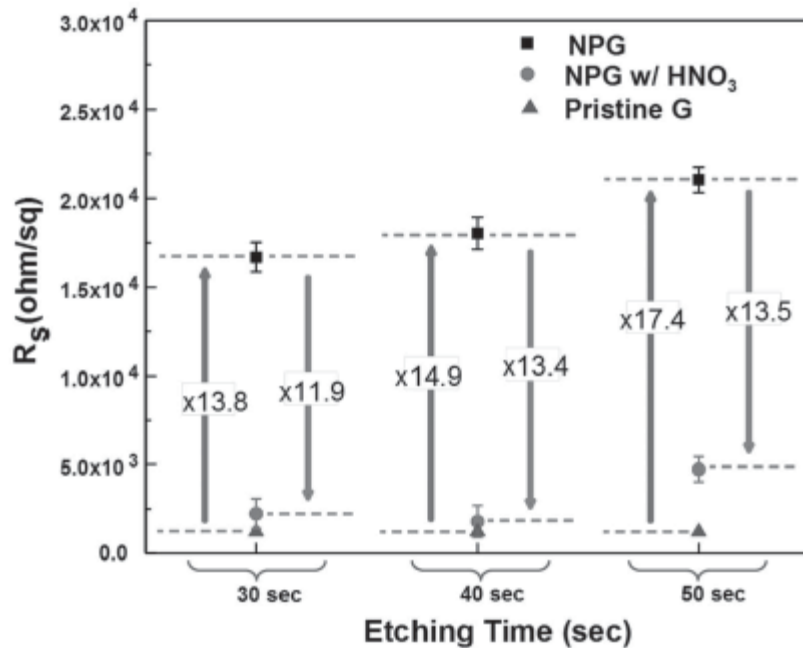
Figure 3.2.5: Sheet resistance (R_s) increase by nanopatterning of graphene (up arrows) and near-complete recovery of the electrical conductivity by chemical doping (down arrows), especially for the 40 s etched sample. The R_s values are plotted for three different etching times (30, 40, and 50 s).

The unique electronic property of graphene can be modulated by the charge carrier concentrations, which is dependent on introducing of gate bias and chemical doping, resulting in an improvement (reduction) of sheet resistance. Other novel approaches may also be introduced to further improve the optical transmittance and the sheet resistance of graphene, such as electrostatic doping method as was recently reported. With an introduction of electrostatic potential, various device junctions can be constructed by connecting GNRs of different width and orientation with perfect atomic interface, and more importantly device units can be selectively doped by manipulating the edge terminations of GNRs. In the present research, the electrical resistance of the graphene increases signifi cantly by a factor of ≈15 by removal of substantial graphene regions via nanopatterning into hexagonal array pores. However, our use of chemical doping on the nanopatterned graphene almost completely recovers the lost electrical conductivity, thus leading to a desirably much more optically transparent conductor having ≈7 fold reduced light blockage by the nanopatterned graphene material without much loss of electrical conductivity. It is likely that the availability of large number of edges created in the NPG provides ideal sites for chemical dopant attachment, leading to a significant reduction of the R_S . The results indicate that the NPG approach can be a promising route for simultaneously tuning the optical and electrical properties of graphene to make it more light-transmissible and suitable as a new generation of flexible transparent conductors.
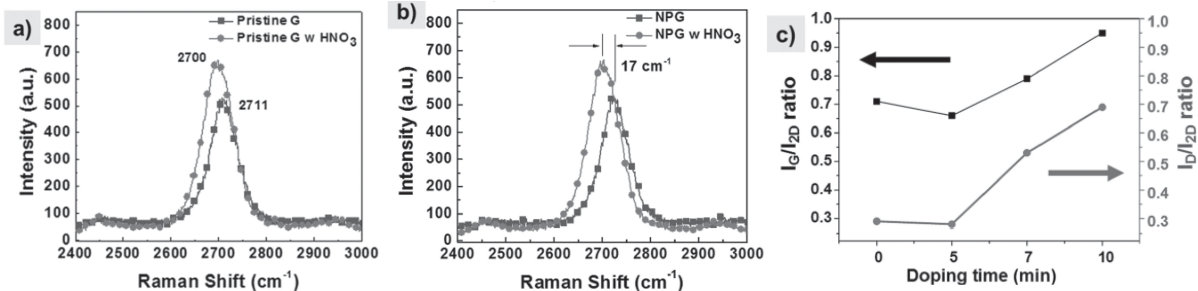
Figure 3.2.6: Comparison of Raman spectra before and after HNO$_3$ doping a) pristine graphene of ≈11 cm^{-1} blue shift. b) NP graphene showing ≈17 cm^{-1} blue shift on 2D band. c) Comparison of the intensity ratio for G and 2D bands by doping time.

The electrical sheet resistance of the graphene increases significantly by a factor of ≈15 by removal of substantial graphene regions via nanopatterning into hexagonal array pores as shown in Figure 3.2.5 (upward arrows). In order to reduce the sheet resistance increase by nanopatterning, we employed chemical doping of NPG with an exposure to nitric acid (HNO$_3$) for ≈6 min. HNO$_3$ is known to be one of molecular adsorbates that can be used to effectively p-dope graphene films. This can reduce the sheet resistance of graphene films and electrons are transferred from the graphene to the nitric acid as charge-transfer complex is formed according to the reaction. Bae *et al.*[34] investigated that the electrical properties of graphene films can be enhanced with various types of chemical dopants. The results indicate that the enhanced sheet carrier density is obtained in principle by multiplying the fi lm thickness to the bulk carrier density and by doping with nitric acid. The sheet resistance was reduced after a 63 wt% HNO$_3$ treatment for several minutes. However, the extent of resistance reduction upon chemical doping of pristine graphene sheet resistance was meager, only by 1.4 times as shown in Table 3.2.1 . The recovery in sheet resistance of unpatterned graphene is consistent with the previously reported 2–4 times increase of conductivity accompanying p-doping of graphene by nitric acid treatment. However, for the case of the nanopatterned graphene, an entirely different behavior is observed. The electrical conductivity recovery (sheet resistance recovery) by chemical doping is by a factor of ≈13 as shown in Figure 3.2.5 , much larger than the conductivity recovery for the case of nanopatterned graphene layer (by ≈1.4 in our graphene sample).

Such a pronounced electrical conductivity increase by chemical doping seen only in NPG samples is attributed to the availability of large number of edges created in the NPG structure which can provide ideal sites for chemical dopant attachment, thus leading to a significant reduction of the *R S* . In principle, the edges of nanopatterned holes provide active sites, where the carbon atoms are much more chemically reactive than that in the plane of the perfect graphene. Liu *et al.* reported that the graphene nanomesh structure serves as a source of chemical enhancement for Raman intensity of adsorbed molecules. The edges in the nanomesh can act as chemical sites to quickly trap molecules for chemical modification of graphene. If a similar doping mechanism applies to NPG, the large number of edges created on the nanohole arrays could facilitate attachment of HNO$_3$, which explains the very large enhancement in sheet conductivity observed in our doped NPG samples.

[34] S. Bae *et al. Nat. Nanotechnol.* **2010** , *5* , 574 .
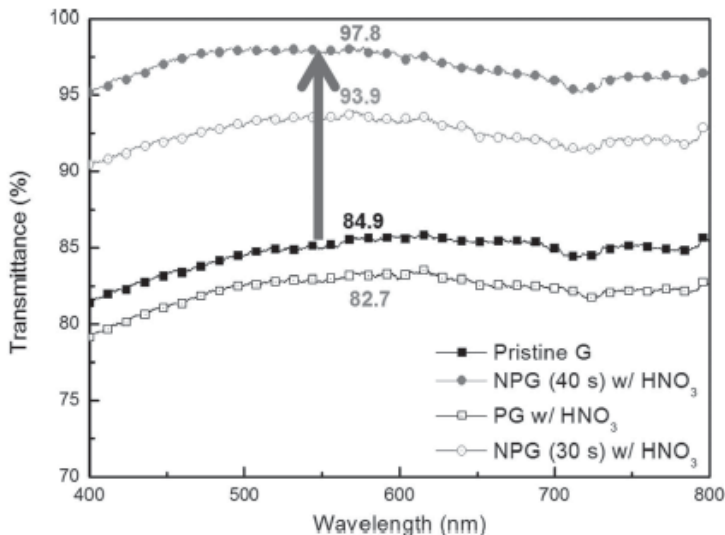
Figure 3.2.7: UV–vis spectra of pristine and NP graphene films on quartz substrates.

To understand the effect of acid treatment, we carried out a Raman spectroscopy analysis of the as-prepared NPG as well as nitric-acid-treated (doped) NPG. Figure 3.2.6 shows Raman spectra of the graphene fi lms before versus after doping with 63 wt% HNO_3 for 10 min. There is some blue shift ($\Delta v \approx 11$ cm^{-1}) in the 2D band peak for the pristine graphene, which is already known in p-doped graphene fi lm. The increased peak shift in the position of the 2D band with acid doping of NPG sample ($\Delta v \approx 17$ cm^{-1}) indicates that the HNO_3 carriers were doped in the NPG graphene lattice, which clearly indicates that the number of edge-plane-like active carbon sites in FLGs are increased compared with that in pristine graphene. The position of 2D band is very sensitive to the local doping level in graphene. Typically, a 2D band of undoped pristine graphene appears at 2700 cm^{-1}. After doping, there is a systematic upshift in the position of 2D band. The further enhanced upshift in the 2D band by acid treatment on NPG with increasing hole-doping is also confi rmed by the analysis of the sheet resistance as well as the 2D band shifts of patterned graphene via O_2 plasma etching, and also corresponds to the previously reported Raman spectra of HNO_3 -doped graphene showing a blueshift both for G and 2D peaks. The ratio of the intensities of Gand 2D-bands (I_G / I_{2D}) is also considered to be sensitive to doping. Figure 3.2.6 c shows the ratios of the G/2D intensity of graphene with various doping time. The intensity ratio shows a marked increase with the increase in doping time.

The optical transmittance spectra for FLG and NPG samples are shown in Figure 3.2.7 . Unlike the ITO fi lm, which provides a relatively good optical transmittance mostly for wavelength window from ≈450 to ≈600 nm, the FLG fi lm maintains good transmittance throughout the entire range of wavelengths of ≈400 to ≈800 nm studied in this investigation. The unpatterned graphene by itself was found to reduce transmittance at 550 nm by ≈15% in our graphene sample. These results are relatively consistent with previously reported transmittance on stacked CVD-grown graphene layers in which an attenuation coefficient of 2.6% per layer is extracted by fitting the data to Beer's law. As is demonstrated in Figure 3.2.7 , the transmittance of the NPG with 85.2 nm diameter pores has been found to be quite high, 97.8% at 550 nm, for 40 s etching time, which represents almost 7 times reduced light blockage than that for the pristine graphene counterpart. The transmittance of the NPG with 50 s etching time was similar with that for the 40 s sample

26

(Table 3.2.1). Interestingly, only a slight decrease in transmittance (from 94.2% to 94.0%) was observed by doping of the NPG by HNO_3 , while it induced a significant reduction in electrical resistance by an order of magnitude (from 16 670 to 2 200 Ωsq^{-1}) for the 40 s etched sample. In other words, the transmittance was less affected by doping than the electrical properties (Table 1). Geometrically, the nanohole array in the 40 s sample decreases the area of graphene by a factor of 0.689 (see Figure 3.2.4 d), which is based simply on the decrease in the coverage of NPG on the substrate compared to pristine graphene, while the increase in optical transmission is by a factor of 6.86x, obtained by comparing the light blockage of the pristine graphene (100% – 84.9% =15.1%) versus the 40 s plasma etched NPG hexagonal patterned graphene (100% – 97.8% =2.2%). Further detailed study is in progress to understand the mechanism behind this observation of surprisingly high optical transmittance in the doped NPG samples. Such a phenomenon points to a possibility of utilizing the properly nanopatterned and doped graphene as promising transparent conducting electrodes for display and other optoelectronic devices operating over a wide range of wavelengths. The starting graphene material utilized in this study was not the highest quality FLG graphene having lowest possible electrical sheet resistance, as compared to previously reported graphene samples, so the absolute value of the sheet resistance of our samples may not seem very low, however, the relative improvements obtained by nanopatterning and chemical doping, with the resultant optical transmission improvement, are quite impressive, which are likely to be similarly applicable to other graphene starting material having different electrical sheet resistance values.

For display type applications of transparent conductors, a proper combination of low electrical sheet resistance and high optical transmittance is essential. De *et al.*[35] have correlated the figure merit of transparent conductors to the ratio of the DC conductivity to optical conductivity, with high values of the ratio representing the desirable high transmission and low sheet resistance. The optical transmittance of graphene layer can be calculated by

$$T = \left(1 + \frac{Z_0}{2R_S}\frac{\sigma_{OP}}{\sigma_{DC}}\right)^{-2}$$

(3.2.1)

where Z_0 is impedance of free space and R_S is the sheet resistance. The ratio of DC conductivity over optical conductivity (σ_{DC}/σ_{OP}) was calculated for our pristine and nanopatterned graphene as shown in Table 3.2.1 . From the calculated ratio of σ_{DC}/σ_{OP}, the ratio of 1.8 was obtained for our pristine graphene (without patterning and doping). The figure-of-merit ratio (σ_{DC}/σ_{OP}) for the 40 s plasma etch NPG sample which was subsequently acid-doped is particularly high, increased to 10.2 as shown in Table 3.2.1 , which is comparable to the reported values. This value is 5.7 times higher than the (σ_{DC}/σ_{OP} =1.8) value for pristine graphene, which is also shown in Table 3.2.1. Because this σ_{DC}/σ_{OP} value has a higher correlation with the transmittance change than the sheet resistance, it is important to achieve a high transmittance for the transparent conductor applications. It is noted that the σ_{DC}/σ_{OP} ratio for our doped NPG samples is the highest for the 40 s optimally etched and doped nanostructure as compared to 30 and 50 s plasma etched and doped NPG. The 50 s plasma etch turned out to be an overetch as the hexagonal array nanohole pattern begins to get locally collapsed, which results in undesirable increase of electrical resistance in the NPG sample as shown in Table 3.2.1. Most of the previously reported data show a trend of

---

[35] S. De *et al. ACS Nano* **2010** , *4* , 2713 .

increased sheet resistance as the transmittance is increased, however our approach demonstrated that reducing the sheet resistance is possible while enhancing optical transmittance. The self-assembly type patterning of graphene using floating membrane of AAO is convenient, versatile, and should be of low ost. The dimensions of the AAO holes, spacing, and neck width are all controllable, from ≈20 nm regime to ≈300 nm regime. However, care should be taken in handling and deposition of the fragile AAO membrane in water, minimizing inadvertent membrane folding, wrinkling, or tearing when it is picked up by the relevant substrate material to be patterned. Those AAO areas that are not in good contact with the graphene layer underneath could allow inadvertent reactive ion etching (RIE) plasma to penetrate laterally and remove a part of the graphene material, although this will be a limited local phenomenon. For large-scale manufacturing, some automated or robotic-type handling of the membrane processing, rather than manual handling, would be more desirable.

Based on the trend seen in our results, we can calculate a possible figure-of-merit ratio to be as high as 130 if our starting material graphene were of high quality, which would be far over the industrially desired of figure-of-merit value (σ_{DC} /σ_{OP} =35). The minimum industry standard for ITO replacement materials is a sheet resistance of R_S < 100 Ωsq^{-1} coupled with transmittance of T >90% in the visible (σ_{DC} /σ_{OP} =35). For example, if a four-layer stacked high purity graphene (each having 240 Ωsq^{-1} sheet resistance is nanopatterned and doped similarly as our Figure 3.2.4 b,d sample, the final sheet resistance of the doped NPG sample is expected to be ≈150 Ωsq^{-1} sheet resistance and 98% transmittance. Desirable conductive transparent films in general require the sheet resistance to be 10–100 Ωsq^{-1}. It is worthwhile trying to use several layer graphene sheets to get the lower sheet resistance for transparent conductive films. However, there will be a compromise of optical transparency, so to the extent we can live with some loss of transparency in thicker graphene layer, the use of thicker layer can be considered, which will be explored in our follow-up research. Also, we will in the future try to utilize a better starting material of lower sheet resistance graphene (a few hundred ohms sq^{-1} as reported by other researchers), which should produce improved final end results. The present research clearly demonstrates a combined nanopattering and doping approach to drastically alter the optical and electrical conductivity properties simultaneously toward unusually high optical transmission characteristics, which, if adopted properly for the high-quality graphene, can be a promising route for a new generation of flexible transparent conductors.

In summary, successful fabrication of optically highly transparent (≈98%) graphene layer has been demonstrated by a proper combination of nanopatterning and chemical doping. This result has important implications for tuning electrical and optical properties of graphene simultaneously, as the two properties were previously controlled in an opposite way – e.g., increasing transmittance by scarifying resistivity. Our ability to control and manipulate the nanoholes in graphene sheets by AAO nanopatterning represents the first step toward graphene transmittance enhancement, and conductivity enhancement by means of defect creation and hydrogenation (or oxygenation). By converting the H-(or O-) termination to HNO_3 termination, the sheet resistance has been reduced to the level of pristine graphene, thus leading to a desirably much more optically transparent conductor having as much as ≈7 fold reduced light blockage by graphene material without much loss of electrical conductivity. It is likely that the availability of large number of edges created in the nanopatterned graphene provides ideal sites for chemical dopant attachment, leading to a significant reduction of the R_S while minimally affecting the transmittance. The results indicate

that the nanopatterned graphene approach can be a promising route for simultaneously tuning the optical and electrical properties of graphene to make it more light-transmissible and suitable as a new generation of flexible transparent conductors.

3.3 Graphene Band Gap Opening By Nanoparticle Decoration

Atomically thin Graphene has attracted attention of researchers as a promising novel material for electronic/optoelectronic applications due to its outstanding electrical, optical and thermal properties that include but not limited to its high carrier mobility, residual carrier concentration, saturation velocity, thermal conductivity and mechanical strength. Due to the degeneracy of Graphene valence and conduction band at the Dirac point, it shows a semimetalic characteristics—zero bandgap nature, which precludes its application in digital and logic circuits. In order to make Graphene a technology applicable to real systems and devices, a non-zero bandgap is indispensable. A bandgap can be introduced in Graphene either by breaking the translational symmetry or by breaking the sublattice symmetry. From density functional theory studies, it is evident that a bandgap in graphene can be achieved in several ways, which include but not limited to: adsorption of hydrogen molecule, doping with silicon and group IV element, adsorption of water molecule, and aromatic molecules. In experiment, it has been demonstrated that a bandgap starting from 2.5 meV up to 450 meV can be introduced in Graphene by decoration with Si-rich two dimensional islands, fabrication of Graphene nanomesh via nanoimprint lithography, formation of nanoperforated Graphene via block copolymer (BCP) lithography, adsorption of patterned hydrogen and adsorption of water molecules. However, these methods either result in a negligible bandgap value, or demand sophisticated/complex lithographic processes and controlled environment. In this work, we have demonstrated bandgap engineering of Graphene by decorating with randomly distributed ZnO nano-seeds as well as with randomly distributed gold nanoparticles, which break its sublattice symmetry, and opens up a bandgap.

The band structure of Graphene exhibits two bands intersecting at the k and k' points in the Brillouin zone—Dirac point. The energy-momentum relation of Graphene compared with that of conventional semiconductor is shown in Fig. 3.3.1.
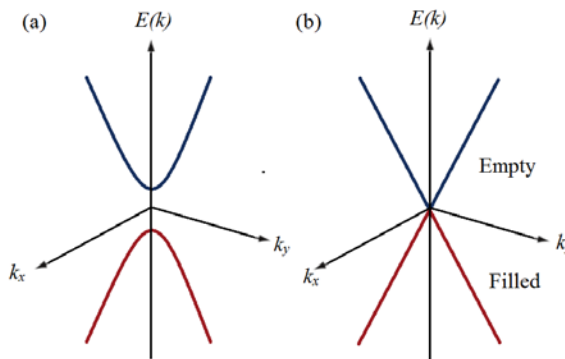

Figure 3.3.1: Energy-Momentum relation of (a) conventional semiconductor (b) Graphene

At this point, valence and conduction bands are degenerate, which results in Graphene to be a zero bandgap material. To introduce bandgap in Graphene, this degeneracy of valence and conduction bands at the Dirac point needs to be lifted off and it can be done by breaking the equivalence between the Graphene sublattices—the sublattice symmetry. In the Graphene decorated with randomly distributed nanoparticles, the interaction between nano-seeds/particles and Graphene

breaks the sublattice symmetry resulting in opening a bandgap. The bandgap of a semiconductor as well as engineered Graphene can be extracted from the slope of Arrhenius plot.

The rate constant of a chemical reaction (k) depends on absolute temperature (T), pre-exponential factor (A), universal gas constant (R), and activation energy (E_a) by the following exponential equation, well known as Arrhenius equation, as follows:

$$k = Ae^{\frac{-E_a}{RT}} \tag{3.3.1}$$

In a similar fashion, the conductivity of a semiconductor, σ is dependent on its absolute temperature (T) and activation energy for conduction (bandgap, E_g) by the following equation:

$$\sigma = \sigma_0 e^{-E_g/2kT} \tag{3.3.2}$$

Where the factor of 2 in the exponent is because, the excitation of an electron across bandgap produces two mobile carriers: an intrinsic electron and an intrinsic hole. The last equation can be written in the form of a linear equation:

$$\ln \sigma = \ln \sigma_0 - \frac{E_g}{2k}\frac{1}{T}, \tag{3.3.3}$$

which allows extraction of the bandgap if temperature dependent conductivity is plotted.

For the ZnO nanoseeds decorated Graphene, the nanoseeds were grown on top of single layer Graphene using zinc acetate dihydrate ($Zn(CH_3COO)_2 \cdot 2H_2O$) (ZAD) as reported in [36]. We modified this approach and utilize the effects of sonication to produce solution phase seeding in a solution exposed to the ambient. A 0.005M concentration of ZAD in isopropyl alcohol (IPA) solution was prepared at room temperature by stirring with a magnetic stir bar at 350 rpm for 5 minutes. Single layer CVD Graphene grown on Copper sheet was coated with PMMA using a regular spin coater and was put floating on ferric chloride ($FeCl_3$) solution for 8 hours without any disturbance while copper surface touching the solution. Once the copper was completely etched, it was washed with DI water multiple times without flipping, and eventually was transferred on SiO_2. After being transferred, the sample was put in a desiccant for 8 hours, and then was put in acetone at 50 ºC for 15 minutes to remove the PMMA. Polyethylene shadow Mask for Source/Drain patterning was written using a laser engraver. 10 nm Ti and 100 nm Au were e-beam evaporated to pattern the Source/Drain contacts at a chamber pressure of 2×10^{-7} mTorr. The contact length and width were 5 mm and 1 cm respectively and the distance between contacts were 5 mm. The samples were cleaned with methanol, acetone and isopropanol before immersing into the ZAD-IPA solution. The solution with the immersed substrate then was irradiated using a commercially available high intensity ultrasound setup (750W ultrasonic processor, Sonics and Systems). The sample was prepared with a single sonication cycles of 15 minutes duration and the amplitude of the 20 kHz ultrasonic probe was 75% of the maximum amplitude (~30 W.cm^{-2}). The global temperature of the aqueous solutions did not exceed ~70ºC.

---

[36] P.K. Vabbina *et al.* SPIE Proceedings (2011), doi: 10.1117/12.899418

The undecorated Graphene as well as Graphene decorated with ZnO nano-seeds were characterized by Raman spectroscopy. Fig. 3.3.2 shows the Raman spectrum of the pristine Graphene and Graphene decorated with ZnO nano-seeds, taken using a 532 nm laser with a spot size of 1 μm^2. The 2D/G ratio (0.93) of the pristine Graphene (bottom panel of Fig. 3.3.2) confirms the presence of single layer graphene. In addition, a peak at 432.39 cm^{-1} of the decorated Graphene (top panel of Fig. 3.3.2) confirms the presence ZnO. From the Raman spectra of decorated Graphene, a shift of G and 2D peaks is visible, with respect to those of the undecorated one.
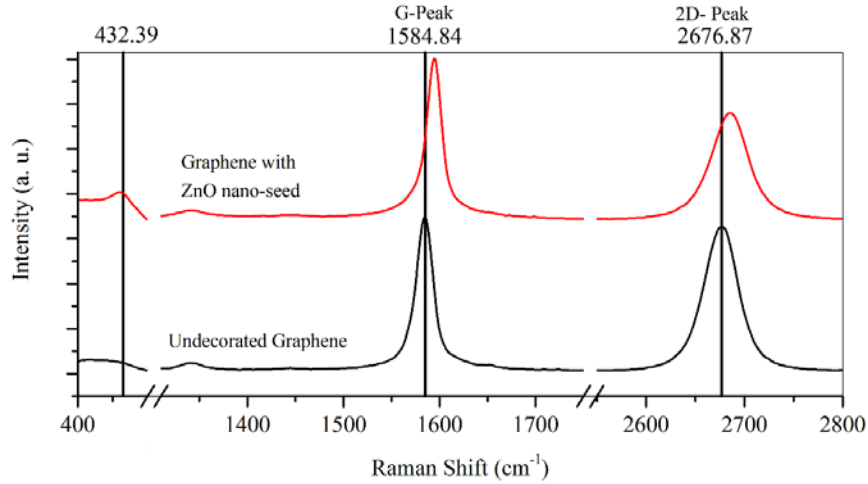

Figure 3.3.2: Raman spectra of pristine and ZnO nano-seed decorated single layer Graphene

The SEM image of the ZnO nano-seed decorated Graphene shown in Fig. 3.3.3. confirms the average size of the nano-seeds to be ~ 10 nm with the average separation distance of 10 nm. The AFM image of the decorated Graphene shown in Fig. 3.3.4 confirms the root mean square (RMS) and average roughness to be 15.85 nm and 12.34 nm, respectively. This large roughness is due to the presence of ZnO nano-seeds, as well as, due to the surface roughness of Graphene itself.
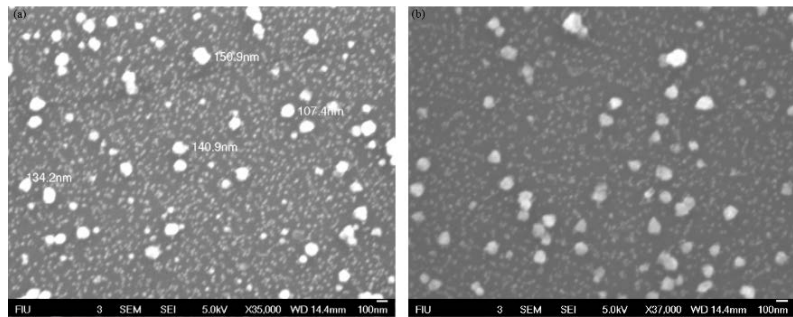

Figure 3.3.3: SEM image of ZnO nano-seed decorated single layer Graphene at two different magnifications
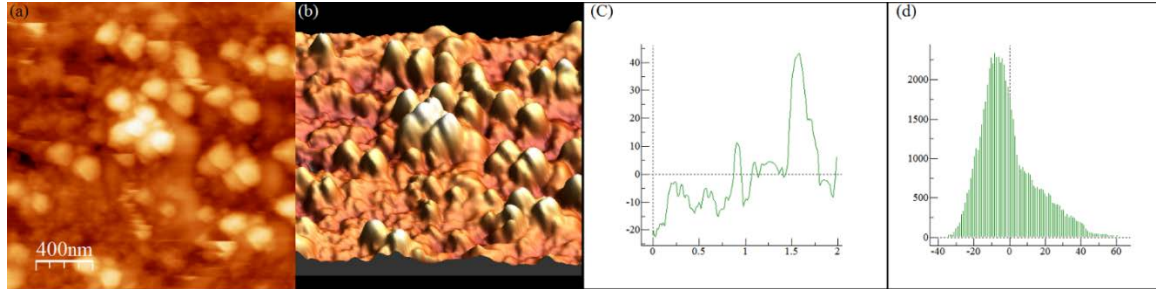
Figure 3.3.4: AFM image of ZnO nano-seed decorated single layer Graphene. (a) 2D image. (b) 3D image. (c) The profile along a straight line. (d) Roughness analysis: RMS Roughness= 15.85 nm and Average Roughness= 12.34 nm.

For gold nanoparticles decorated Graphene, the nanoparticles were grown first on SiO_2/Si substrate and then CVD Graphene was transferred on top of the gold nanoparticles, unlike the ZnO nano-seed decorated Graphene sample where nano-seeds were grown on top of Graphene. Gold nanoparticles were grown underneath Graphene because single layer Graphene was unable to sustain the high energy sputtering mechanism to form gold thin film if performed over Graphene after transfer. Three SiO_2/Si chips with 300 nm SiO_2, named as Sample-A, Sample-B, and Sample-C, were first solvent cleaned. Gold thin film was grown on SiO_2 by sputtering. The gold film thickness on Sample-A, Sample-B, and Sample-C were measured at the edge by using atomic force microscopy (AFM). Fig. 3.3.5 (a), (b), and (c) show the profile of the step of Sample-A, B, and C, with the 2D and 3D views inset. The film thickness estimated from the AFM image for Sample-A, B, and C were 1 nm, 4 nm, and 7 nm, respectively.
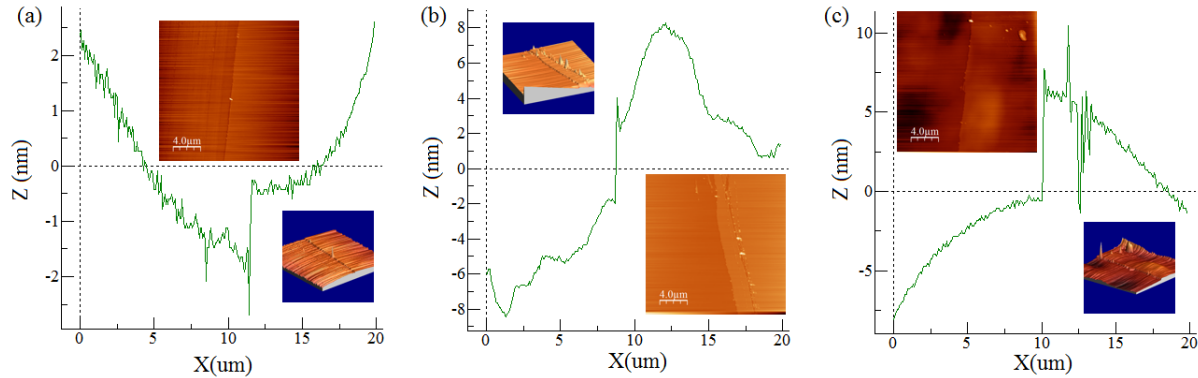

Figure 3.3.5: The profile of the step at the edge of sputtered gold thin film on (a) Sample-A, (b) Sample-B, and (c) Sample-C, measured by Atomic Force Microscopy (AFM) with 2D and 3D views (inset).

The samples were then annealed in N_2 environment at 800 °C for 30 minutes with a ramp of 5 °C/s. At this high temperature and ramp, the gold thin film dewetted and formed gold nanoparticles, as expected. The presence of nanoparticles was confirmed through SEM imaging, as shown in Fig. 6. From the AFM and SEM image shown in Fig.3.3.5 and Fig. 3.3.6, it is evident that: Sample-A with the thinnest gold film sputtered (1 nm) resulted in the least dense nanoparticles growth with largest diameter, Sample-B with 4 nm sputtered gold has denser nanoparticles with smaller diameter, compared to Sample-A, and Sample-C with the thickest gold film (7 nm) has intermediate nanoparticle density and diameter.

32
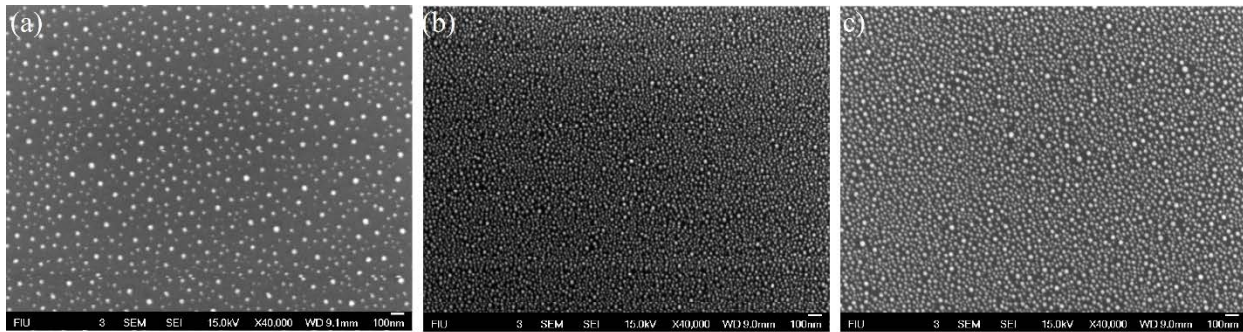
Figure 3.3.6:SEM image of gold nanoparticles grown on SiO_2 of (a) Sample-A, (b) Sample-B, and (c) Sample-C.

Using the standard graphene transfer method mentioned above, single layer graphene was transferred on top of the gold nanoparticles decorated substrate, and eventually, PMMA was removed with acetone. From Raman spectroscopy as shown in Fig. 3.3.7, it is evident that the 2D and G peaks of Graphene decorated with gold nanoparticles shifted compared to those of the undecorated one, as expected. As before, Polyethylene shadow masks were used to pattern contact pads with length, width, and in-between separation of 2 mm, 2mm, and 7 mm, respectively, consisting of 10 nm Ti and 300 nm Au.
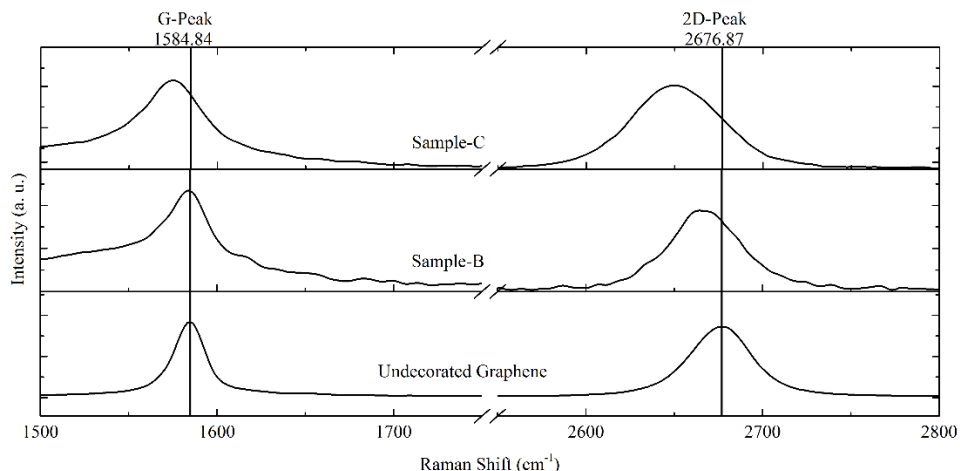

Figure 3.3.7: Raman spectrum of undecorated Graphene and decorated Graphene: Samples-B, C

Bandgap of nanoparticles decorated Graphene was estimated measuring temperature dependent conductivity using the Eq. (3.3.3). A commercially available vacuum probe station integrated with a precision thermal chuck and temperature control system, turbo pump and semiconductor parameter analyzer was used to measure the temperature dependent I-V characteristics. The pressure inside vacuum chamber was set at 25 mBar. At pressure less than 25 mBar, the sample temperature was found unable to follow the thermal chuck temperature due to loss of thermal conductor–air in-between. At first, the sample was left in a vacuum of 25 mBar for 5 hours and then the current-voltage characteristics of the sample was measured keeping the chamber pressure constant, at different temperatures starting from 0 $^\circ$C to 110 $^\circ$C with a step size of 5 $^\circ$C, and at each temperature point, the sample was left for 5 minutes before the measurement was taken.

33

For the Graphene sample decorated with ZnO nano-seeds, a DC voltage was ramped starting from -500 mv to +500 mv with a step size of 10 mV as shown in Fig. 3.3.8 (a), and both the hold time and delay time at each bias point were set at 20 ms. From the current-voltage characteristics of this sample, its resistivity and conductivity were extracted for each temperature value and the resistance was found to decrease linearly with temperature. Eventually, from the Arrhenius plot shown in Fig. 3.3.8 (b), slope was extracted and the bandgap was calculated to be 7.36 meV. We further investigated this bandgap opening process by decorating single layer Graphene with ZnO nano-seeds, whose lateral size (~300 nm) was much bigger compared to Graphene lattice constant (~ 2.46 Å), and it did not show semiconductor properties.
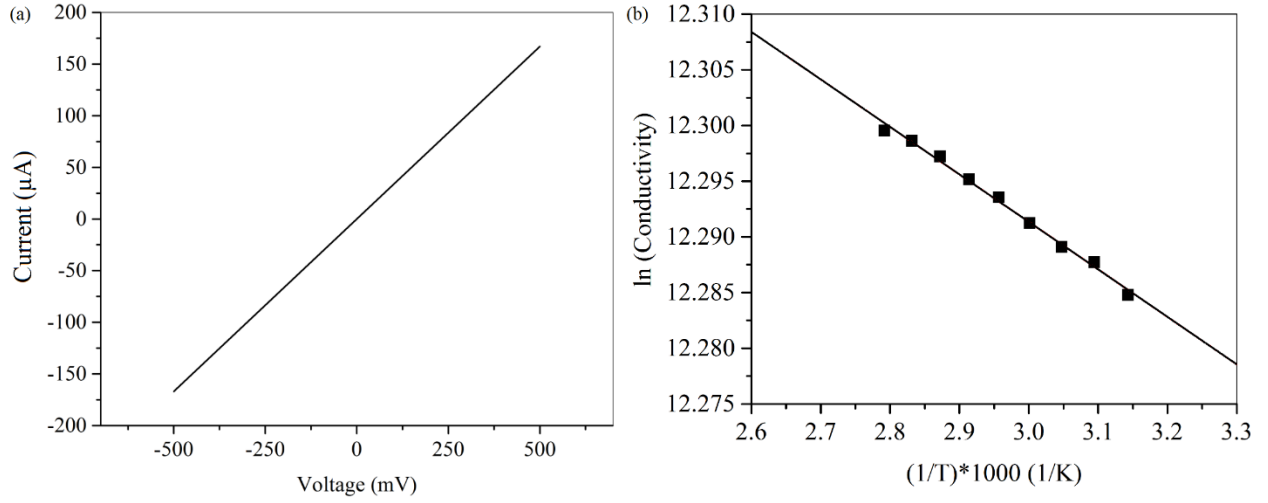

Figure 3.3.8: (a) The current-voltage characteristics of the ZnO nano-seed decorated Graphene at various temperatures, (b) The temperature dependent conductivity property.

For the Graphene samples decorated with gold nanoparticles, the same experimental setup and procedure was followed to measure the introduced bandgap. The logarithm of film conductivity versus inverse of temperature of Sample-B, and C are shown in Fig. 3.3.9, with the respective current-voltage characteristics and temperature-resistance characteristics at 50 °C, inset. The extracted bandgap from the slope of conductivity curve of Sample-A (not shown in Fig. 3.3.9), B, and C were 40.27 meV, 83.98 meV, and 59.91 meV, respectively, as expected from the density functional calculations reported in [37].

In conclusion, we have experimentally demonstrated the opening of a bandgap of single layer CVD Graphene by decorating it with randomly distributed nanoparticles. The first approach of decoration with randomly distributed ZnO nano-seeds opened an insignificant bandgap. On the other hand, the resulting bandgap due to decoration with gold nanoparticles was much more prominent compared to the ZnO nano-seed samples and showed a dependence on nanoparticle density and size. The proposed method of bandgap opening can be further investigated varying nanoparticle size, height, and density. Graphene with a moderate bandgap achieved by fine tuning of this decoration process can be used for digital and logic devices.

[37] S.S. Carara *et al.* Phys. Rev. B 80, 115435 (2009)
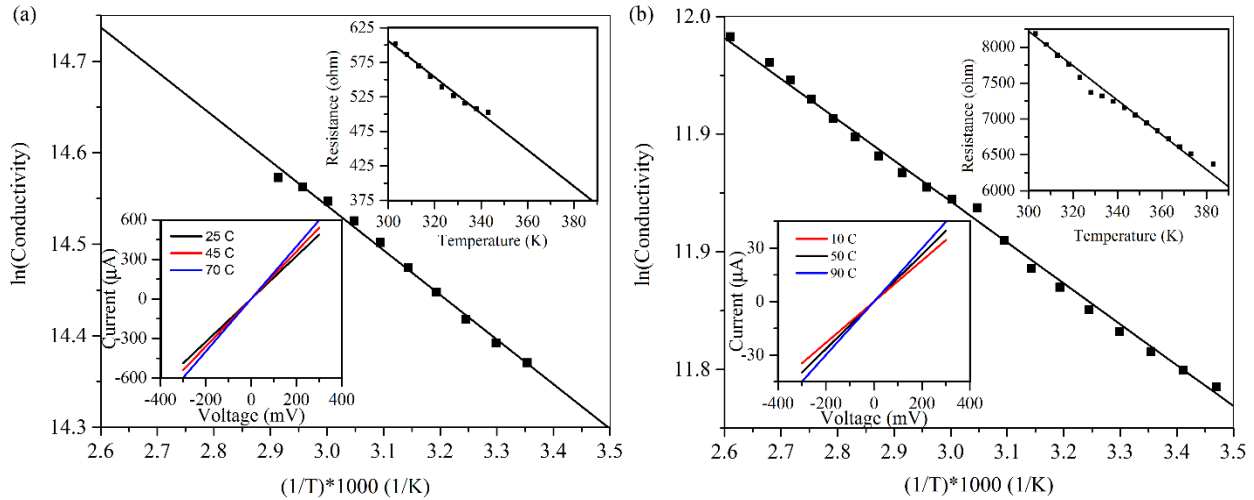
Figure 3.3.9: The temperature dependent conductivity curve of (a) Sample-B and (b) Sample-C, with corresponding current-voltage characteristics at different temperatures and temperature-resistance characteristics, inset.

3.4 Graphene FETs with Improved High Frequency Performance

The advantages of Graphene as a channel material of FETs include but not limited to its perfect 2D confinement of carriers, high residual carrier concentration, high carrier mobility, mechanical flexibility, and extremely high thermal conductivity. The access resistance of GFETs adversely affect the current gain cut-off frequency, f_T by reducing the transconductance and drain current and specially becomes very crucial in downscaled GFETs with shorter gate length. It is therefore desired to minimize GFET access resistance. In conventional silicon based RF transistors, the resistance of access regions is reduced by doping through ion implantation. However, In GFETs, the access regions consist of just a monolayer ungated Graphene with a high sheet resistance, compared to that of heavily doped Si MOSFETs. As a result, the access resistance of GFETs is comparable to the resistance of gated Graphene channel and the 2D structure of Graphene negates the use of ion implantation to dope. The typical value of access resistance of a Silicon MOSFET is at the order of ˜150 Ω-μm. On the other hand, the typical access resistance value of a Graphene FET is ˜350 Ω-μm and 80% of the total device resistance.[38] To utilize the complete advantage of Graphene as a channel material, the set of limitations on the high-frequency performance of GFETs arisen from the access resistances must be eliminated.

It is well known that the source/drain resistances comprising of contact resistance and access resistance impose important set of limitations on the high frequency performance of sub-micrometer FETs by reducing the external transconductance leading to a lower drain current and their minification ensures improved RF performance. These resistances delay the transition of carriers through the device and in terms of delay time, reduction of transit delay time caused by channel resistance and parasitic delay time caused by source/drain resistance ensure high cut-off frequency that can be achieved through shorter gate length and smaller access regions,

---

[38] S.K. Hong *et al.*"Resistance analysis and device design guideline for graphene RF transistors," 2D Materials, vol. 2, no. 3, pp. 034011 (2015).

respectively. Here are some attempts of transit time reduction to improve RF performance: 550 nm and 240 nm long top gated GFET with epitaxially formed Graphene on the Si face of a semi-insulating high purity SiC wafer and 10 nm HFO_2 as gate dielectric demonstrated cutoff frequency of 53 GHz and 100 GHz respectively.[39] GFET with epitaxial Graphene on Si-face of 4H-SiC having gate lengths between 2 μm to 0.5 μm demonstrated current gain cut-off frequency f_T of 4.1 GHz for 2.0 μm long gate GFET whereas the 0.5 μm long gate GFET showed an exceptional high power gain cut-off frequency of 16 GHz.[40] GFETs having CVD Graphene transferred from copper to diamond-like carbon (DLC) as substrate with 500nm, 140nm and 40nm long gates demonstrated cut-off frequencies of 26GHz, 70GHz and 155GHz respectively.[41]

Self-aligned process is used to reduce access region length that can effectively reduce parasitic delay time and increase f_T. Self-aligned fabrication of T-gate CVD Graphene FET with gate length of 110nm and 170nm with shorter ungated Graphene sections of about 20- 40nm were reported showing f_T of 15 GHz and 23 GHz respectively.[42] GFETs with self-aligned nanowire gate having gate length of 210 nm, 182 nm and 144 nm demonstrated f_T of 125 GHz, 168 GHz and 300 GHz respectively.[43] However self-aligned process makes fabrication more complex with smaller tolerances.

Reduction of access resistance for enhanced RF performance in III-N high electron mobility transistors (HEMT) and in Graphene FETs (GFET) have been reported.[44],[45] Here, rather than reducing the access resistance by minimizing ungated region length or doping, we proposed, extensively analyzed, fabricated/integrated, and characterized a novel device structure with controllable access resistance having a total of 5 contacts including source, drain, gate, and 2 field controlling electrodes (FCEs). The FCEs are capacitively coupled to the access regions of the device. The proposed device shows a higher cut-off frequency due to minimization of parasitic resistance. In addition to that, the capacitive coupling technique of the additional contacts ensures mitigation from additional power consumption.

An important metric for RF transistor's performance measurement is its current gain cutoff frequency, f_T. Current gain is the ratio of current at the output terminal to that in the input terminal. In common emitter configuration, the input terminal of a FET is the gate and the output terminal is drain.

---

[39] Y.M. Lin *et al.* Science, vol. 327, no. 5966, pp. 662, Feb 5 2010.

[40] K. Tahy *et al.* "Gigahertz operation of epitaxial Graphene transistors," in 2009 Device Research Conference, 2009

[41] Y. Wu *et al.* Nature, vol. 472, no. 7341, pp. 74-78 2011

[42] Y. Badmaev, *et al.* ACS nano, vol. 6, no. 4, pp. 3371-3376 2012.

[43] L. Liao, *et al.* Nature, vol. 467, no. 7313, pp. 305-308 2010

[44] Y. Lin, *et al.* Electron Device Letters, IEEE, vol. 32, no. 10, pp. 1343-1345 2011.

[45] H.C. Movva, *et al.* Appl.Phys.Lett., vol. 101, no. 18, pp. 183113 2012.
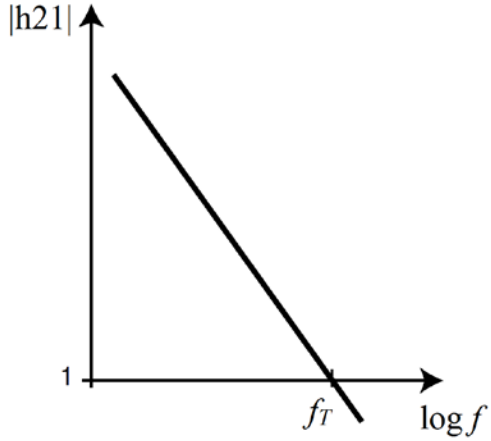
Figure 3.4.9: Relation between current gain, |h21| and frequency

As it is a FET, the input current in DC is zero. As a result, the current gain for DC is theoretically infinite, h21 = i_{out}/i_{in} = $i_{out}/0$ = infinite. The reactance of gate to channel capacitance is inversely dependent on frequency and with increasing frequency, the reactance decreases. As a result, the input AC current also increases with frequency which results in a decrement of current gain. The frequency at which, current gain drops to unity is called current gain cut-off frequency. A typical relation of current gain, |h21| and frequency is shown in Figure 3.4.9.

3.4.1 Analytical and Numerical Analysis of GFETs with Field Controlling Electrodes
Small Signal Circuit Analysis of Regular Graphene FET
The schematic of a conventional 3-terminal GFET on SiO₂ with the small-signal equivalent circuit laid on top is shown in Figure 3.4.10.
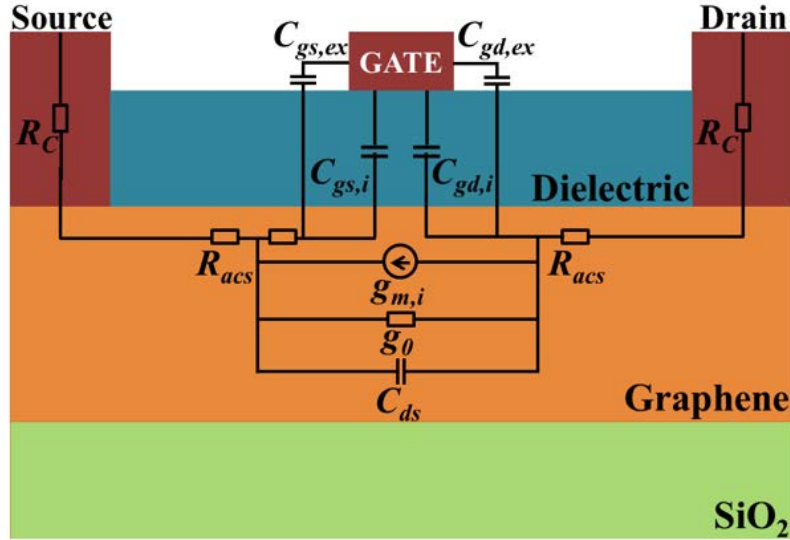

Figure 3.4.10: Schematic of a conventional 3-terminal GFET on SiO₂ with the small-signal equivalent circuit laid on top.

The gate to channel capacitance is actually a distributed capacitance and is usually simplified as

two capacitors: gate to source capacitance, C_{gs} and gate to drain capacitance, C_{gd}, such that

$$C_g = C_{gs} + C_{gd} \qquad (3.4.3)$$

The gate to source capacitance and gate to drain capacitance are composed of both internal and external parts which can be expressed as

$$
\begin{aligned}
C_{gd} &= C_{gd,i} + C_{gd,ex} \\
C_{gs} &= C_{gs,i} + C_{gs,ex}
\end{aligned}
\qquad (3.4.4)
$$

Where $C_{gd,i}$ and $C_{gd,ex}$ are the intrinsic and extrinsic part of gate to drain capacitance, whereas, $C_{gs,i}$ and $C_{gs,ex}$ are the intrinsic and extrinsic part of gate to source capacitance. The intrinsic capacitances, $C_{gd,i}$ and $C_{gs,i}$ are parallel plate capacitances which are dependent on gate length. On the other hand, the extrinsic capacitances $C_{gd,ex}$ and $C_{gs,ex}$ are in fact fringe capacitances and independent on gate length.

The small-signal gate-source and gate-drain capacitance can be calculated as:

$$C_{gs} = \frac{\delta Q_{CH}}{\delta V_{GS}} , \; V_{DS} \text{ is constant} \qquad (3.4.5)$$

$$C_{gd} = \frac{\delta Q_{CH}}{\delta V_{DS}} , \; V_{GS} \text{ is constant} \qquad (3.4.6)$$

Here, Q_{CH} is the total charge in Graphene channel, V_{GS} is gate to source voltage and V_{GD} is the gate to drain voltage. The total channel charge Q_{CH} can be expressed as:

$$Q_{CH} \approx \frac{WC_{OX}}{E_{AV}} V_{DS} \left(V_{eff} - \frac{V_{DS}}{2} \right) \qquad (3.4.7)$$

Here, W is the device width, C_{OX} is the gate oxide capacitance, E_{AV} is the average electric field, and V_{eff} is effective gate-source overdrive voltage. If we replace $E_{AV} \approx \frac{V_{DS}}{L}$ in the above equation, the simplified expression for Q_{CH} turns out to be:

$$Q_{CH} = C_{OX}WL(V_{eff} - \frac{V_{DS}}{2}) \qquad (3.4.8)$$

Now, the small signal gate to drain and gate to source capacitance can be calculated as:

$$C_{gs} = C_{ox}WL$$

$$C_{gd} = \frac{C_{ox}WL}{2}$$

(3.4.9)

If $g_{m,i}$ is the intrinsic transconductance, the extrinsic delay of the device τ_{ext} can be expressed as

$$\tau_{ext} = \frac{C_{gs,ex} + C_{gd,ex}}{g_{m,i}}$$

(3.4.10)

The intrinsic capacitances $C_{gd,i}$ and $C_{gs,i}$ are dependent on gate length and directly scale with that. The intrinsic delay time τ_{int} can be expressed as

$$\tau_{int} = \frac{C_{gs,i} + C_{gd,i}}{g_{m,i}}$$

(3.4.11)

The parasitic time delay due to parasitic resistances and capacitances can be expressed as

$$\tau_{par} = C_{gd}(R_S + R_D).[1 + (1 + C_{gs}/C_{gd})g_0/g_m]$$

(3.4.12)

where $g_0 = 1/R_{SD}$ is the output conductance and R_S and R_D are the source and drain resistance representing the ohmic contact resistance, R_C and source/drain access resistance, R_{acs} in series:

$$R_D = R_S = R_C + (L_{acs}/\mu q n_0 W)$$

(3.4.13)

here L_{acs} is the access region length (L_{gs} and L_{gd}), μ is the carrier mobility, q is electronic charge, n_0 is the residual carrier density in Graphene and W is the device width. The current gain cut-off frequency f_T is inversely proportional to the total delay time in the device and can be expressed as

$$1/2\pi f_T = \tau_{int} + \tau_{ext} + \tau_{par}$$

(3.4.14)

Thus through summing up all the delay times and rearranging, the f_T of the device can be related to the small signal circuit parameters as follows:

$$f_T = \frac{g_m/(2\pi)}{[C_{gs} + C_{gd}].[1 + (R_S + R_D)/R_{SD}] + C_{gd} \cdot g_m \cdot (R_S + R_D)}$$

(3.4.15)

where R_{SD} is the channel resistance that can be expressed as follows:

$$R_{SD} = L_G / \mu q (n_0^2 + n_g^2)^{1/2} W$$

(3.4.16)

where n_g is the carrier density due to gate modulation. One needs to minimize the delay times to increase the current gain cut-off frequency, f_T as well as maximum oscillation frequency, f_{MAX}, which is proportional to f_T. From Figure 3.4.11, it is visible that for short channel devices, the effect of parasitic time delay, τ_{par} becomes more prominent compared to that of long channel

devices. So, for short channel devices with good high frequency performance, its minimization becomes indispensable.
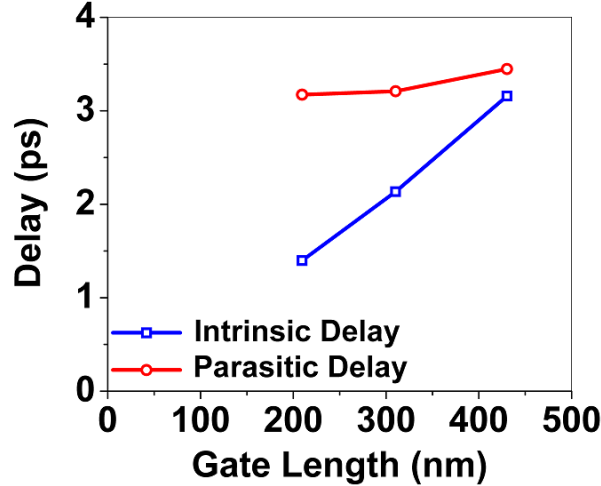

Figure 3.4.11: Intrinsic and parasitic time delays vs. gate length of In$_{0.7}$Ga$_{0.3}$As-channel HEMTs reproduced from [46].

Small Signal Circuit Analysis of Top FCE GFET

To reduce the GFET access resistance, here we propose a novel device structure consisting of two capacitively coupled FCEs, placed on top of the device, at the ungated access regions as shown in Figure 3.4.12 (b). As the transistor action of the device takes place at the gate terminal, the additional DC bias at the FCEs will help supporting the total device current in either of the transportation regimes (electron/hole) by selective population of particular type of carriers at the access regions.
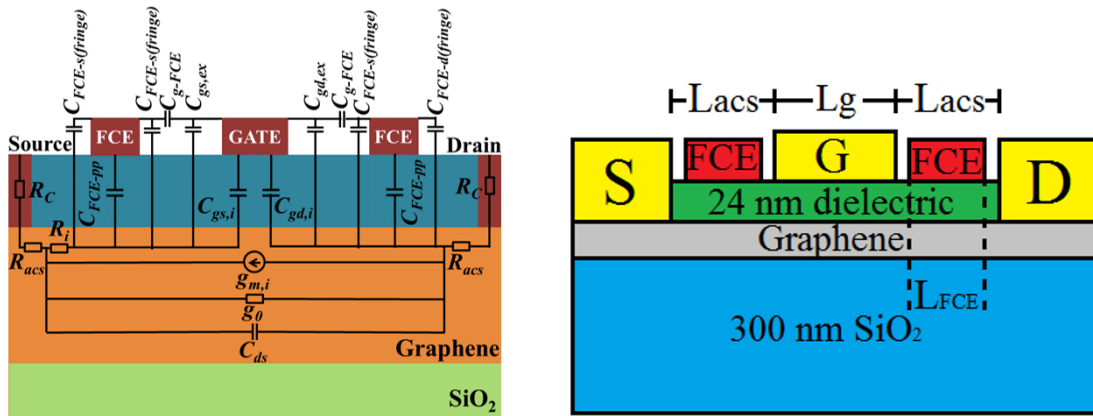

Figure 3.4.12: (a) Small signal equivalent circuit overlaid on top of top FCE GFET (b) Schematic of the proposed top FCE GFET (not in scale).

---

[46] S. Fukuda, *et al.* Japanese Journal of Applied Physics, vol. 48, no. 4S, pp. 04C086 2009

The proposed FCEs independently biased with a DC voltage reduce the source/drain access resistance, as well as, introduce some additional parasitic capacitance. A small signal equivalent circuit overlaid on top of the proposed GFET with two FCEs placed on top of the access regions is shown in Figure 3.4.12 (a). The FCEs make a parallel plate capacitance, $C_{FCE\text{-}pp}$ and two fringe capacitances, $C_{FCE(fringe)}$ with the Graphene channel. As all three of the capacitances are parallel to each other, the total FCE capacitance, C_{FCE} can be expressed as:

$$C_{FCE} = C_{FCE(pp)} + 2C_{FCE(fringe)}$$
$$= \varepsilon_0 \varepsilon_r \frac{WL_{FCE}}{t_{ox}} + 2C_{FCE(fringe)} \tag{3.4.17}$$

Here, ε_0 is the permittivity of free space, ε_r is the relative permittivity of air, W is the device width, L_{FCE} is the FCE length, and t_{ox} is the gate oxide thickness. The gate terminal makes two parallel plate capacitance with FCE on each side and can be expressed as:

$$C_{g-FCE} = \varepsilon_0 \varepsilon_r \frac{Wt}{L_{g-FCE}} \tag{3.4.18}$$

The total gate to source capacitance, $C_{gs(total)}$ and $C_{gd(total)}$ after adding FCEs turn out to be

$$C_{gs(total)} = C_{gs} + \frac{C_{FCE} \times C_{g-FCE}}{C_{FCE} + C_{g-FCE}}$$
$$C_{gd(total)} = C_{gd} + \frac{C_{FCE} \times C_{g-FCE}}{C_{FCE} + C_{g-FCE}} \tag{3.4.19}$$

If an FCE of length L_{FCE} is placed at the access region of length L_{acs}, then the new expression for R_S and R_D becomes

$$R_D = R_S = R_C + \frac{(L_{acs} - L_{FCE})}{W \mu e n_0} + \frac{L_{FCE}}{W \mu e (n_0^2 + n_{FCE}^2)^{1/2}} \tag{3.4.20}$$

The induced carriers n_{FCE} caused by FCE modulation effectively reduces the resistance of the ungated access regions and thus results in a decrement of τ_{par} and increment of f_T.

Small Signal Circuit Analysis of Bottom FCE GFET
In this part of this report, we study the theory of the proposed device consisting of two independently biased capacitively coupled contacts placed at the access regions on bottom of the GFET as shown in Figure 3.4.13. As like as the top FCE GFET, the FCEs on the bottom of the device are independently biased and capacitively coupled to the channel.
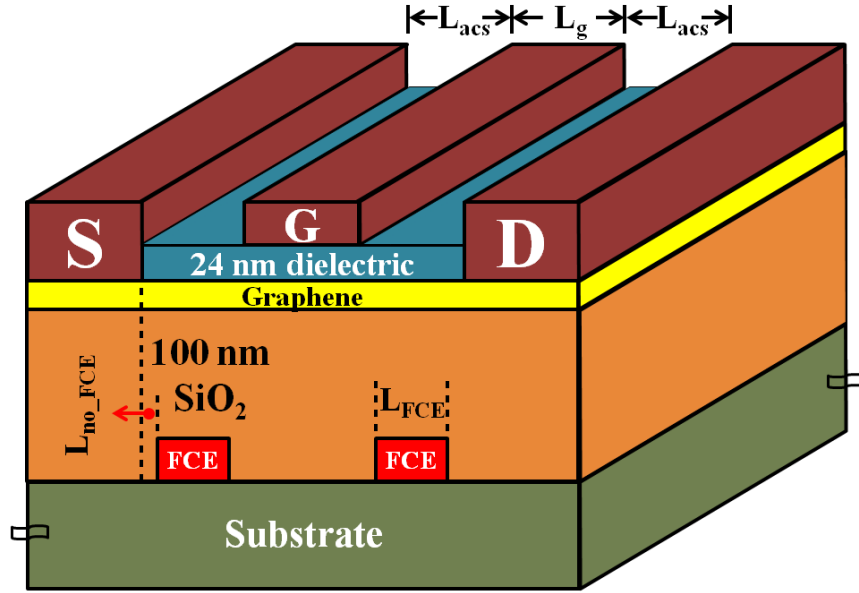
Figure 3.4.13: Schematic of the proposed GFET with 2 bottom FCEs at the ungated region

The independently biased FCEs induce additional carriers at the access region according to eqn. 16 As proposed, an FCE of length L_{FCE} placed at the access region of length Lacs making two no-FCE regions on both sides each having a length of L_{no_FCE} changes the expression of R_S and R_D as follows-

$$R_S = R_D = 2R_C + \frac{4L_{no\_FCE}}{\mu e n_0 . W} + \frac{2L_{FCE}}{\mu e (n_0^2 + n_{FCE}^2)^{1/2} W} \qquad (3.4.21)$$

The resistance of the ungated access regions decreases by the induced carriers n_{FCE} due to FCE modulation which results in a decrement of τ_{par} and increment of f_T. In this device, the key advantage is the ease of fabrication with high tolerance, because the FCEs are to be patterned on a different layer other than the gate layer. In addition to that, the larger distance between FCEs and gate will result in lower parasitic capacitances.

Small Signal Circuit Analysis of Hybrid Contact GFET
In this part, we have proposed, studied, and extensively analyze a GFET with hybrid contacts capable to reduce the access resistance and contact resistance of the device, simultaneously.

42
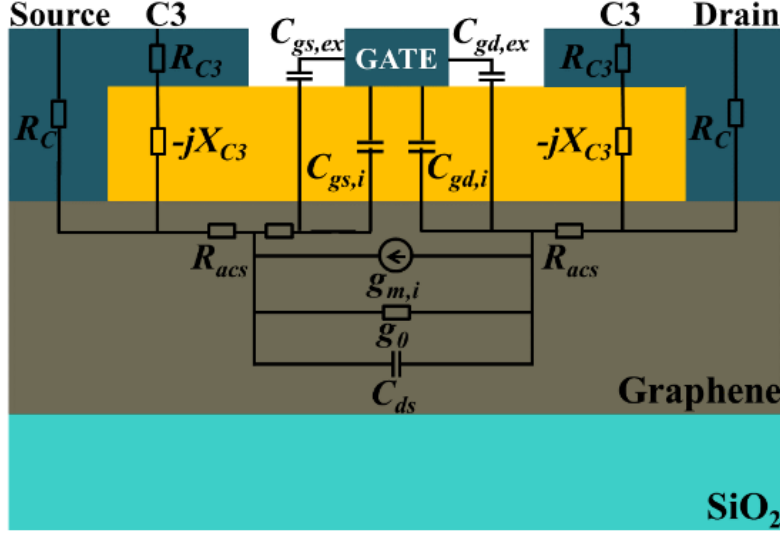
Figure 3.4.14: Small signal equivalent circuit overlaid on top of the proposed hybrid contact Graphene FET

The hybrid contact consists of a ohmic contact having capacitive extension towards the Gate. The capacitively coupled part of the contact reduces the contact resistance and provides a low resistance path for the high frequency signal. In addition, the extension towards Gate reduces the access region length and the associated resistance—the access resistance. Small signal equivalent circuit of the proposed hybrid contact GFET overlaid on the device schematic is shown in Figure 3.4.14.

If two capacitively coupled contacts (C3s) are placed on the access regions and connected to the ohmic Source/Drain as shown in Figure 3.4.2, the C3 will make a path for high frequency RF signal parallel to the ohmic contact. The C3 impedance $Z_{C3}=R_{C3}-jX_{C3}$ consists of real and imaginary parts and the total contact impedance comes to be $Z_C = R_C\|Z_{C3} = R_C\|(R_{C3}-jX_{C3})$. After rearrangement and simplification, Z_C can be expressed as:

$$Z_C = \frac{R_C^2 R_{C3} + R_{C3}^2 R_C + X_{C3}^2 R_C}{(R_C + R_{C3})^2 + X_{C3}^2} - j\frac{X_{C3}R_C^2}{(R_C + R_{C3})^2 + X_{C3}^2} = R_C' - jX_C'$$

(3.4.22)

Assuming the length of C3 is L_{C3}, the access region length of the hybrid contact GFET comes to be $L_A' = L_A - L_{C3}$ and the new expression for Source/Drain impedance and total channel impedance become as follows:

$$Z_D = Z_S = Z_C + R_A' = R_C' - jX_C' + (L_A' / \mu q n_0 W)$$
$$Z_{SD} = 2Z_D + R_{CH} = R_{SD} - jX_{SD}$$

(3.4.23)

From the equation above, we can see that the total channel resistance has real part as well as an imaginary part. A simple matching network can be designed for matching and eliminating the imaginary part of the input impedance. An impedance matching network is an additional circuit that consists of a reactive element of such a value that can effectively nullify the opposite signed reactive element of the device and thus eliminate the effective reactance of the whole system. It

can be achieved with only 2 reactive elements that transform both the real and imaginary part. A common 2 reactive element configuration is referred to as L-section matching network as shown in Figure 3.4.3(a).
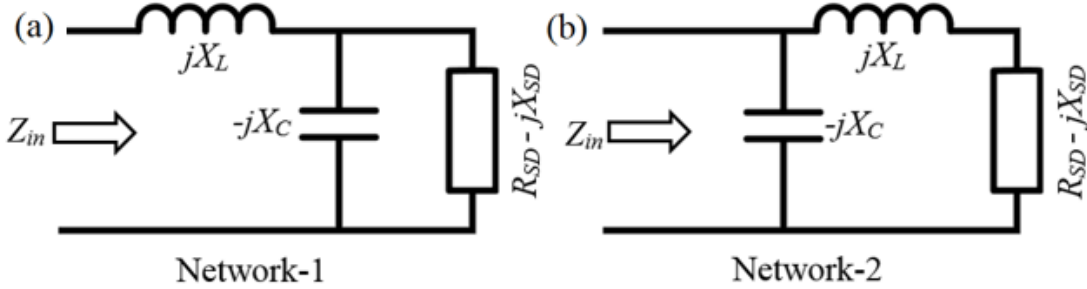

Figure 3.4.15. (a) Matching Network-1 (b) Matching Network-2.

Considering network-1, we can quantify the input impedance as:

$$Z_{in} = jX_L + \frac{R_{SD} + jX_{SD}}{1 + jX_C R_{SD} - X_C X_{SD}}$$

(3.4.24)

To match it with a resistance R, we consider $Z_{in}=R$ and after equating the real and imaginary parts, we get:

$$X_L = \frac{1}{X_{CAP}} + \frac{X_{SD}R}{R_{SD}} - \frac{R}{X_{CAP}R_{SD}}$$

$$X_{CAP} = \frac{X_{SD} \pm \sqrt{\frac{R_{SD}}{R}}\sqrt{R_{SD}^2 + X_{SD}^2 - RR_{SD}}}{R_{SD}^2 + X_{SD}^2}$$

(3.4.25)

By solving these equations, we can determine the capacitor and inductor values required to nullify imaginary part of contact impedance. These two relations are derived for network-1 and are valid if $R_{SD}>R$. On the other hand, if $R_{SD}<R$, network-2 as shown in Figure 3.4.3(b) needs to be used and after following the same procedure, we can estimate X_L and X_{CAP} as follows:

$$X_L = \pm\sqrt{R_{SOURCE-DRAIN}(R - R_{SOURCE-DRAIN})} - X_L$$

$$X_{CAP} = \pm\frac{\sqrt{(R - R_{SOURCE-DRAIN})/R_{SOURCE-DRAIN}}}{R}$$

(3.4.26)

For devices working on a wide frequency range, a very common technique in RF/mobile communication named "frequency transformation technique" needs to be used, as reported in [47].

Once the matching network has been used, only the real part of contact resistance R'$_c$ remains and the new expression of source/drain resistance comes out to be:

$$R_D = R_S = R'_C + (L'_A / \mu q n_0 W)$$
(3.4.27)

One can easily get the relation between f_T and Z_C by plugging this new R_S and R_D into the f_T equation in (3.4.5).

The C3 can be considered as a RC transmission line and its impedance can be analytically calculated. If a C3 is placed on top of Gate dielectric, the contact metal and Graphene channel with in-between dielectric material form a RC transmission line. The propagation constant γ and characteristics impedance Z_0 of this transmission line can be estimated by the following equations:

$$\gamma = \sqrt{i2\pi R_{sh}C}, Z_0 = \frac{1}{W}\sqrt{\frac{R_{sh}}{i2\pi fC}}$$
(3.4.28)

where, R_{sh} is sheet resistance of Graphene channel, C is the metal to Graphene capacitance per unit area, W is the width and f is the frequency. The C3 impedance can be estimated equal to the input impedance of this open ended transmission line as follows:

$$Z_{in} = Z_0\coth(\gamma L_{C3})$$
(3.4.29)
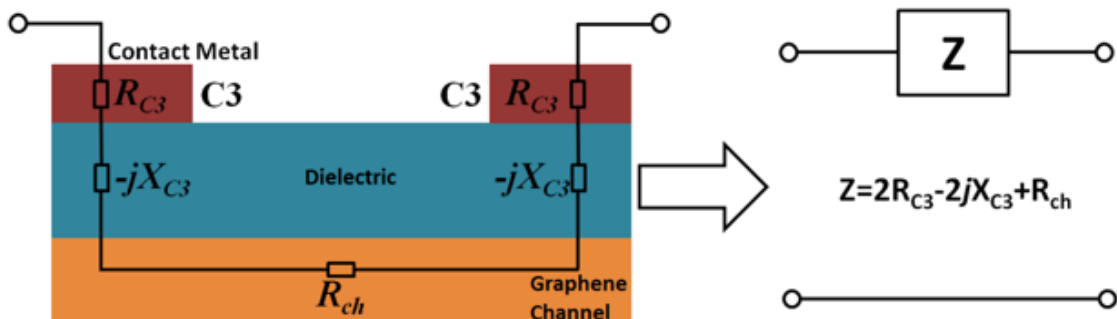
Figure 3.4.16. Schematic of a RF TLM structure on Graphene with small-signal equivalent circuit overlaid on top and the equivalent 2-port network

In simulation, the impedance of C3s can be calculated by using RF Transmission Line Method (TLM) structures with multiple C3s with various in-between distances. Two C3s and the Graphene channel in-between is a Two-Port network as shown in Figure 3.4.4 and its impedance can be estimated by extracting the 2 port S-Parameters and converting them to B-Parameter. The real and

[47] S. Dutta Roy, IETE Journal of Education, vol. 55, no. 1, pp. 47-51 2014.

imaginary parts of B-parameter are actually the real and imaginary parts of total impedance of the two port network—two C3 impedance in addition to in-between Graphene channel resistance.

Simulation of Top FCE GFET

Here we simulate and analytically estimate the performance of the top FCE GFET and compare with the conventional ones. The baseline conventional GFET in this study was chosen similar to the one reported in [48]. We name it as GFET-A. It consists of 3.0 μm long gate and 1.5 μm long access region having SiO_2 as substrate and Al_2O_3 with SiO_2 as gate dielectric as shown in Figure 17 (a). Using the reported characteristics, residual carrier (hole) concentration at the Graphene channel is extracted as 7.02×10^{12} cm^{-2} at $V_{GS}=0$ which results in an access resistance of $R_{acs}=25.2$ Ω for the device width of 100 μm. We simulated the DC and RF characteristics of the baseline GFET using physics based numerical device simulation tool with parameters modified for Graphene. This type of simulation approximates the operation and transportation of carriers through the structure by applying a set of differential equations including Poisson's Equation, Carrier Continuity Equations and Drift-Diffusion Equation, derived from Maxwell's laws, onto a 2D grid, consisting of a number of grid points called nodes. This way the electrical performance of a device can be modeled in DC, AC or transient modes of operation. The results presented in Figure 3.4.17 (b) are in good agreement with the measured characteristics in the above reference which validate our simulation method where the contribution of both the electrons and holes to the drain current is considered. For the baseline GEFT, f_T and f_{MAX} are extracted as 1.0 GHz and 1.2 GHz, respectively. Operating regime (electron or hole) of the device can be chosen by biasing the gate on either side of Dirac point to make one type of carriers dominant. The total device current on either regime is still supported by the low density residual carriers at the ungated access regions causing high source/ drain resistance which adversely affect the RF performance.
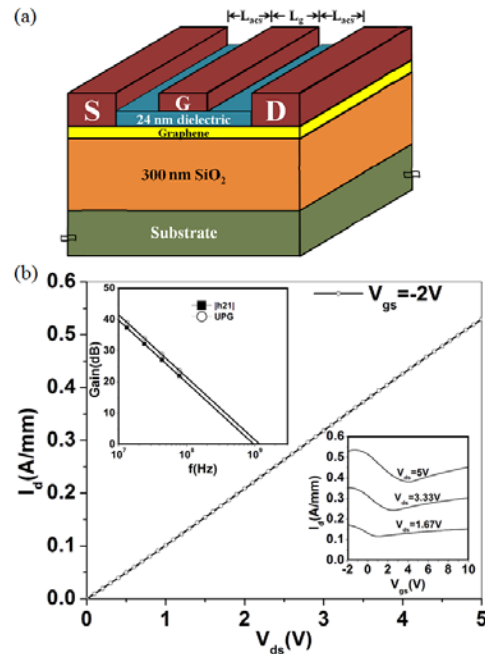

Figure 3.4.17: (a) Schematic of the baseline GFET-A, (b) DC and RF characteristics (Current Gain, |h$_{21}$| and Unilateral Power Gain, UPG) of the baseline GFET-A from simulation.

---

[48] O.M. Nayfeh, IEEE Transactions on, vol. 58, no. 9, pp. 2847-2853 2011.

In the proposed device, two capacitively coupled FCEs are placed at the ungated access regions as already shown in Figure 3.4.12 (b). As the transistor action of the device takes place at the gate terminal, the additional DC bias at the FCEs will help supporting the total device current in either of the transportation regimes by selective population of particular type of carriers at the access regions.

We consider two devices for our analysis: (i) GFET-A; the long channel device with L_g=3.0 μm, L_{acs}=1.5 μm, μ_h=530 cm^2/V.s and μ_e=336 cm^2/V.s and (ii) GFET-B; the short channel device with L_g=0.5 μm, L_{acs}=1.5 μm, μ_e=4900 cm^2/V.s and μ_h=3100 cm^2/V.s. Analytical calculations using the equations above show that for GFETs with a typical residual carrier (hole) concentration of 4.8× 10^{12} cm^{-2}, the GFET-A, the long channel low mobility device with two 1.3 μm long FCEs each biased at -3 V can lower the R_{acs} of an initial value of 36.8 Ω down to 20 Ω.
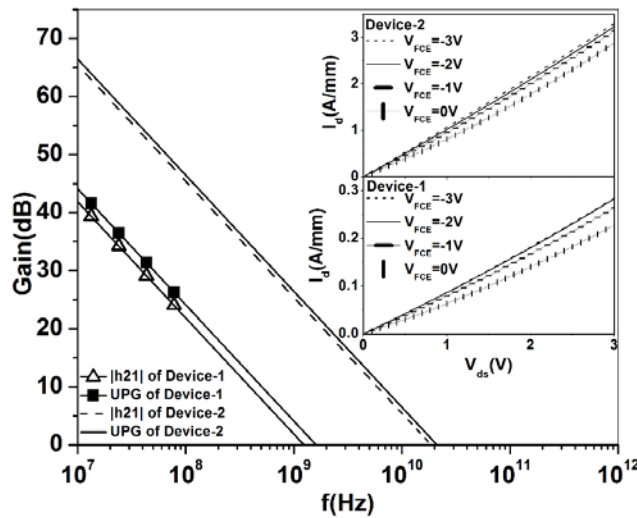

Figure 3.4.18: RF characteristics of both GFET-A and GFET-B with V_{FCE}=-3V and V_{gs}=-2V. Inset shows the I_d-V_d characteristics of GFET-A & B with V_{FCE} in hole transportation regime at V_{gs}=-2V considering concentration dependence of the hole mobility.

The minimization of R_{acs} makes the f_T of Device-1 to be 1.47 GHz whereas the f_T of this device with V_{FCE}=0 is 1.1 GHz calculated for hole transportation regime. Similar minimization of access resistance due to biased FCE makes the f_T of GFET-B; the short channel high mobility device to be 22.1 GHz which has a value of 16.9 GHz at V_{FCE}=0 also for hole regime operation.

The numerical device simulation tool was used to simulate the proposed novel GFET with residual carrier (hole) concentration of 4.8×10^{12} cm^{-2} same as that used for baseline device simulation and analytical calculations. The RF characteristics at V_{gs}=-2V (hole regime) and V_{FCE}= -3V along with the I_d-V_{ds} characteristics with FCE bias of both GFET-A and GFET-B are shown in Figure 3.4.18. The I_d-V_{ds} characteristic is depicting the decrement of R_S and R_D due to the decrement of R_{acs} by FCE bias.
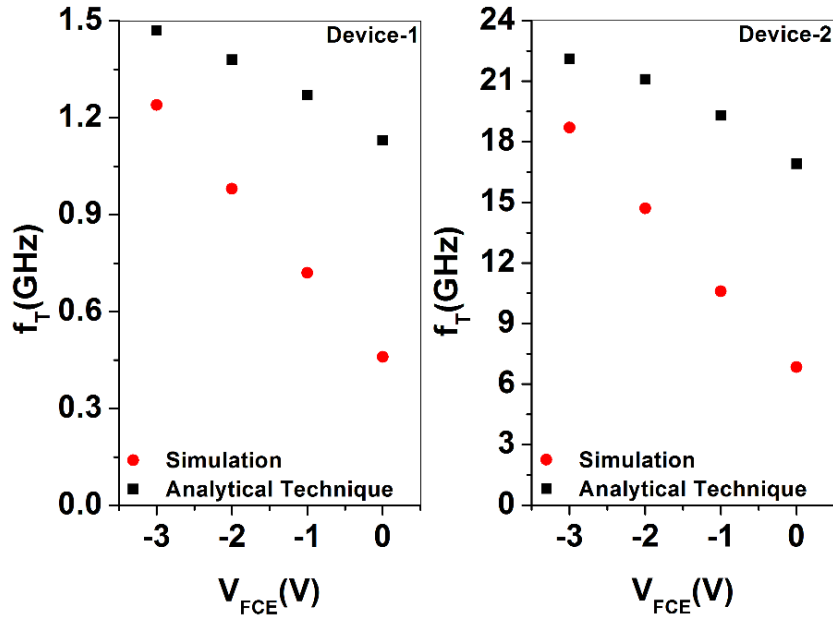
Figure 3.4.19: Improvement of f_T with V_{FCE} for both GFET-A and GFET-B in hole regime.

The improvement of RF characteristics with FCE bias estimated using both analytical and numerical techniques for hole regime is shown in Figure 3.4.19. It was reported that carrier mobility did not show significant dependence on carrier concentration in the range of concentration we worked. Therefore, the hole mobility for the GFET-A value was kept constant at 530 cm^2/V.s throughout the entire range of FCE in both analytical and numerical analyses.
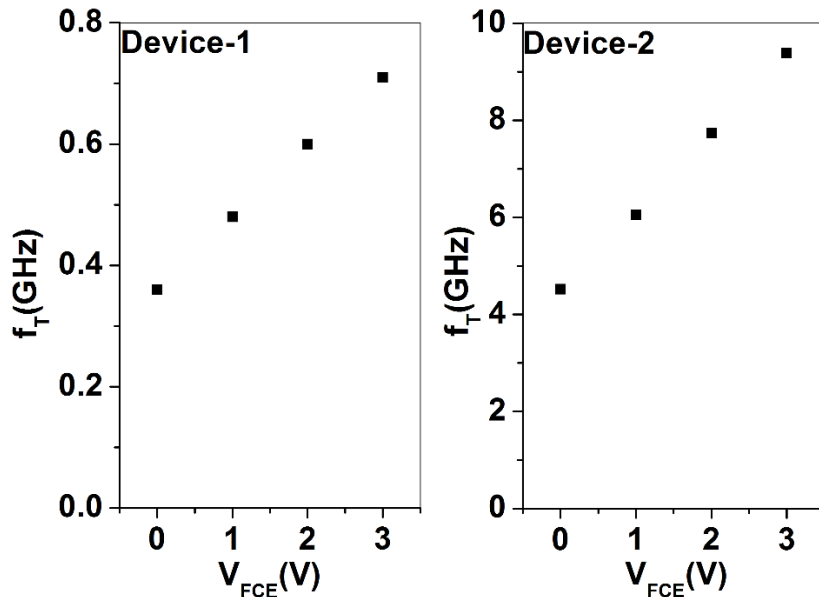

Figure 3.4.20: Improvement of f_T with V_{FCE} for both GFET-A and GFET-B in electron regime at V_{gs}=6.0 V (numerical simulation results).

On the other hand, Graphene hole mobility was considered to be significantly dependent on carrier concentration for the GFET-B, and its values at V_{FCE}=0, -1, -2, and -3V were estimated using the

data in [49] for all analyses. The analytical technique resulted higher cutoff frequency compared to that obtained from numerical simulations because of the limitations to take the additional parasitic capacitances introduced due to the FCE contacts into account.

One can expect similar improvement of f_T while the GFET is in electron transport regime. Such improvement is estimated using the simulation tool considering similar concentration dependent mobility of electrons for GFET-B and shown in Figure 20.

Simulation of Bottom FCE GFET
To improve the RF performance we added FCEs at the 1.5 μm long ungated regions on bottom of GFET-A as already shown in Figure 3.4.13. As we cannot make the gate dielectric so thick that the gate loses good control over the channel, we have a limitation on the gate voltage too not to surpass the gate dielectric breakdown electric field. As the dielectric between FCEs and channel is much thicker compared to the gate dielectric, the FCE voltage was much higher than the gate voltage. To determine the optimum FCE length and position providing maximum f_T for GFET-A, we placed FCEs of different lengths at the center of the access regions leaving two equal no_FCE regions both sides and simulated the RF performance at V_{FCE}= -9V which represents an electric field moderately lower than the breakdown electric field of SiO$_2$. It was reported that carrier mobility did not show significant dependence on carrier concentration in the range of concentration we consider here. Therefore, the hole and electron mobility was kept constant at 530 cm^2/V.s and 336 cm^2/V.s respectively for V_{FCE}= -9V as well as for rest of the analyses performed on GFET-A throughout the entire range of FCE bias. The dependence of f_T over L_{FCE} shown in Figure 3.4.21 (a) reveals that two 1.4 μm long FCEs at the access regions leaving 50 nm no_FCE regions on each side is the optimum condition in this case. Keeping the Source/Drain to FCE distance ($L_{s/d-FCE}$) unchanged to 50 nm, we gradually decreased the Gate to FCE distance down to zero (FCE edge aligned to Gate edge) and plotted f_T against them as shown in Figure 3.4.21 (b). The decrement of L_{g-FCE} showed deterioration of f_T rather than improvement here. At L_{g-FCE}= 50 nm, we later decreased the $L_{s/d-FCE}$ from 50 nm down to zero gradually. This time, the decrement of $L_{s/d-FCE}$ increased the f_T as shown in Figure 3.4.21 (c).

From Figure 3.4.21, the optimum L_{FCE}, $L_{s/d-FCE}$ and L_{g-FCE} were found 1.45 μm, 0 μm and 50 nm respectively. Using the FCEs with optimum length and position, for hole regime operation of GFET-A (V_{gs} = -2.0 V), the DC simulations showed that the drain current increased with increasing negative FCE bias (V_{FCE}) shown in Figure 3.4.22, which reveals reduction of access resistance.

---

[49] X. Du *et al.* vol. 3, no. 8, pp. 491-495 2008
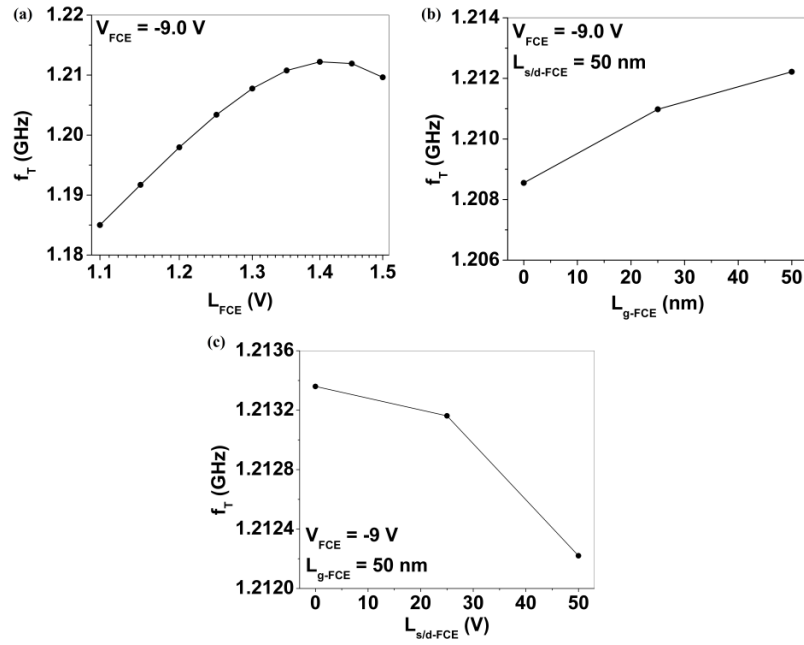
Figure 3.4.21: At V_{FCE}= - 9 V (a) f_T plotted against different L_{FCE}. (b) At $L_{s/d\text{-}FCE}$ =50 nm, f_T plotted against $L_{g\text{-}FCE}$. (c) At $L_{g\text{-}FCE}$ = 50 nm, f_T plotted against $L_{s/d\text{-}FCE}$.

Analytical calculations based on the equations presented above were used to quantify the reduction and was found that for L_{gs}/ L_{gd}=1.5 μm with FCEs of optimum size and position, the access resistance R_{acc}=36.8 Ω of the baseline device went down to 23.0 Ω at V_{FCE} = -9 V.
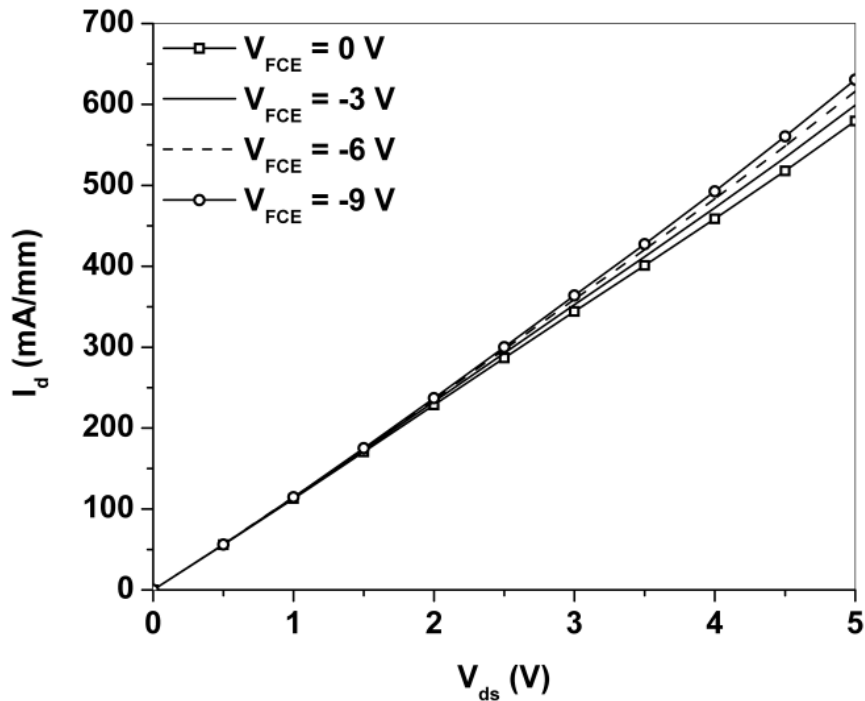
Figure 3.4.22: Increment of drain current with FCE bias at V_{ds} = 5.0 V and V_{gs} = -2.0 V.

50

We used analytical and numerical investigation to estimate the RF improvement in both electron and hole regime of operation. Fig. 3.4.5 (a) shows the simulated current gain, $|h_{21}|$ - frequency relationship of the device for the DC biasing conditions of $V_{gs} = -2$ V, $V_{ds} = 5$ V which represents hole regime operation of GFET-A and for different FCE biases. The current gain cutoff frequency, f_T was extracted from the data in Figure 3.4.23 (a) and compared to the ones analytically calculated in Figure 3.4.23 (b). As the simulation tool estimates the transportation of carriers through the structure by applying differential equations onto the nodes of a 2D grid, it was capable of including the additional capacitances arisen due to the presence of the additional contacts (FCEs) by itself. To include them in the analytical calculation part, we modified the capacitance values of C_{gs} and C_{gd} in the RF equations derived for conventional 3-terminal FETs by calculating the FCE capacitances using geometric and material parameters. Considering the device width to be 100 µm, each of C_{gs} and C_{gd} valued 3.90×10^{-13} F calculated for conventional 3 terminal GFET and after inclusion of additional capacitances due to FCEs, it became 4.40×10^{-13} F.
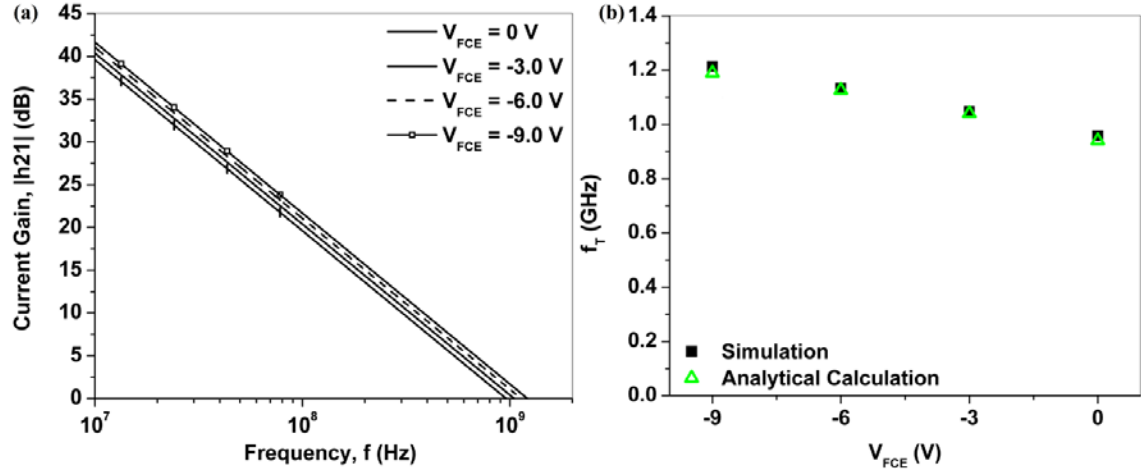

Figure 3.4.23: (a) Current gain $|h_{21}|$ - frequency relationship of the GFET-A with FCEs at varying V_{FCE} values in hole regime of operation. (b) f_T vs. V_{FCE} where f_T is calculated using analytical technique and also extracted from (a).

For electron regime of the same device, DC biasing of $V_{ds} = 5$ V and $V_{gs} = 6$ V was considered for similar analytical and numerical estimation of the cut off frequency, f_T. The f_T of baseline GFET-A in this condition was extracted to be 0.57 GHz. Figure 3.4.24 (a) shows the $|h_{21}|$-frequency relationship of GFET-A with FCEs at different V_{FCE} and the extracted f_T values along with those from analytical technique are plotted against V_{FCE} in Figure 3.4.24 (b).

We also explored the effect of biased FCEs on RF improvement in short channel high mobility GFETs. The baseline GFET chosen for this analysis is similar to the one reported in [50]. The device has CVD-grown Graphene channel with carrier mobility of $\mu = 2234$ cm^2/ V.s on sapphire substrate with $L_g = 210$ nm, $L_{sd} = 1.5\,\mu$m and named as GFET-B. Considering the device geometry to be symmetrical, access region length is $L_{gs} = L_{gd} = 645$ nm.

---

[50] H. Wang *et al.* American Physical Society, APS March Meeting 2012, February 27-March 2, 2012, abstract #J7.015
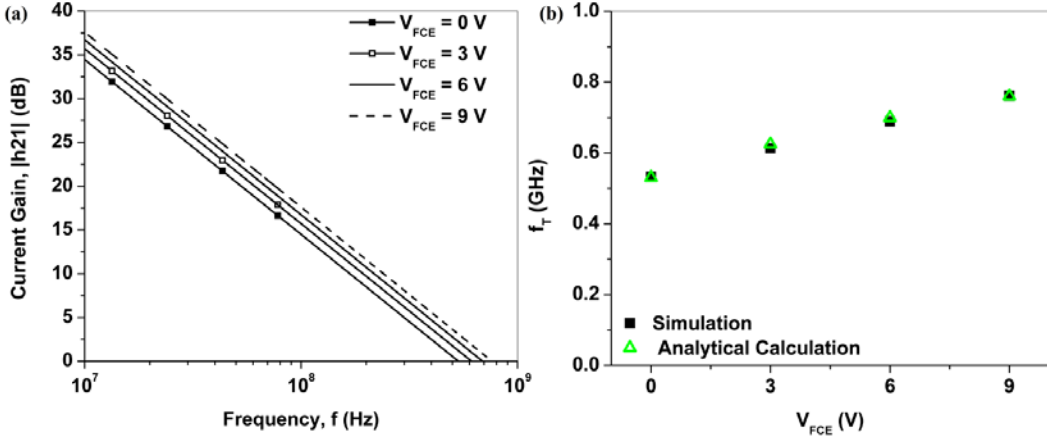
Figure 3.4.24: (a) Current Gain |h21| - Frequency relationship of GFET-A with FCEs at different V_{FCE} values in electron regime of operation. (b) f_T vs. V_{FCE} where f_T is calculated using analytical technique and also extracted from (a).

The simulated RF performance of the baseline device presented in Figure 3.4.25 is in good agreement with the reported one after de-embedding. f_T and f_{MAX} were extracted as 22.1 GHz and 23.3 GHz, respectively. To improve the RF performance, FCEs are added on bottom of two 645 nm long ungated regions and biased up to ±9.0 V as before not to exceed the breakdown voltage of Al_2O_3 reported in [51]. Graphene hole and electron mobility was considered to be significantly dependent on carrier concentration and their values at different V_{FCE} were estimated using the data in the reference for all analyses.

To determine the optimum FCE length and position for GFET-B, we placed FCEs of different lengths as before and simulated the RF performance. The dependence of f_T over L_{FCE}, L_{g-FCE} and $L_{s/d-FCE}$ shown in Figure 26 reveals that the optimum values of L_{FCE}, $L_{s/d-FCE}$ and L_{g-FCE} are 495 nm, 0 nm and 150 nm respectively.
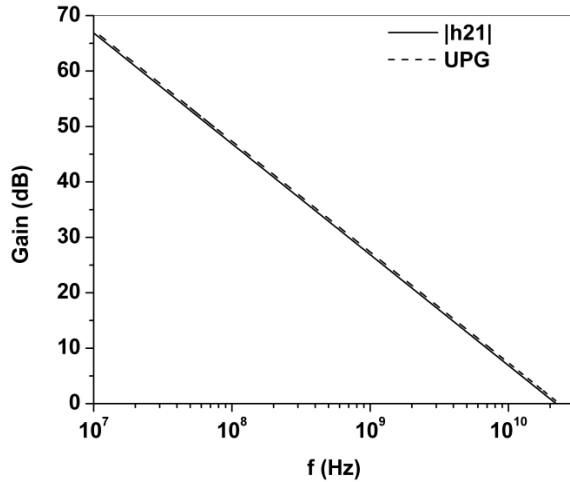

Figure 3.4.25: Current Gain and Unilateral Power Gain vs. frequency of the short channel high mobility baseline GFET.

---

[51] M. Groner, *et al.* Thin Solid Films, vol. 413, no. 1, pp. 186-197 2002.

Using the optimum FCE length and position, we estimated the RF improvement in both electron and hole regime of operation using both simulations and analytical technique. Analytical calculation showed that the access resistance of 645 nm long access region with an initial value of 3.66 Ω went down to 2.31 Ω for $V_{FCE} = -9$ V. In frequency domain AC simulations, a biasing condition of $V_{ds} = -1.6$ V, $V_{gs} = -0.6$ V was assumed for hole regime and $V_{ds} = -1.6$ V, $V_{gs} = 1$ V was assumed for electron regime.
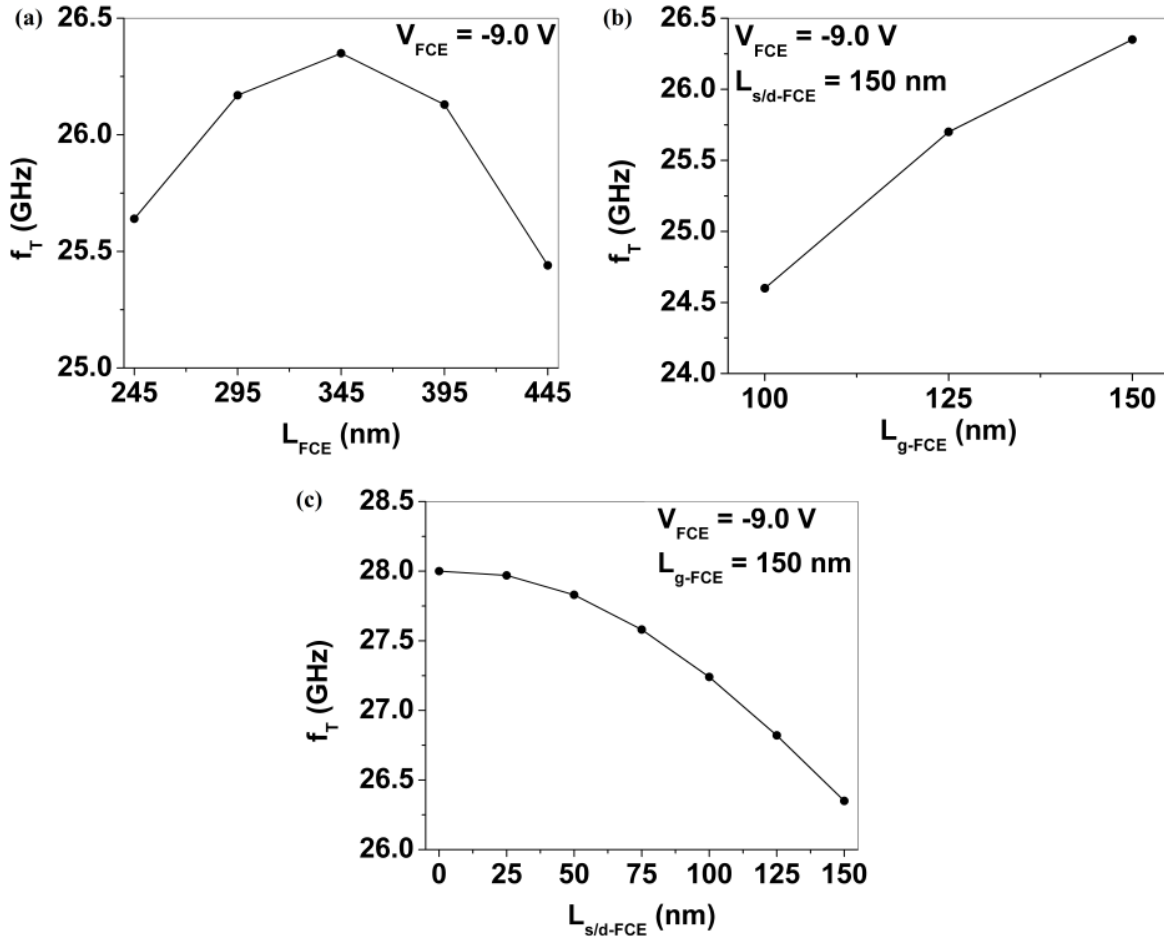
Figure 3.4.26: At $V_{FCE} = -9$ V (a) f_T plotted against different L_{FCE}. (b) At $L_{s/d\text{-}FCE} = 150$ nm, f_T plotted against $L_{g\text{-}FCE}$. (c) At $L_{g\text{-}FCE} = 150$ nm, f_T plotted against $L_{s/d\text{-}FCE}$.

The extracted f_T values from the frequency response for hole regime along with those from analytical calculation using modified RF equation for 5-terminal GFET are plotted against V_{FCE} in Figure 3.4.27 (a) whereas that for electron regime in Figure 3.4.27 (b).
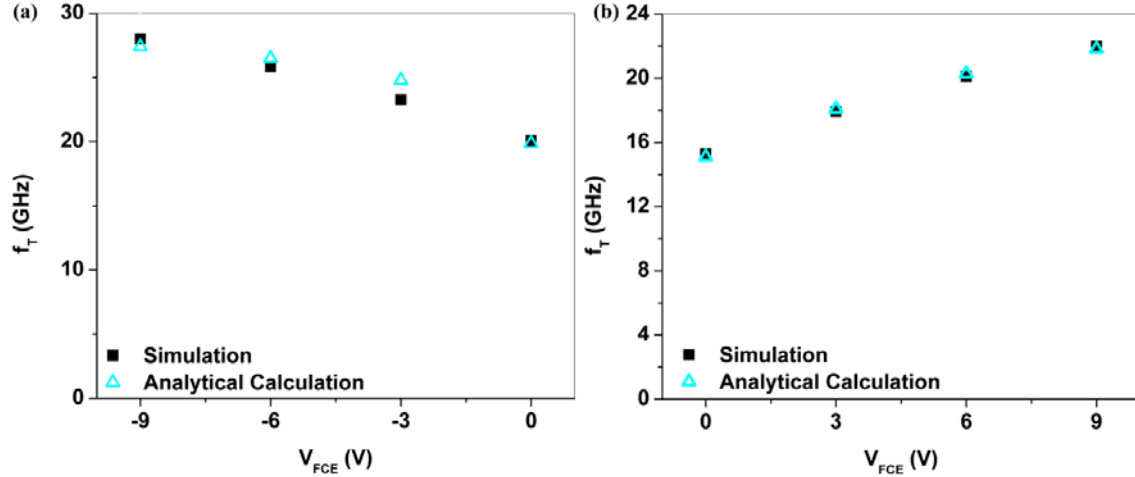
Figure 3.4.27: Extracted f_T from frequency response and from analytical calculations plotted against V_{FCE} for (a) hole regime operation and (b) electron regime operation.

Simulation of Hybrid Contact GFET

We aim to add two C3s on this device and short them to the ohmic contacts to extensively analyze its effect on the device's high frequency performance. As a starting point of capacitive impedance simulation, we first simulated a simple capacitor-like structure. It consists of 30nm SiO_2 between two metal contacts and each metal contact has a contact resistance of 0.7 ohm-mm, shown in Figure 3.4.28 (a).
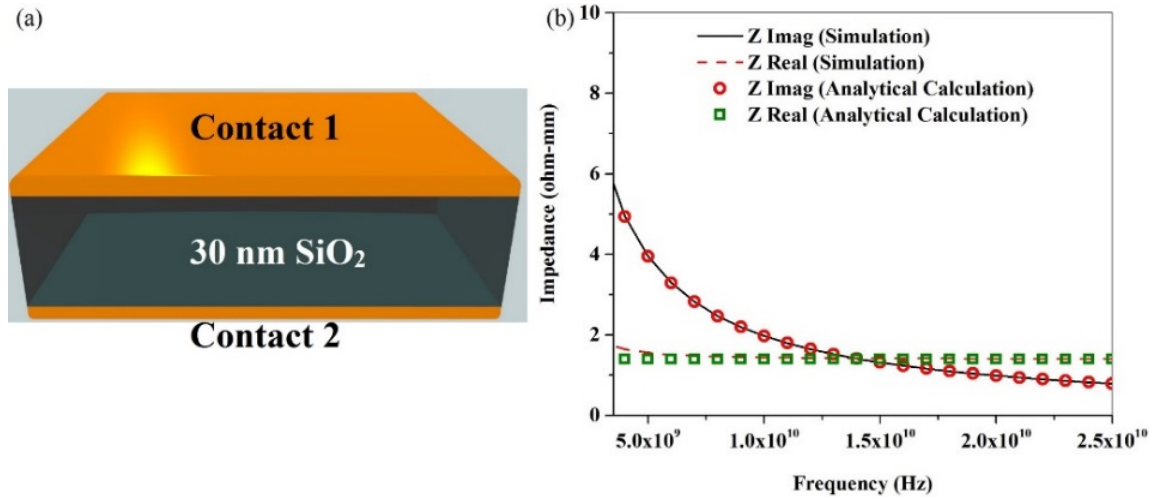
Figure 3.4.28: (a) Schematic of the capacitor like structure (b) The real and imaginary part of impedance estimated from simulation and analytical calculation.

The real and imaginary parts of this capacitive impedance are estimated using simulation as well as analytical technique. In Figure 3.4.28 (b), the real and imaginary part of capacitive impedance estimated from simulation and analytical calculations are plotted with respect to frequency. We can see that the results using both of the methods are in a very good agreement, which validates our simulation technique of estimating capacitive impedance. For further verification, we

successfully regenerated the experimental data for III-N RF TLM structures reported in [52]. To estimate the impedance of the capacitance formed between a C3 and Graphene channel with Gate dielectric in-between, we simulated a RF TLM structure on Graphene having two C3s with various in-between distances.

The C3s were placed on exactly the same structure, as in baseline GFET-1, consisting of 9 nm SiO$_2$ and 15 nm Al$_2$O$_3$ serving as Gate dielectric deposited on CVD Graphene with carrier mobility same as that of baseline GFET-1, shown in Figure 3.4.17 (a). The impedance between contact 1 & 2, 2 & 3, and 3 & 4 were calculated at a specific single frequency, plotted with respect to distance, and extrapolated up to zero distance to extract the real and imaginary part of a single C3 impedance at that frequency. This procedure was repeated over the frequency range of 5 GHz to 25 GHz with a step size of 1 GHz. The real and imaginary part of C3 impedance plotted with respect to frequency is shown in Figure 29 (b).
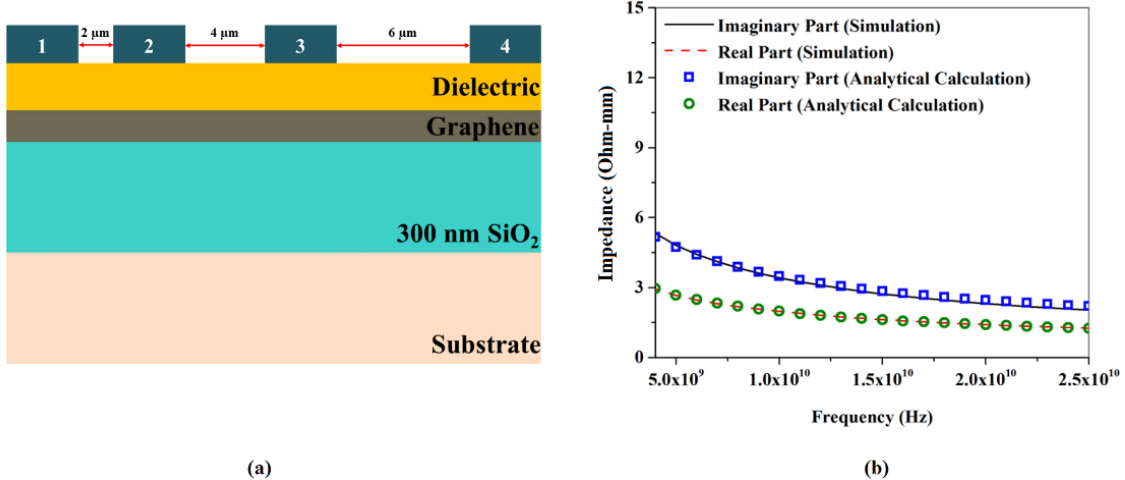

Figure 3.4.29: (a) Schematic of RF TLM structure on Graphene. (b) The real and imaginary part of C3 impedance estimated from both simulation and analytical calculations plotted with respect to frequency.

Finally, we simulated the proposed GFET which has two C3s shorted to the ohmic Source/Drain contacts of the already simulated baseline GFET-1, shown in Figure 3.4.30. The length of capacitively coupled extension was 0.8 µm in this simulation. The Current Gain, |h21| of the baseline GFET-1 and the proposed modified version with C3s are plotted with respect to frequency in Figure 31 (a). According to definition, the frequency at which current gain becomes 0 dB is the current gain cut-off frequency, f_T. We can see from Figure 3.4.31 (a) that for a C3 length of 0.8 µm, the f_T of this proposed GFET reached a value of 0.78 GHz whereas that for the baseline GFET-1 was 0.74 GHz. In each and every numerical calculation, the gate to source/drain parasitic capacitances have been considered. In addition to that, in analytical calculations, the parasitic capacitances have been estimated using geometric and material parameters. The value of these parasitic capacitances ranged from 3.90×10^{-13} F to 4.40×10^{-13} F.

The drain to source voltage as well as the drain side C3 to source voltage, V_{ds} was 5.0 V during frequency domain AC simulation. As the drain bias as well as the drain side C3 bias is positive,

[52] G. Simin, *et al.* Appl.Phys.Lett., vol. 89, no. 3, pp. # 033510 2006.

we considered the GFET electron regime operation so that the drain side C3 bias accumulate more major carriers (electrons) underneath. A Gate bias of V_{gs}=2V was used to operate the GFET in electron regime.
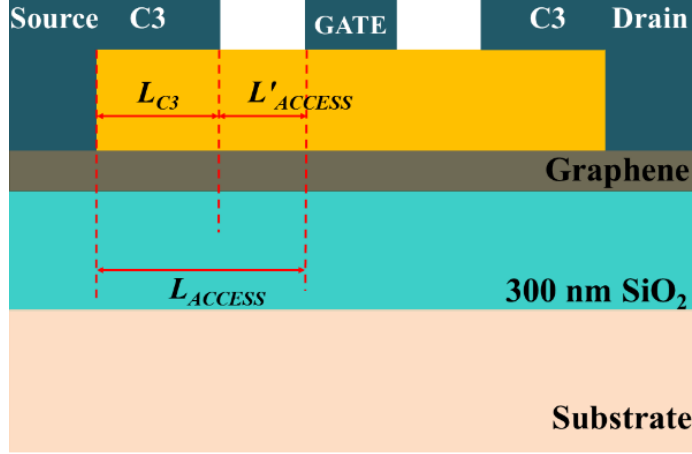
Figure 3.4.30: Schematic of the proposed GFET (not in scale).

We later gradually increased the length of C3s. The approaching C3 towards Gate reduced access region length as well as access resistance. Also the increment of capacitive coupling area due to C3 length increment decreased capacitive impedance. As a result of access resistance decrement as well as the decrement of capacitive impedance, the f_T of the proposed GFET further increased. The effect of increased C3 length over f_T for this device is shown in Figure 3.4.31 (b) estimated from both simulation and analytical calculation. We can find from Figure 3.4.31 (b) that the f_T of this proposed device reached a value of 0.89 GHz for a C3 length of 1.4 μm whereas it was just 0.78 GHz for C3 length of 0.8 μm before. Further increment of C3 length was studied and due to introduction of high parasitic capacitance, that resulted in f_T deterioration.
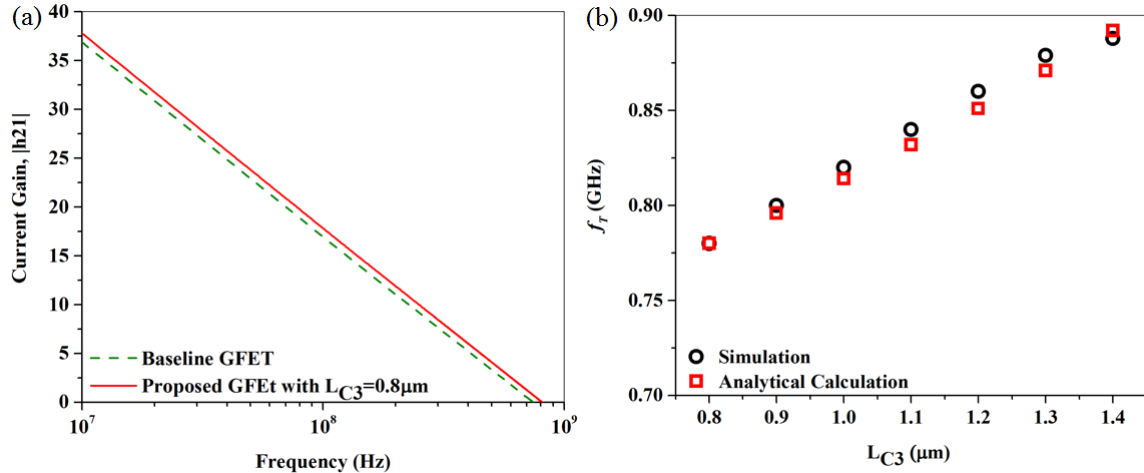
Figure 3.4.31: (a) Current Gain, |h21| of the baseline GFET-1 along with that of the proposed hybrid contact GFET in electron regime (V_{gs}=+2.0 V and V_{ds}=+5.0 V) plotted with respect to frequency (b) The current gain cut-off frequency (f_T) of the proposed GFET extracted from |h21|vs f characteristics, plotted with respect to L_{C3}.

56

As the C3 impedance is dependent on frequency and from our results in Figure 3.4.29 (b), it was found that the real part of C3 impedance is reduced at higher frequencies; we intended to quantify the effect of C3 on RF performance of a shorter channel higher mobility GFETs. To do so, as before, a short channel high mobility GFET reported by Wang *et al.* (see above) was chosen as our short channel high mobility baseline and named it as GFET-2.

The device has CVD-grown Graphene channel with carrier mobility of μ = 2234 cm^2/ V.s on sapphire substrate with gate length of 210 nm, Source to Drain distance of 1.5 μm. We considered the device geometry to be symmetrical and estimated the access region length to be 645 nm on each side of the Gate. We simulated the DC and RF characteristics of the baseline GFET-2 as before and they were in a very good agreement with the reported data. For this simulation as well as for the following simulations and analytical calculations, the device width was considered to be 100 μm as before. Later we simulated our proposed short channel high mobility GFET with hybrid contact by making a capacitive extension of 245 nm of both Source and Drain towards Gate.
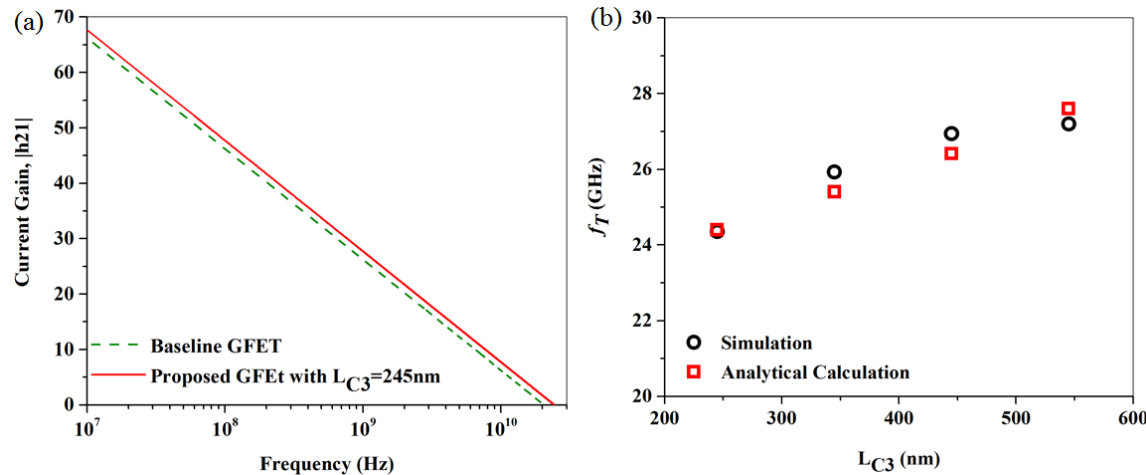

Figure 3.4.32: (a) Current Gain, |h21| of the baseline GFET-2 along with that of the proposed hybrid contact GFET in electron regime (V_{gs}=+0.6 V and V_{ds}=+1.6 V) plotted with respect to frequency (b) The current gain cut-off frequency (f_T) of the proposed GFET extracted from |h21|vs f characteristics, plotted with respect to L_{C3}.

The RF characteristics of the baseline GFET-2 in electron regime along with that of the proposed GFET having a C3 length of 245 nm are shown in Figure 3.4.32 (a). From Figure 3.4.32 (a), we see that the f_T of the baseline reported GFET and proposed GFET with 245nm capacitive extension are 20.05 GHz and 24.4 GHz respectively. Later the C3 length was gradually increase up to 550 nm as shown in Figure 3.4.32 (b). Due to the increment of C3 length, the f_T gradually increased and eventually reached a value of 25.9 GHz. As before, further increment of C3 length was studied and L_{C3}=550 nm was found to be the optimum extension.

In addition to the C3 extension over the access region, we also simulated a GFET with the source to drain distance same as that of the baseline, but with a longer gate. The new length of gate was equal to old gate length plus 2L_{C3}, L_{g-new}=L_{g-old}+2L_{C3}. From our simulation, we found that this device does not show any improvement of f_T, rather the f_T deteriorates compared to the baseline GFET. The reason behind this deterioration is the increment of transit delay. Though the C3 is capacitively coupled to the channel as like as the gate contact, the switching of the device takes

place in gate, not in C3s. The increment of the gate length increased the transit delay, whereas the equal C3 extension length reduced the parasitic delay.

3.4.2 Fabrication/Integration of GFETs

The proposed GFET with two additional contacts was fabricated jointly in a class 100 clean room of The Advanced Materials Engineering Research Institute (AMERI) at Florida International University and Nanoscale Research Facility (NRF) at University of Florida. The microfabrication involved processes including e-beam lithography, photolithography, e-beam evaporation, atomic layer deposition, and reactive ion etching. In conventional GFET fabrication process, the first step is transfer of Graphene on a suitable substrate, followed by patterning device mesa and source/drain contacts. The pattering of Graphene mesa as well as the patterning of source/drain contacts involve lithography, requiring the Graphene to be exposed to resists and developer several times. It is well known that Graphene is very much prone to contamination from resists and solvents, and the more it is exposed to contamination, the more the key feature of Graphene—mobility, degrades. Rather than following the conventional sequence of GFET fabrication steps starting with Graphene transfer and mesa etch, and ending with gate patterning, here we started the process by firstly pattering gate-FCE on the substrate, then oxide deposition and patterning, followed by source/drain patterning, and finally Graphene transfer followed by mesa etch. As a result, starting from the Graphene transfer ending with mesa etch, Graphene was never exposed to resists and developers, and prevented from the consequential contamination.

Lithography: Lithography is the process of transferring geometric pattern on the surface of a substrate wafer. The geometric pattern is transferred on a layer of resist which is coated on top of the wafer or a chip. When the coated resist is exposed to ultraviolet light (photolithography) or electron beam (e-beam lithography), it changes it physical properties in such a way that the exposed (positive resist) or unexposed (negative resist) part of the resist dissolves in the developed during the development process. The exposure of resist can be done in 2 ways: selectively obstructing light by using a mask, or direct writing where the writing head exposes the resist according to the design file. The lithography process includes the following steps:

Substrate Preparation: The basic intension behind surface preparation is to improve the adhesion of resist on the wafer/chip surface. The first step of surface preparation—surface cleaning, is done to remove organic and inorganic contaminants. Widely used solvents for surface cleaning are Acetone, Isopropyl Alcohol, and Methanol. After cleaning with solvents, it is washed with deionized water and baked at more than 100 °C for a few minutes to dehydrate. If the surface is hydrophilic, adhesion promoters such as hexamethyl disilizane (HMDS) is used to improve adhesion.

Resist Spin Coat: Resist is a material which is sensitive to radiation, UV for photolithography and e-beam for e-beam lithography. For photolithography, the resist that is used is sensitive to ultra violet light and is called photoresist. On the other hand, e-beam resist is sensitive to electron beam and used in electron beam lithography. In general, it contains inactive resin, solvent, and photoactive compound. When a resist polymer and electromagnetic radiation interact, two different types of chemical reactions can take place: (1) cross-linking (2) chain scission. The second one is also referred as fragmentation. In case of negative resists, cross-linking takes place,

whereas, chain scission takes place with positive resist. In cross-linking, after interaction with incoming radiation, the atoms in adjacent chains of the get displaced and the carbon atoms bond directly, resulting in a material not dissolvable in developer. On the other hand, radiation disrupts the polymer chains of positive resists, breaking them up to smaller pieces, and makes a material, very fast dissolvable to developer. The spin coater tool consists of a spinner chuck which holds wafer by vacuum and its spin speed (RPM), ramp, and spinning time can be set by user.

Baking: After coating the substrate with resist, the coated resist film contains remaining solvent concentration, and is baked on hot plate before exposure. The baking reduces the quantity of remaining solvent content to avoid mask contamination and sticking to the mask, prevent popping or foaming of the resist by N_2 created during exposure, improve resist adhesion to the substrate, minimize dark erosion during development, prevent dissolving one resist layer by a following multiple coating, and prevent bubbling during subsequent thermal processes (coating, dry etching). Baking can be divided in to two types: soft baking and hard baking. Immediately after resist coating, soft baking is done. On the other hand, had baking is the last step of lithography, done after exposure and development, in order to harden the photoresist and improve adhesion to the wafer surface.

E-beam Direct Writing: Once the substrate is coated with e-beam resist, direct e-beam writing is performed. Patterning techniques other that UV lithography including electron beam lithography and x-ray lithography are developed due to two driving forces. They are: higher resolution (smaller feature size) and cost. The maximum achievable resolution of a UV lithography system is limited with the wavelength of the beam. Conventional photolithography systems, which rely on UV light, can therefore achieve a minimum "diffraction-limited" feature size of several hundreds of nanometers and can be improved using advanced resolution enhancement techniques (RET). However, RET for photolithography increases cost and cycle time of masks along with increment of complexity for technology nodes. An electron's velocity and kinetic energy are related by the following equation:

$$E_{kin} = \frac{1}{2}mv^2$$
(3.4.30)

And the de Broglie wavelength for electrons with kinetic energy E_{kin} can be expressed as:

$$\lambda = \frac{h}{\sqrt{2mE_{kin}}} = \frac{1.23}{\sqrt{E_{kin}}}[nm]$$
(3.4.31)

It states that an electron accelerated to an energy of 10 keV would have a wavelength, $\lambda=0.12$ Å. This clearly shows that e-beam lithography has a huge advantage over current optical lithography systems, which are limited by their wavelength.

Modern sophisticated electron beam lithography (EBL) systems have the same fundamental parts in common including electron sources, electron lenses, beam deflector, aperture, beam blanker, stigmator, and stage. EBL patterning is performed in a high vacuum chamber. The sample is mounted on a wafer holder consisting of a set of test standards for calibration, focusing, and position. Calibration subroutines can be performed before the actual writing or during the writing. The stage is moved by piezoelectric motors and the position is controlled by laser interferometry

system. The use of laser interferometry system ensures to achieve nanometer-scale precision. To isolate mechanical vibration from the system, the stage is also placed on a vibration isolation system. In some of the systems, there is an additional charge coupled device camera inside the chamber to assess the control of sample positioning.

Photo Mask Writing: Photo mask consists of a glass, one side covered with chrome, and the chrome is covered with a photo resist. The pattern information, to be transferred on a wafer or chip, is created in a drawing package and generally stored in a database. The design file is then reformatted and transferred to a direct writing tool, which is generally named as Mask Maker. According to the drawing file, the mask maker exposes selective part of the photoresist on mask. The imaged pattern on the mask is then developed to form a template over the opaque chrome and put in chrome etchant to etch away chrome where the resist is clear. Once the chrome is etched away, the remaining photoresist is removed, cleaned and stored for later use, in a mask aligner tool.

Mask Alignment and exposure: In a multi-layer device fabrication/integration process, the first layer does not require any alignment, but the subsequent layers require to be aligned to the preceding layer. To aid the alignment process, each layer is accompanied by some features which help to align the mask for the next layer. These features are called alignment marks and these marks are transferred on the wafer in such a way they can be easily seen through a microscope of the mask aligner tool on the surface of the wafer and the photomask. The alignment marks are generally etched into the wafer after a previous photolithography step and it is required of the lithography to know what marks on the wafer are supposed to line up with what marks on the mask - which can get complicated after several masking steps. The mask alignment procedure starts with loading of the mask and the wafer in the aligner tool. The wafer vacuum stage on which the wafer is placed can be moved in x-dierection, y-direction, and can be rotated (θ). Using these knobs, the wafer is aligned to the fixed mask using a microscope. Once the alignment is done, the wafer is brought to contact with mask. Following the mask alignment and contact, the UV source power is measured, exposure time is calculated and the wafer is exposed.

Development: Once exposed, the wafer is removed from the stage and put into a solution named developer. The developer is a chemical that removes the exposed (unexposed) part of the positive (negative) photoresist coated on top of the wafer. The concentration of the developer and development duration need to be estimated during process development. After development, the wafer is rinsed with DI water and dried with N_2 for subsequent steps.

Descum: This procedure is used to remove residual photoresist from the arears where photoresist is removed by developer. The thickness of such residual photoresist film is generally less than 1000 Å, but its interference can very detrimental in the subsequent processing, especially if the pattern geometry is very small. A low power short time reactive ion etching is generally used to remove these residues.

Reactive Ion Etching: The reactive ion etching (RIE) uses chemically reactive plasma generated at the presence of RF power under a low pressure (10-100 mTorr) to consume the material on wafer, in addition to ionic bombardment. In the RIE system, the wafer is placed on a chuck which is grounded, and another electrode on top of the grounded chuck is connected to RF source. Generally the frequency of the RF source is 13.56 MHz. As the electrons are lighter compared to

ions, they move faster, collide very frequently and as a result, is removed of the plasma. The positively charged plasma forms a DC electric field. In addition to chemical reaction between the plasma and target material, the positive ions can be accelerated by applied electric field and can physically bombard the target as well. This process of physical bombardment can also assist the etching process. In contrast to wet etching, RIE can move the etchant in the direction of applied electric field and produce anisotropic profile.

E-beam Evaporation: The electron beam evaporation system is used to produce uniform high-purity thin films. It is used to evaporate refractory and dielectric materials, as well as the more common conductive and semiconductor materials. Electron beam heating is an efficient way to achieve high temperatures for uniform thin film, optical coating and vacuum metallurgic processes. The e-Gun is a self-accelerated electron beam device, held at a high negative potential, which is produced by the hot tungsten filament. The beam of electrons leaves the filament and then magnetically focused. The evaporant material is put in a crucible and the crucible is placed in a pocket where it is grounded and water cooled. The beam strikes the evaporant material with a set spot size and intensity. Using an electro-magnetic system, the electron beam can be swept over the evaporant material. The material deposition rate can be changed by tuning input power, charge size, charge shape, and the characteristics of the material to be evaporated. Material with low evaporation temperature and high thermal conductivity can be evaporated with highest evaporation rates. In this process, the evaporant are not contaminated because the focused electron beam strikes only the evaporant source material in the crucible. The e-Gun source generally operates in a high vacuum chamber and the magnitude of chamber pressure, which normally increases during evaporation, depends on the pumping capacity of the system and the cleanliness of the evaporant material.

Lift-off: Lift-off is a method of patterning deposited thin films which are difficult to pattern by dry etching. The pattern is transferred on the substrate using standard photolithographic process followed by descum. The thin film is blanket deposited on top of the whole substrate which covers the photoresist as well as the areas where photoresist has been removed to open windows. As a result, at the windows, the film is deposited on the substrate, whereas, in rest of the areas, it is deposited on photoresist. During lift-off, the thin film covered substrate is put in a solvent that removes the photoresist as well as the thin film deposited on top of photoresist, leaving behind the film deposited directly on substrate.

Graphene Transfer: CVD Graphene grown on Copper sheet is coated with PMMA and put floating on a suitable copper etchant without any disturbance while copper surface touching the solution. Once the copper is completely etched, it is washed with DI water multiple times without flipping, and eventually transferred on suitable substrate. After being transferred, the sample is put in a desiccant to remove water molecules and then put in a suitable solvent to remove the PMMA.

Fabrication of GFET: Process Details
A 300 nm SiO_2 on top of N-type Silicon was chosen as substrate of the device. The substrate was cleaned with acetone/IPA/methanol, rinsed with DI water, and dried with N_2 flow. The sample was then baked at 100 ºC for 3 minutes to remove solvent remnants. The fabrication process consists of a total of 6 different layers, and the layout design of these layers was done using Layout Editor.
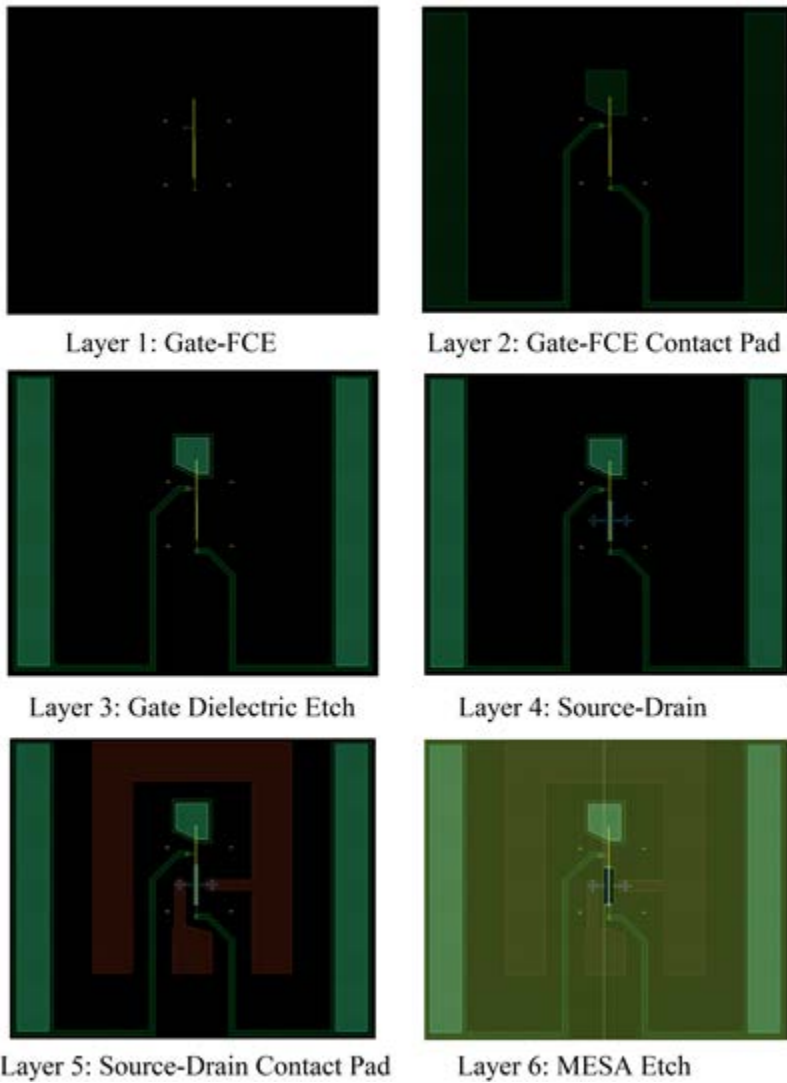
Figure 3.4.33: Layout design of 6 different layers.

The layout design of the 6 different layers is shown in Figure 3.4.33. 200 nm of 950 PMMA A4 was spin coated (200nm thick, static pour, at 500 RPM for 5s, then 4000 RPM for 45s) and oven baked at 185 ℃ for 30 minutes. The Gate-FCE layer with alignment marks were patterned using e-beam lithography. For e-beam writing, 15kV beam voltage was used at a dose of 18 0uC/Cm^2, with a step size of 25 nm, column aperture of 30 um, and a write field of 200 um. It was developed in a solution of MIBK: IPA=1: 3 for 30 seconds at 4 ℃ using a chiller plate. 10-nm Ti/40-nm Au was evaporated using e-beam evaporator at a chamber pressure of 2×10^{-7} mTorr and lifted-off in acetone, in a standard sonic bath, by sonicating for 1 minute. Figure 3.4.34 shows the optical image of gate-FCE along with the alignment marks after lift-off.
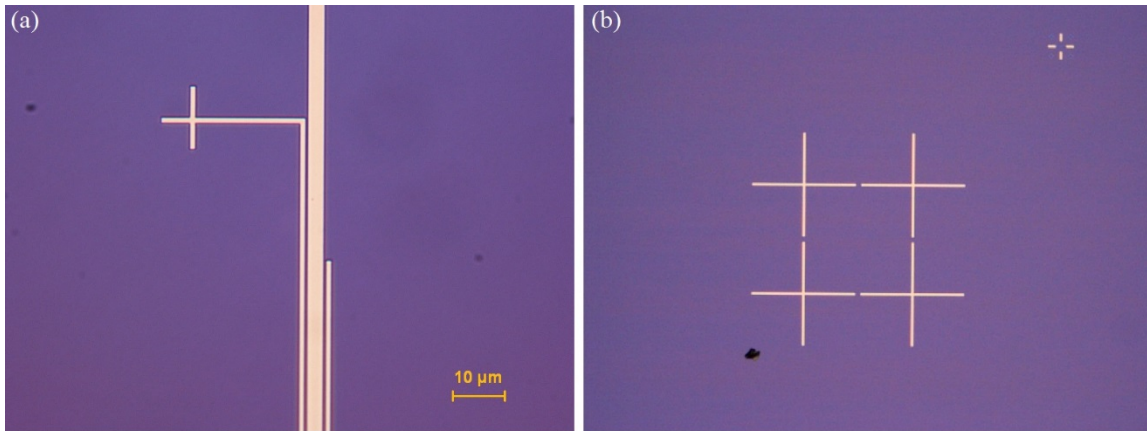
**Figure 3.4.34:** Optical microscope image of (a) Gate-FCE layer after metallization and lift-off (b) Alignment marks for mask alignment after metallization and lift-off.

The next layer was the pads. The substrate with Gate-FCE layer patterned and metalized is then coated with 600 nm LOR 3B (Step 1: 500 RPM/100 Ramp, 5 s; Step 2: 1000 RPM/500 Ramp, 60 s) on top of 600 nm S1805 photoresist (Step 1: 1500 RPM/300 Ramp, 5 s; Step 2: 3000 RPM/500 Ramp). The LOR 3B lift off resist and S1805 photoresist were cured on a hotplate at 180 °C (10 minutes) and 115 °C (3 minutes), respectively. Photo mask for the Gate-FCE pad layer was written using mask maker and aligned on the patterned substrate using a mask aligner. After exposing with UV, it was developed in developer MF-26A for 15 minutes, rinsed with DI, dried with N_2, and a descum was done by oxygen plasma etching for 15 seconds. 10-nm Ti/500-nm Ni was evaporated for pad layer metallization and lifted-off in Remover-PG without sonication. The optical microscope image of the sample after lift-off is shown in Figure 3.4.35 (a).
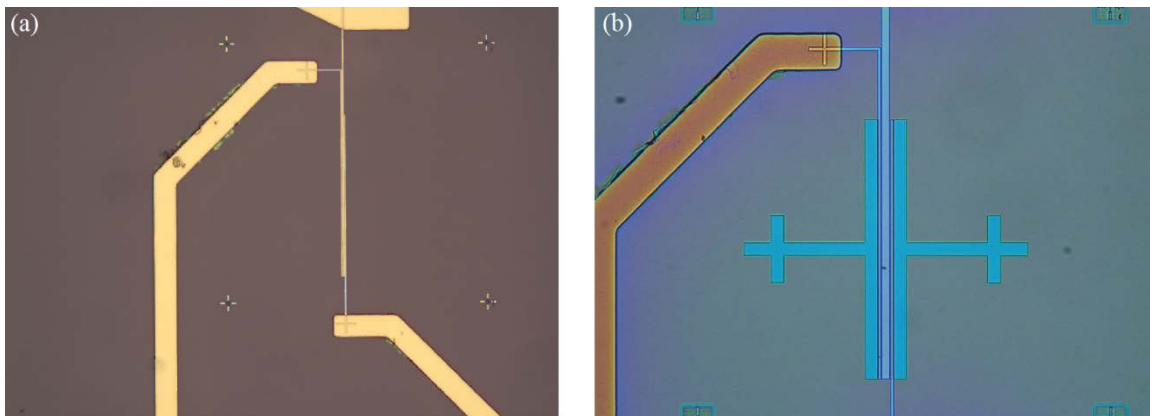
Figure 3.4.35: Optical microscope image of (a) Gate-FCE pad layer after metallization and lift-off, (b) Source/drain layer after metallization and lift-off.

Following the Gate-FCE layer and pad layer formation, 20 nm HfO_2 was deposited by ALD, as gate dielectric. Then it went through the same photolithographic process with mask to open windows for the pads. The 20 nm dielectric above the pads was etched by reactive ion etching (Chlorine + Argon) through the windows. For the Source-Drain patterning, the same e-beam

lithographic process was used and 10-nmTi/50-nm Au was evaporated, followed by the same lift-off process in sonic bath. The image of the chip after source/drain metallization and lift-off is shown in Figure 3.4.35 (b). Source-Drain pad layer was patterned by the photolithographic process used for Gate-FCE pad layer, followed by a 10-nm Ti/500-nm Au evaporation, and lift-off.
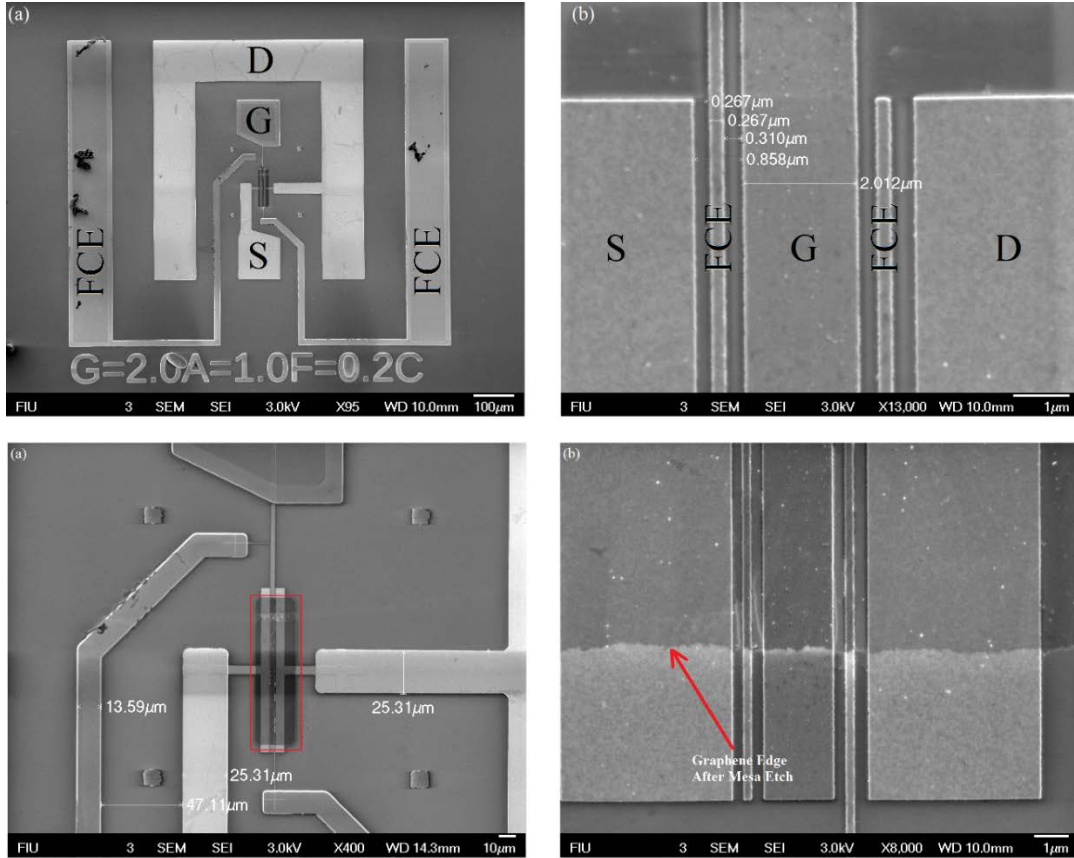
Figure 3.4.36: (a) SEM image of the GFET with source, drain, gate, and FCEs marked. The letters S, D, and G stand for source, drain, and gate respectively. (b) High magnification image of the device with embedded scale showing FCE length, gate length, and access region length, (c) The Graphene channel after mesa etch, marked with red rectangle, (d) a closer view of the Graphene channel edge.

Single layer CVD Graphene grown on Copper sheet was coated with PMMA using a regular spin coater and was put floating on $FeCl_3$ solution for 8 hours without any disturbance while copper surface touching the solution. Once the copper was completely etched, it was washed with DI water multiple times without flipping, and eventually was transferred on the patterned substrate. After transfer, the sample was put in a desiccant for 8 hours. Graphene covered with PMMA was then coated with S1805 photoresist and went through the same photolithographic process with mesa mask, to open windows for mesa etch, through which oxygen plasma etching was used to etch PMMA and Graphene. Figure 3.4.36 shown the SEM image of the GFET after fabrication at low and high magnification at different regions. After mesa etch, the sample was put in acetone at 50 °C for 15 minutes to remove PMMA over the Graphene channel. The simplified process flow is shown in Figure 3.4.37.
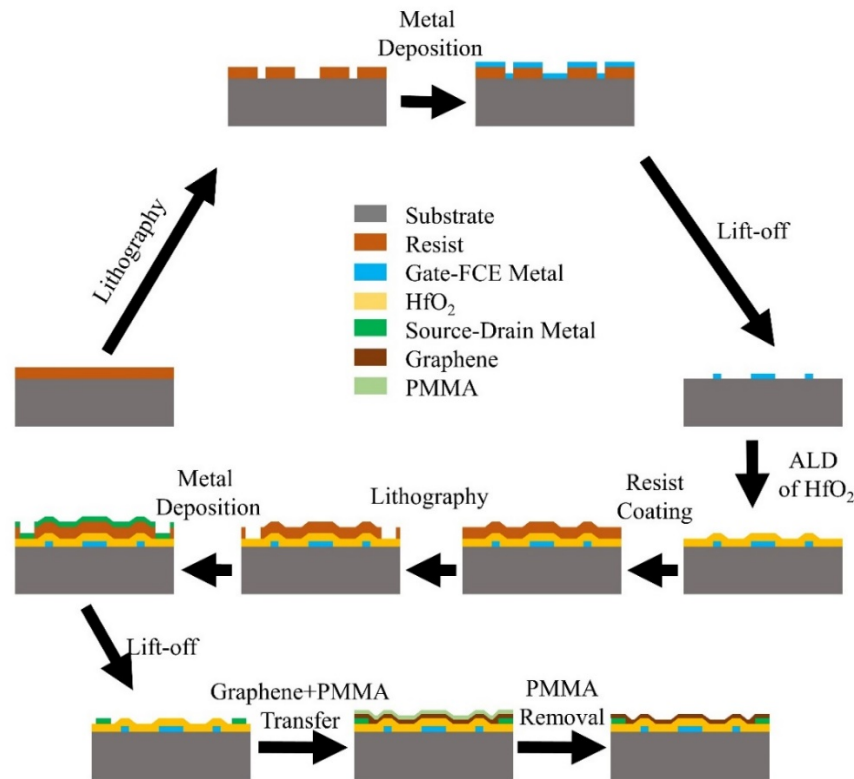
Figure 3.4.37: Simplified process flow of GFET fabrication/integration

3.4.3 Characterization of GFETs with Field Controlling Electrodes

The Graphene channel was characterized by Raman spectroscopy. Figure 3.4.38 shows the Raman spectrum of the Graphene taken using a 532 nm laser with a spot size of 1 µm^2. The 2D/G ratio (0.93) of the Raman spectrum confirms the presence of single layer Graphene.
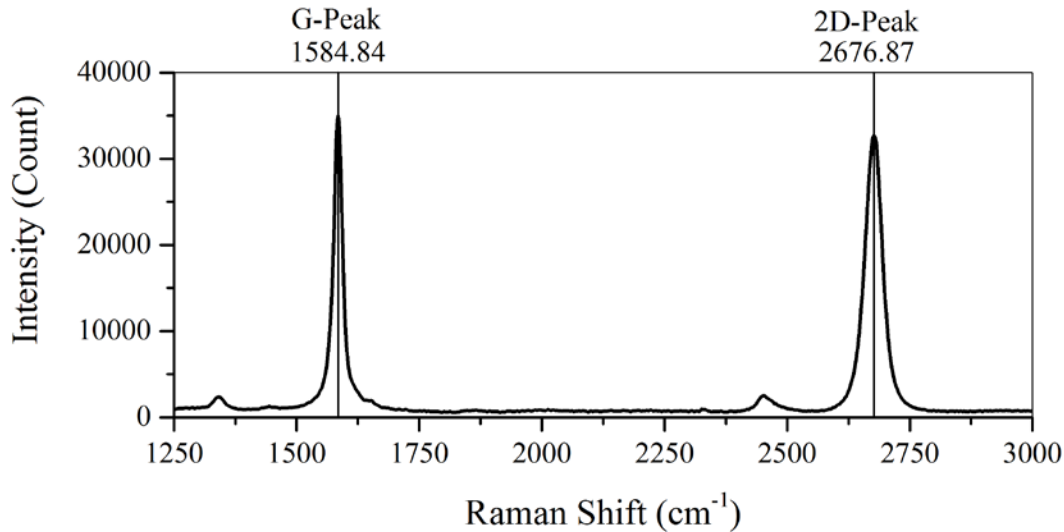
Figure 3.4.38: Raman spectrum of single layer Graphene forming FET channel

The DC characteristics of the fabricated device was measured using a HP 4156 A semiconductor parameter analyzer integrated with a probe station. Figure 3.4.39 (a) shows the drain voltage vs. drain current characteristics with different FCE biases starting from 0 V to -6.0 V, applied on both of the FCEs, with a step size of 2.0 V. In Figure 3.4.39 (b), the gate voltage vs drain current characteristics is plotted for different FCE biases, as well. From the transfer characteristics, it is evident that the Dirac point was not reached up to +8.0 volts. It implies that the Graphene had unintentional p-type doping during growth/transfer.

From the I_d-V_d characteristics, as well as the I_d-V_g characteristics, it is evident that the additional DC bias applied at both of the FCEs result in decrement of access resistance, which eventually increases Drain current.
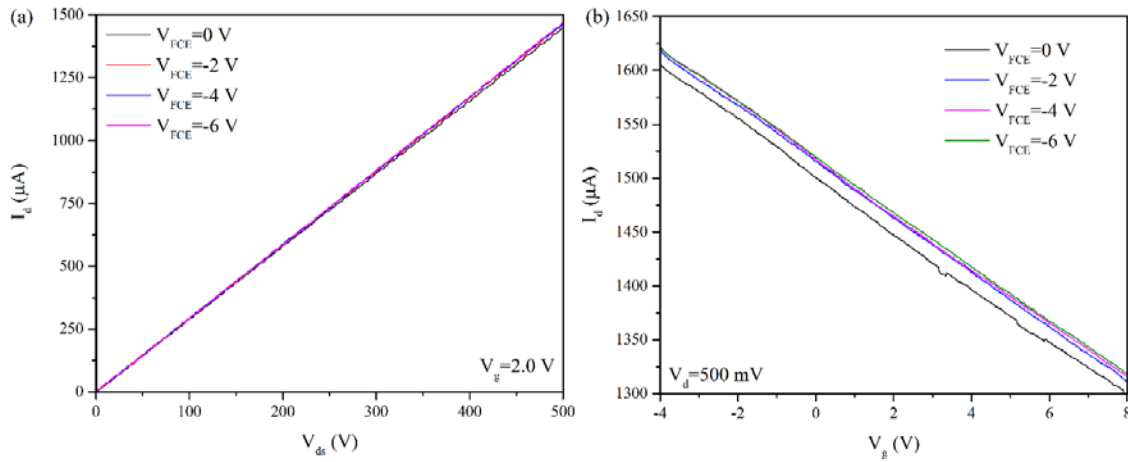
Figure 3.4.39: (a) The Id-Vd characteristics of GFET at different V_{FCE} (b) The Id-Vg characteristics of GFET at different V_{FCE}.

The gate leakage current of the device is plotted in logarithmic scale and shown in Figure 3.4.40. The leakage current was at the order of a pA.
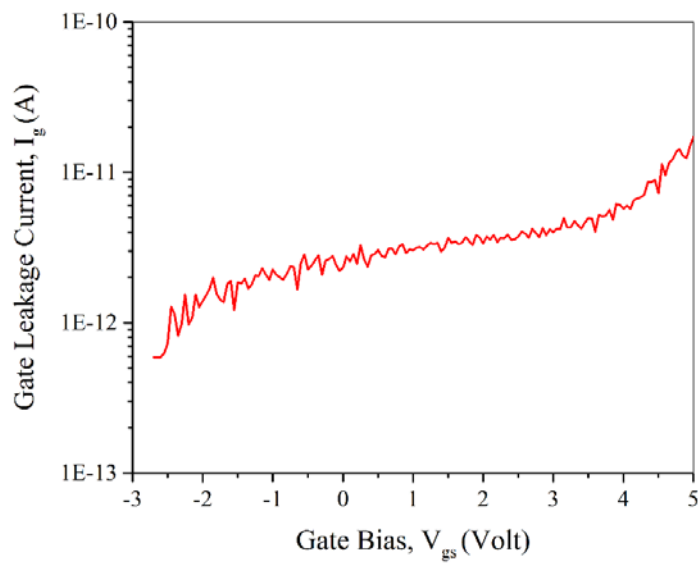
Figure 3.4.40: Gate leakage current

In addition to gate leakage current, the FCE leakage current was measured as well. The FCE leakage current was at the order of pA as well, as shown in Figure 3.4.41. Low gate leakage current as well as low FCE leakage current is important for good RF performance.
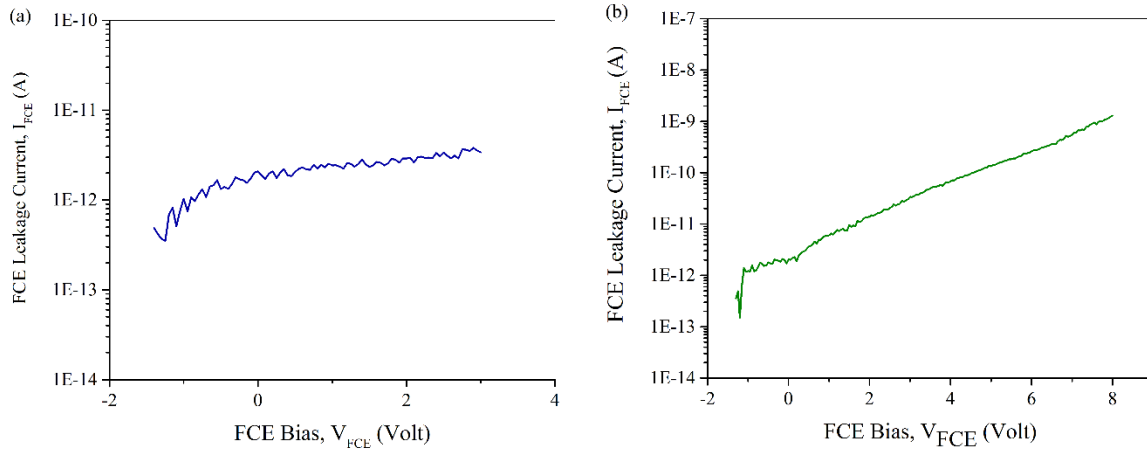

Figure 3.4.41: Leakage current of (a) FCE-1 and (b) FCE-2

The RF characteristics of the GFET was measured using a vector network analyzer HP 8510 C integrated with a probe station from J micro Technology with two coplanar waveguide probes (50A-GSG-200-DP) from GGB Industries. The schematic of the setup is shown in Figure 3.4.42.
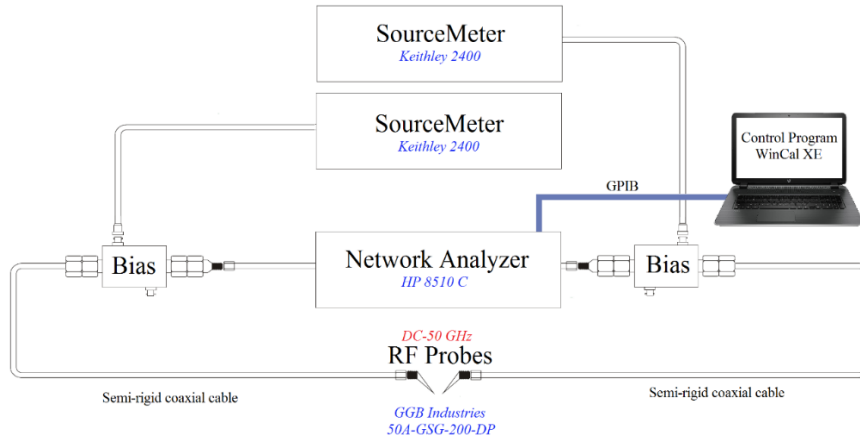
Figure 3.4.42: Schematic of the S-parameter measurement setup

Two 24" long low loss phase stable semi-rigid coaxial cable with one 2.4mm Female connector and one 2.4mm Male connector were used to connect the probes. DC bias was applied using two bias tees PE1610 from Pasternack and two Keithley 2400 SourceMeters. Standard Short-Open-Load-Thru (SOLT) calibration was performed using a clabration substrate CS-5 from GGB Industries, before measuring the 2-port S-Parameters. The network analyzer was controlled by a comprehensive and intuitive on-wafer RF measurement calibration software named WinCal XE from Cascade Microtech, to achieve accurate and repeatable S-parameter measurement. The WinCalXE features include exclusive 1-, 2-, 3-, and 4-port calibration algorithms, immediate and live data measurement and viewing, LRRM, LRM+, SOLT-LRRM hybrid and NIST-style multi-line TRL calibrations, as well as an Error Set Management capability for data comparison and augmentation. A picture of the setup is shown in Figure 3.4.43.

67
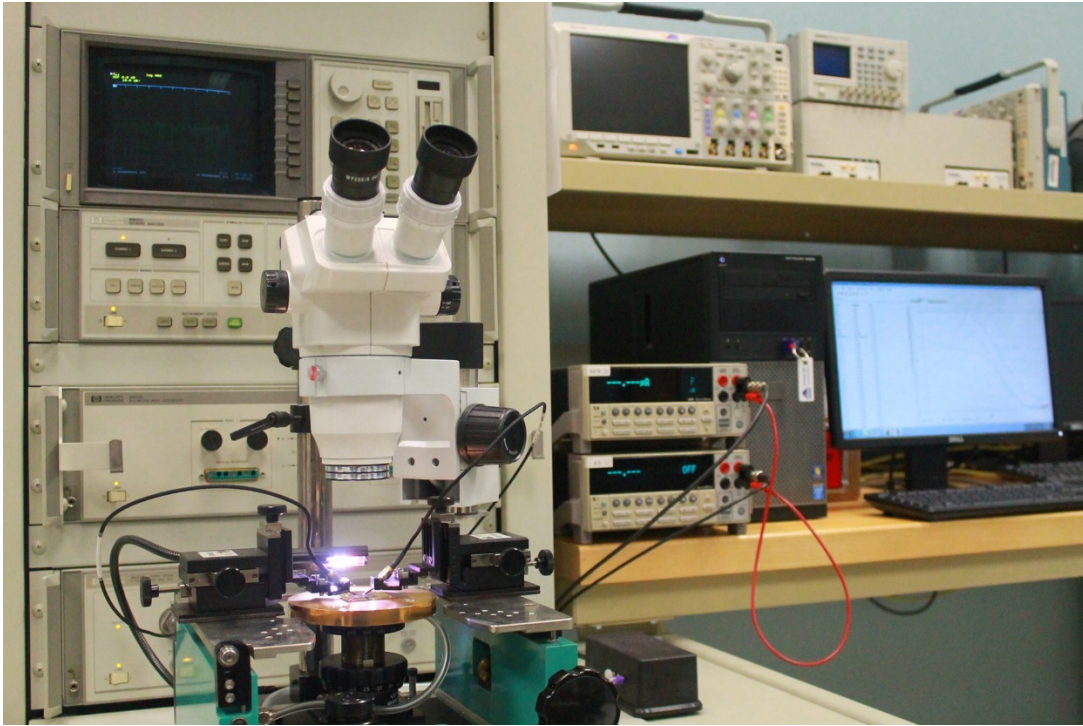
Figure 3.4.43: A picture of RF measurement Setup

The two port S-parameter of the device was measure, corrected by the calibration file, and converted to h21 parameter using the following equation:

$$h_{21} = \frac{-2S_{21}(R_{01}R_{02})^{1/2}}{(1-S_{11})(Z_{02}^* + S_{22}Z_{02}) + S_{12}S_{21}Z_{02}}$$

(3.4.32)

where Z_{01} is source impedance and Z_{02} is load impedance. The current gain, |h21| is plotted with respect to frequency in Figure 3.4.44 for two different devices: conventional 3 terminal GFET and the same geometry GFET with proposed additional contacts (FCEs). The DC biasing condition at source, drain and gate were same for both of the devices whereas the proposed device had both of its FCEs biased at -3.0 V. From Figure 3.4.44, it is evident that -3.0 V applied at both of the FCEs increases the current gain cut-off frequency from 1.10 GHz to 1.22 GHz.
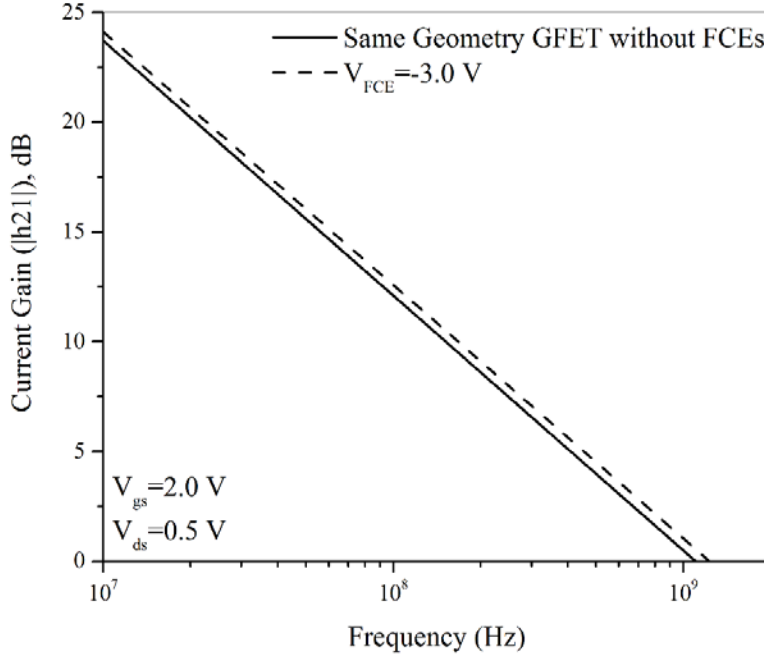
Figure 3.4.44: Current gain of a conventional 3 terminal GFET along with that of a same geometry proposed GFET plotted with respect to frequency for comparison.

In conclusion, we proposed, extensively analyzed, fabricated, and characterized a Graphene FET with two capacitively coupled field-controlling electrodes at the access regions of the device. It is observed that the biased FCEs could control sheet carrier concentration at the ungated regions, and thus resulted in a reduction of the access resistance and improvement of the RF performance of GFETs. The increment of current gain cut-off frequency, f_T was 10.9% compared to that of same geometry GFET without FCEs. The proposed GFET with improved RF characteristics can be used for high frequency applications.

3.5 Graphene Plasmonic Devices and Metasurfaces for THz
3.5.1 Analysis of Graphene-based periodic gate FET structures for THz applications

We performed theoretical investigation of graphene based FET structures for resonant absorption of THz radiation by the plasmons excited in the high sheet concentration and high carrier mobility active layers. Our studies demonstrate that the proposed periodic gate FET structures of Graphene can resonantly absorb THz radiation up to 5th harmonic at room temperature. Moreover, these structures have the advantage of tunability by the modulation of sheet carrier concentration in the channel.

The structures investigated in this study consist of graphene layers on sapphire substrates (see the inset in Fig. 3.5.1). Titanium grating gates are placed on 17 nm thick SiO_2 layer deposited on graphene. Different gate period, L, and gate finger length, W, combinations were studied. A commercial simulation package of finite-difference time-domain (FDTD) method with a 3D Maxwell equation solver and a custom code for data analysis were used to calculate absorption

69

and transmission spectra of the structures. The simulations were carried out using periodic boundary conditions for the grating gate arrays. Furthermore, real experimental data for dispersion relations and different loss mechanisms for materials were used in the simulation. The mesh size was sufficiently small to match experimental data for structures with small features. We validated our simulation method by comparing the numerical results by the experimental results reported in the literature for AlGaN/GaN grating gate devices and graphene nanoribbon metamaterial structures.

A short channel with high sheet carrier concentration acts as a resonant cavity for the plasma waves with the fundamental frequency of ω_0 and its harmonics. An incoming electromagnetic radiation excites plasma waves in such a channel. When $\omega_0\tau \gg 1$ (τ is the momentum relaxation time) the resonant condition is satisfied. The electron energy dispersion in undoped grapheme is linear $E=\nabla V_F.k$ with k being the electron momentum and V_F being the 2D Fermi velocity, which is a constant for graphene ($V_F =10^8$ cm/ s). The linear electron energy spectrum implies zero effective electron mass in graphene. The electron "inertia" in massless graphene is described by a fictitious "relativistic" effective mass $m_F=E_F/V_F^2$, where E_F is the Fermi energy. Electron relaxation rate in graphene with electron mobility μ can be estimated as $1/\tau = e/\mu m_F$. Therefore, $\omega_0\tau \gg 1$ is satisfied for frequencies above 2 THz even for low mobility graphene with $\mu = 1600$ cm^2/Vs. Plasmon dispersion in a gated graphene can be formally written in the same form as in a conventional semiconductor structure with substituting the effective electron mass by the "relativistic" effective mass m_F resulting in

$$\omega = q^4 \sqrt{N_s \frac{V_F^2 e^4 d^2}{2\pi \hbar^2 \varepsilon^2}} \qquad (3.5.1)$$

where N_s is the sheet carrier concentration, d is the distance between the graphene channel and the gate metal, ε is the permittivity, q is the plasmon wavevector, which is determined by the grating gate period L, $q=2\pi//L$ (n = 1,2,3…).
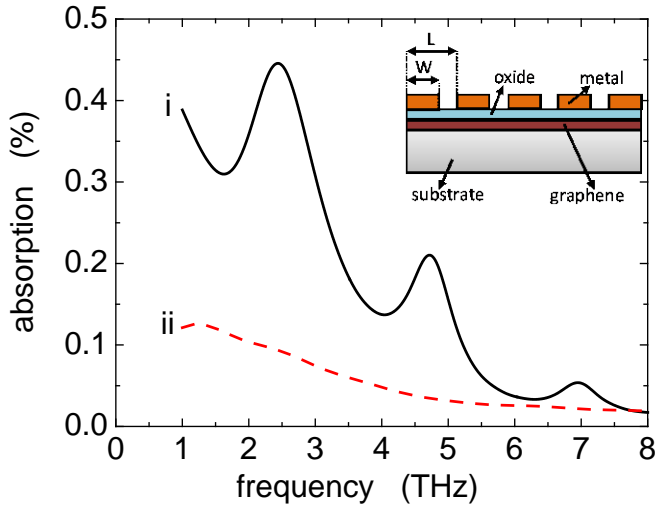
**Figure 3.5.1:** Room temperature absorption spectra of AlGaN/GaN and Graphene grating gate FET structures with L=1.5µm W=1.15 µm, N_S=7.5×10^{12} cm^{-2}. The inset shows the cross section of the studied structures. (i) Graphene, (ii) AlGaN/GaN

Room temperature operation is a crucial aspect for the practicality of the THz devices for many practical applications like medical imaging, security and sensing. In Fig. 3.5.1 we compare the room temperature absorption spectra of Graphene and AlGaN/GaN grating gate devices with the same geometrical parameters. The graphene devices present a well pronounced resonant absorption peaks corresponding to the fundamental mode and first two harmonics in the $1 - 8$ THz range. The resonant frequencies are in agreement with the calculated values using the eqn. (3.5.1).

The modulation depth in the absorption spectrum of the periodic gated FET structures is also controlled by the carrier scattering rate in the channel. The lower scattering rate in graphene compared to GaN/AlGaN heterostructure devices allows clear absorption peaks with large modulation depth. Effect of the scattering rate in graphene is presented in Fig. 3.5.2a. For lower mobilities (curve i and ii) contribution of Drude absorption at the background is visible. As the mobility increases, modulation depth increases as especially at higher frequency modes.
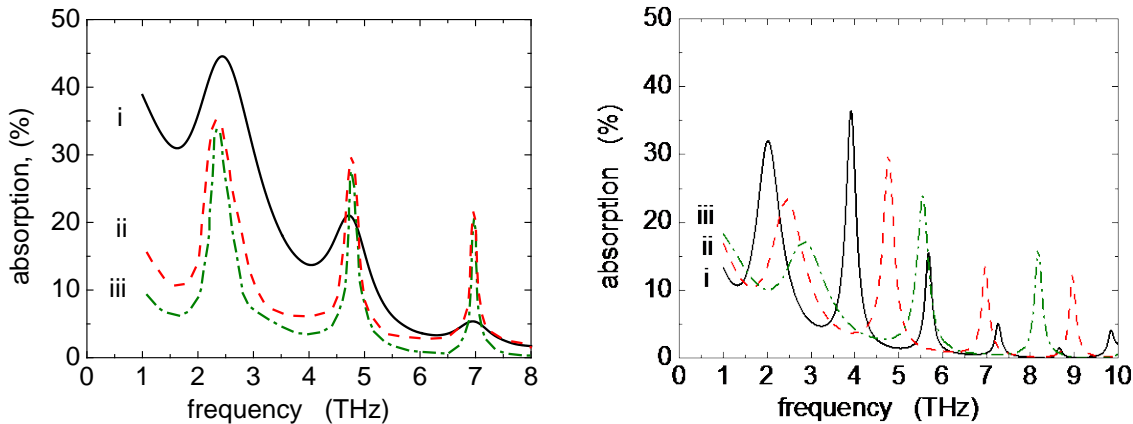
Figure 3.5.2: (a) Absorption spectra of graphene with different mobilities. L=1.5µm W=1.15 µm, N_S=7.5×10^{12} cm^{-2}. (i) µ = 3000 cm^2/V.s (ii) µ = 15000 cm^2/V.s (iii) µ = 40000 cm^2/V.s **(b)** Absorption spectra of graphene grating gate FET structure with different carrier concentrations. L=1.5µm W=1.15µm, µ=15000 cm^2/Vs. (i) Ns = 3.6×10^{12} cm^{-2} (ii) Ns = 8.3×10^{12} cm^{-2} (iii) Ns = 1.5×10^{13} cm^{-2}

An important advantage of the grating gate devices is tunability of the resonant absorption frequencies though controlling the charge concentration by the applied gate voltage. Fig. 3.5.2b clearly shows the shift of the resonant frequencies by the charge carrier concentration as expected from the eqn.(3.5.1). It should be noted that the plasmon frequency in graphene exhibits different dependence on the gate voltage ($\sim N_s^{1/4}$) as compared with gated plasmons in conventional semiconductor structures ($\sim N_s^{1/2}$).

3.5.2 Deep Sub-wavelength Multimode Tunable In-Plane Plasmonic Lenses Operating at Terahertz Frequencies

Terahertz technologies utilize electromagnetic radiation in the frequency range between 300 GHz and 10 THz. Potential applications for terahertz technology in biology, chemistry, medicine, astronomy and security are wide ranging. THz wavelengths have several properties that could promote their use as sensing and imaging tool. There is no ionization hazard for biological tissue and Rayleigh scattering of electromagnetic radiation is many orders of magnitude less for THz

wavelengths than for the neighboring infrared and optical regions of the spectrum. THz radiation can also penetrate non-metallic materials such as fabric, leather, plastic which makes it useful in security screening for concealed weapons. The THz frequencies correspond to energy levels of molecular rotations and vibrations of DNA and proteins as well as explosives, and these may provide characteristic fingerprints to differentiate biological tissues in a region of the spectrum not previously explored for medical use or detect and identify trace amount of explosives. THz wavelengths are particularly sensitive to water and exhibit absorption peaks which make the technique very sensitive to hydration state and can indicate tissue condition. THz radiation has also been used in the characterization of semiconductor materials and in testing and failure analysis of VLSI circuits.

Plasma oscillations in various types of field effect transistors (FETs) are used for THz detection, mixing and generation. Plasmonic THz detectors have the advantage of continuous tunability over the conventional detectors such as bolometers and pyroelectric detectors. However, detection of THz radiation by such devices can be polarization dependent because only TM polarized incident THz radiation can excite the plasmons as a result of Maxwell's equations and therefore their response to

Figure 3.5.3: (a) THz plasmonic concentrators with concentric circular gratings. (b) The cross section of the AlGaN/GaN devices passing from the center of the circular grating structure.(c) Cross section of the graphene devices.

most THz sources such as blackbody emitters which radiate unpolarized radiation is diminished. On the other hand, responsivity of FET based detectors is also limited by the size of their active region which is typically much smaller than the wavelength of THz radiation. Meanwhile, Graphene with remarkably high electron mobility at room temperature, with reported values in excess of 15,000 cm^2/V.s has strong potential for THz plasmonic devices. Recently, the high mobility properties of Graphene at room temperature was exploited to demonstrate graphene plasmonic THz metamaterials and FETs for THz detection.

Metal structures have been proposed to focus plasmons in visible and near infrared region. Other plasmonic methods have been used to focus THz radiation including tapered metal-plasmon tip which allowed λ/250 compression. However, there has been no reported study on focusing of plasmons in-plane deep sub-wavelength regime. In this paper, we propose a new type of plasmonic devices which has the capability of focusing the incident THz radiation into deep sub-wavelength volume independent of its polarization. Moreover, the resonant modes of the focused plasmons can be tuned by the applied voltage on the metallic gratings.

The proposed in-plane THz plasmonic concentrator devices consist of periodic concentric metallic rings placed on AlGaN/GaN heterojunction and graphene active layer as presented in Fig. 3.5.3. The abrupt junction of the GaN/AlGaN interface plane causes the creation of 2 dimensional electron gas (2DEG) at the interface with large sheet carrier concentration and high mobility which would serve as a resonance cavity for the plasmons. Plasmons in such structures follow the gated 2DEG plasmon dispersion. Graphene with its potentially very high mobility also can act as a plasmonic cavity. The periodicity in the radial direction compensates the momentum for excitation
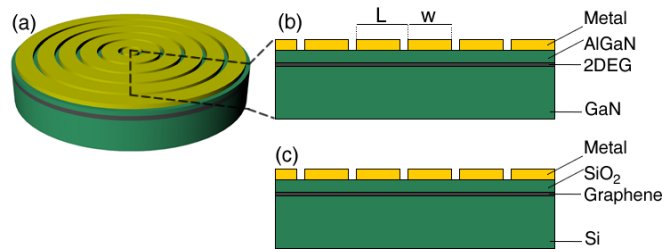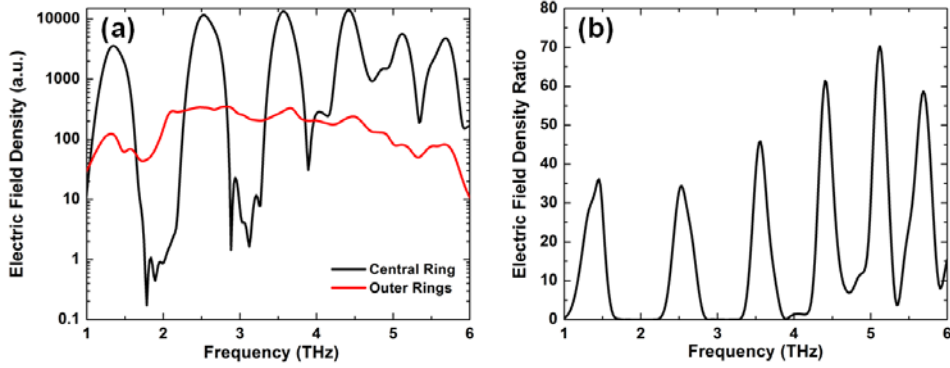
Figure 3.5.4: (a) Electric field density under the central ring and under the outer rings. The total electric field under the central and outer rings are divided by the total are of the rings. (b) Electric field density ratio under the central ring to the electric field density under the outer rings. The ratio gives the strength of the electric field confinement at the central ring. L=1.5 μm, w= 1.3μm, N=7.5×10^{12} cm^{-2}.

of the plasmons in between the metal and the active layers. The outer edge of the outer most ring is assumed to be mesa etched which results in isolated cylindrical active region. This etched interface causes the reflection of the plasmons.

Plasmonic absorption of THz radiation is based on the excitation of plasma oscillations in the 2DEG channels by the incoming radiation. A short channel with high sheet carrier concentration acts as a resonant cavity for the plasma waves with the fundamental frequency of ω_0 and its harmonics. An incoming electromagnetic radiation excites plasma waves in such a channel. When $\omega_0 \tau \gg 1$ (τ is the momentum relaxation time) the resonant condition is satisfied. Such a cavity supports two different types of plasma oscillations. The first is the plasma oscillations in the gated region of the 2DEG channel. If an infinite perfectly conductive plane is located at distance d from the infinite 2DEG at a semiconductor heterojunction (e.g. AlGaN/GaN), and the conducting plane is close enough to 2D electron sheet (i.e. kd<<1) then the dispersion relation is given by

$$\omega_p = k \sqrt[4]{N \frac{V_F^2 e^4 d^2}{2\pi \hbar^2 \varepsilon_0^2}} \tag{3.5.2}$$

It should be noted that the plasmon frequency in graphene exhibits different dependence on the gate voltage ($\sim N^{1/4}$) as compared with gated plasmons in conventional semiconductor structures ($\sim N^{1/2}$). Moreover, potentially very large electron mobility in graphene would allow resonant condition to be satisfied at lower frequencies while providing higher Q factors at higher frequencies.

Room temperature operation is a crucial aspect for the practicality of the THz devices for many practical applications like medical imaging, security and sensing. Plasma resonances in a grating gate device can be best excited when the radiative damping γ_{rad} is equal to the dissipative damping γ_{dis} caused by the carrier scattering. In this case the maximum absorbance is given by $0.5(1 - \sqrt{R_0})$ where R_0 is the reflectivity when there is no resonant surface layer. Dissipative damping γ_{dis} of a plasmon mode increases with temperature. Therefore, matching condition of $\gamma_{rad} = \gamma_{dis}$ requires strong radiative broadening at room temperatures. Since the radiative broadening is directly
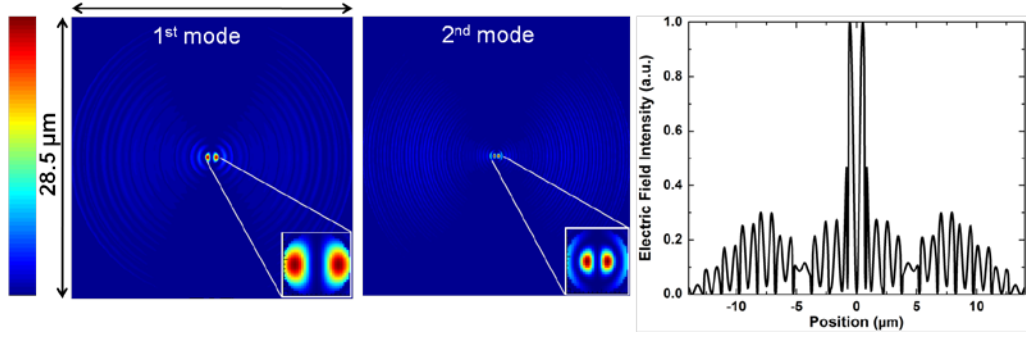
Figure 3.5.5: (a) Simulated electric field mode distribution for the fundamental mode in between the grating and 2DEG, (b) second mode, (c) Electric field intensity on the diameter parallel to the polarization of the incident THz radiation for the fundamental mode.

proportional to the conductivity of the channel, graphene layers are especially promising for room temperature resonant absorption of THz radiation. Radiative dampening is also directly proportional to the strength of coupling between the plasmon modes and the incident THz radiation. Strong electric near field induced in narrow spacings between the circular grating gate metals greatly enhances the coupling and hence the radiative dampening. Slit width (L - w) in the investigated devices was chosen to be about 15% of the metal ring width to achieve high resonant absorbance.

A commercial FDTD simulation tool Lumerical^{TM} is used to investigate the electromagnetic field profile of the plasmons and absorption spectrum of the plasmons at THz frequencies. The modes are excited with a broad band plane wave source perpendicular to the plane of the structure. A reflection and transmission monitor is placed to calculate the absorption spectrum of the device. An electric field profile monitor is placed in between the 2DEG and circular gratings to record the electric field profile of the plasmons. The 2DEG is defined as a plasma layer with specific plasma frequency and collision frequency extracted from the experimental results. The simulation is automatically stopped when the total electric field converges down to a small electric field that is orders of magnitude smaller than the initial electric field.

Electric Field Profile of the Plasmons

AlGaN/GaN heterostructures have simultaneous high mobility and high electron concentration compared to the other semiconductor materials which lead experimental demonstration of GaN-based THz plasmonic devices which could be used for validation of our simulation method. Moreover, GaN based material and device fabrication technologies have reached maturity. Therefore, we first investigated the plasmonic lens devices on AlGaN/GaN heterostructures (see Fig. 3.5.3). Later in this paper, graphene THz devices are investigated due to their potentially much larger mobility and sheet charge carrier concentration. Thickness of the AlGaN barrier layer was 28nm, and the sheet carrier concentration was taken as N=7.5×10^{12} cm^{-2}. A 60nm thick layer of gold was used as gate metal. To observe the resonant absorption clearly, rather high electron mobility of 10,000cm^2/V.s which could be attained at 77K was chosen. These values are close to the experimental ones reported in a recent study of linear grating gate devices. The period L was varied in range of 1.0 - 2.0 μm, whereas the lens gate length w was varied in the range of 0.5 -1.5 μm. The simulation results indicate that gated plasmons in the proposed devices are excited under all the circular gratings. Plasmons effectively propagate parallel to the radial vectors of the circles and interfere with each other forming a standing wave profile.

74
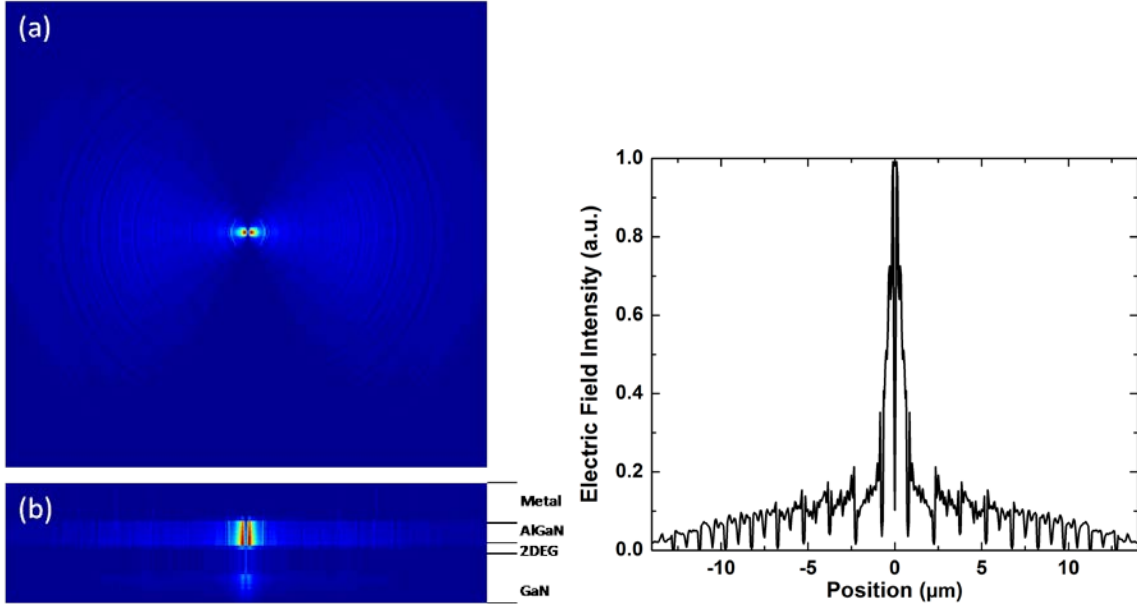
Figure 3.5.6: (a) Summation of modes from 1 to 5. (b) Electric field intensity on the diameter parallel to the polarization of the incident THz radiation for the total electric field summation from mode 1 to 5 five. (c) Electric field intensity summation from mode 1 to 5 five at the center of AlGaN layer on the diameter parallel to the polarization of the incident radiation.

The plasmonic field intensity is concentrated under the central ring and expanded at the outer rings. The plasmons are reflected back from the outer boundaries of the circular mesa and the process continues as they attenuate. When the quality factor is high enough, the plasmons excited at the outer rings can reach to the central ring before they attenuate and thereby contribute to the focusing.

Fig. 3.5.4(a) shows the areal electric field densies under the central ring and outer rings as a function of frequency. Areal electric field density is calculated by dividing the total electric field within a region to its total area. As expected, electric field density under the central ring presents clear peaks at the resonant frequencies which are in good agreement with Eq. (1). Moreover, at the plasmonic resonance frequencies, the electric field density under the central ring is much higher than that of the electric field density under the outer rings. The electric field intensity at the central point can be 6 orders of magnitude higher than that at the points on a line orthogonal to the polarization of the incident radiation. The ratio of the electric field density under the central ring to the outer rings gives the focusing ratio of the field. As the Fig. 3.5.4(b) shows the electric field under the central ring can be 70 times higher than the total electric field under all outer rings.

The electric field distribution in the entire structure for the fundamental mode is shown in Fig. 3.5.5 (a). Two electric field peak intensities are observed at the center of the structure. Those two peaks are a result of anti-symmetric nature of the gated plasmonic mode. The electric field intensity on a line passing through the diameter that is parallel to the polarization of the incident radiation is shown in Fig. 3.5.5(c). Two sharp and high electric field intensity peaks at 1.3 THz is observed near the center of the ring. The second mode shows four peaks as seen in Fig. 3.5.5(b) which is again because of the nature of the gated plasmons.

The summation of all electric field distribution over the complete spectrum of 1 –6 THz is shown

75

in Fig. 3.5.6(a) and Fig. 3.5.6(b). The total plasmonic interference pattern exhibits two peaks under the central ring that are very close to the central point of the ring. The distance between these two peaks is a few hundreds of nanometers. Vertical distribution of the electric field intensity in the cross section at the diameter of the plasmonic lenses is shown in Fig. 4b. The plasmons are confined in between 2DEG and circular gratings. Hence, the incident E field is confined not only in horizontal plane of plasmon propagation direction due to the lens structure but also in vertical direction in the 2DEG which results in a very large field intensity in a small volume under the central ring. Considering that the free space wavelength of the first resonant mode is

Figure 3.5.7: Shift of the plasma resonance frequency by electron concentration changes. (i) $N=7.5 \times 10^{12}$ cm^{-2}, (ii) $N=8.5 \times 10^{12}$ cm^{-2}, (iii) $N=1.1 \times 10^{13}$ cm^{-2}, (iv) $N=1.3 \times 10^{13}$ cm^{-2}

$\lambda=230\mu$m and the diameter of the central disc is D=1.3 μm, incident electric field is confined into a region with $\lambda/180$ linear scale. Taking the volume for free space unit wavelength of the same mode as λ^3 and the volume under the central disc in which the electric field is confined as $\pi r^2 t_{AlGaN}$ the volumetric confinement ratio could be found as 3.8×10^8.

An important advantage of the proposed devices is tunability of the resonant absorption frequencies through controlling the charge concentration by the applied voltage on the circular gates. Fig. 3.5.7 shows the transmission spectra of the investigated devices. The resonant frequencies clearly shift by the charge carrier concentration as expected from the Eq. (3.5.2). As the electron concentration increases, the plasmon resonance frequency presents a blue-shift. The shift is more prominent at higher order modes due to linear dispersion of plasmons at different electron concentrations.

Analytical Model

Starting with the approach of Steele *et al.*, the 2D electric field distribution of the plasmons can be expressed in cylindrical coordinates as

$$E_n^2(r,\phi) = E_0^2 \sin^2\left(\frac{2n\pi r}{L}\right) e^{-\frac{2r}{L_P}} \frac{1}{r^2} \sin^2(\phi) \tag{3.5.3}$$

where E_0 is the constant, n is the mode number, L is the period, L_P is the plasmon propagation length. First sinusoidal term describes the mode confined under the individual grating. Exponential term defines the propagation or dissipation loss of the plasmons as they propagate in the radial direction. Plasmons have a 1/r field distribution dependence on the distance from the center as they concentrate. The last sinusoidal term is the contribution of the polarization effect of the incident radiation on the circular grating. The z dependence of the E field has $e^{-\alpha z}$ with different α values for different mediums which is not included in the equation.
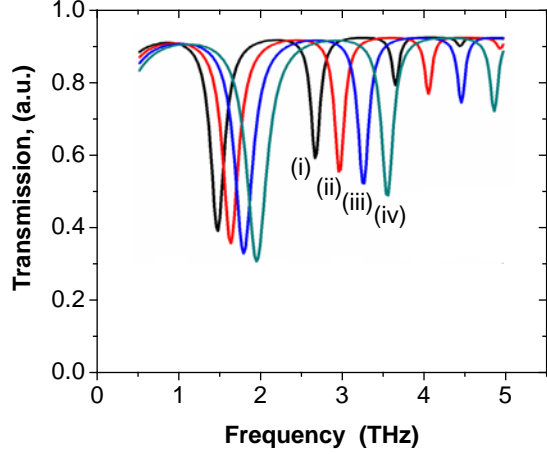
76
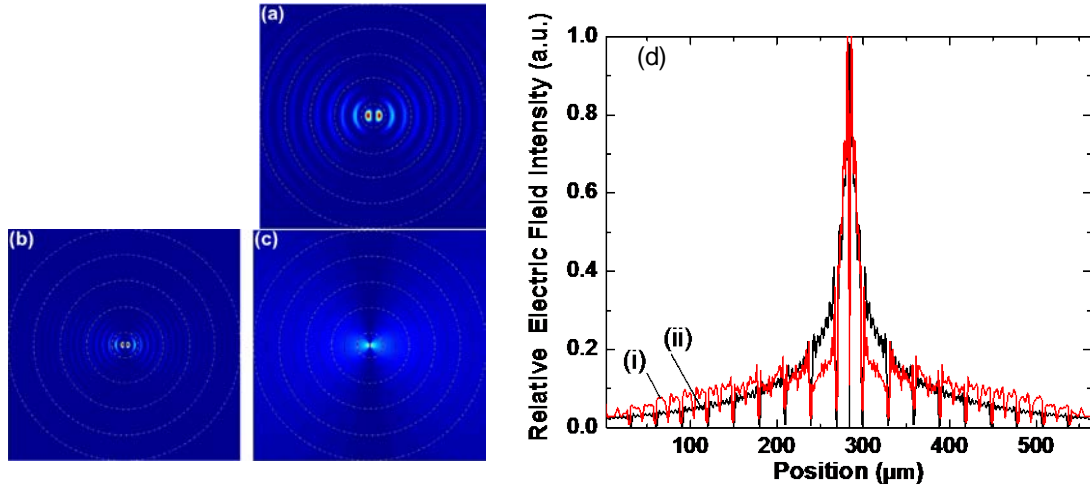
Figure 3.5.8: (a) Calculated electric field intensity of the fundamental mode in between the circular grating and 2DEG, (b) second mode, (c) summation of modes from 1 to 5. (d) Relative electric field intensity on the diameter parallel to the polarization of the incident radiation (i) numerical simulation (ii) Analytical calculation using Eq. (4).

The fundamental mode was calculated using the Eq. (3.5.3) with n=1 and the results are presented in Fig. 3.5.8(a). The highest intensity is observed under the central ring and 2 high electric field peaks are distinct. The second mode was calculated for n=2 and resulting electric field profile shows four high intensity peaks under the central ring as seen in Fig. 3.5.8(b). The summation of electric field intensity distribution from mode 1 to mode 5 is presented in Fig. 3.5.8(c). The total electric field distribution reflects the actual grating structure assuming with high duty cycle. Relative electric field intensity on the diameter parallel to the polarization of the incident radiation calculated by numerical simulations and analytical calculations using Eq. (3.5.3) are presented in Fig. 3.5.8(d). The results of the analytical model are in good agreement with the simulation results.

Effect of Duty Cycle on Focusing
The duty cycle (w/L) has a dramatic effect on the quality factor of the plasmonic modes. The electric field intensity under the central ring vs. frequency for different duty cycles is presented in Fig. 3.5.9(a). Two trends are observed in the plot: (1) Electric field intensity increase with the increasing duty cycle. (2) Electric field intensity increases with the resonant frequency to a maximum value and then starts decreasing. The latter trend is observed also in Fig. 3.5.4. As explained earlier, the resonant absorption in periodic gate structures reach to a maximum when the radiative damping γ_{rad} is equal to the dissipative damping γ_{dis} caused by the carrier scattering. Radiative damping strongly depends on relation between wavelength of the incident radiation and geometry of the structure and increases as the slit size gets smaller. Once it becomes equal to the dissipative damping the absorption and therefore the field intensity under the central disc reaches to a maximum. Further decrease of the slit size makes radiative damping larger than dissipative damping which causes absorption rate starts decreasing. The maximum also corresponds to an optimum slit width to wavelength ratio. As the wavelength changes for higher resonant modes, the radiative and dissipative damping becomes no longer equal or close to each other causing a reduction of absorption which results in the second observed trend. Higher electric field confined under the central ring due to larger duty cycles is shown in Fig. 3.5.9(b). Focusing effect is observable only if the quality factor of the modes high enough to reach to the central disc.
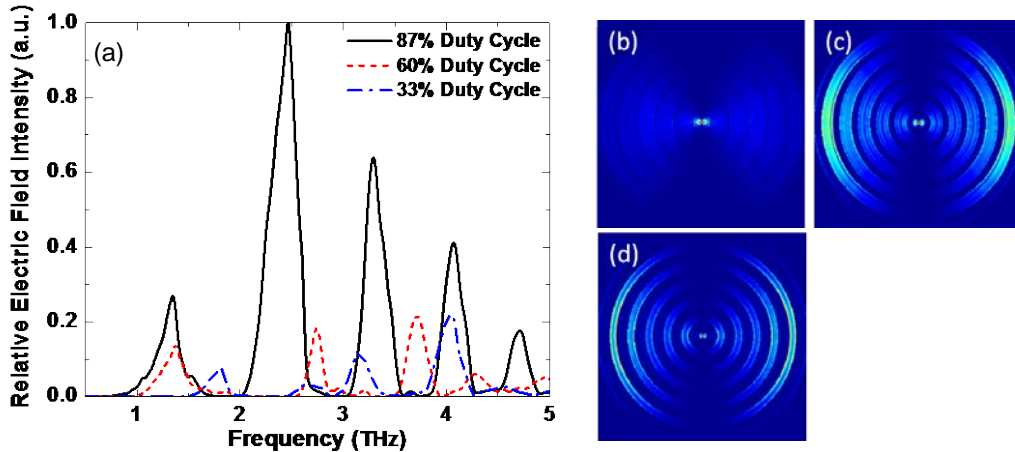
Figure 3.5.9: (a) Normalized electric field intensity under the central disc vs. frequency for different duty cycle of circular gratings. (b) Total electric field profile for 87% duty cycle, (c) 60% duty cycle and (d) 33% duty cycle.

Decreasing duty cycle increases the damping of the plasmons in the ungated regions and thereby prevents them forming a standing wave reaching to the central disc. Instead, plasmons in low duty cycle devices are confined under the outer circles. Fig. 3.5.9(c) and 3.5.9(d) clearly shows that as the duty cycle is modulated to lower values, the electric field intensity of the outer rings becomes comparable with the central ring. Moreover, as the duty cycle decreases, the cavities under the circular gates become isolated from each other approaching to the single gate case in plasmonic FETs reported in the literature. In this case, the dispersion relation is still given by the Eq. 3.5.2 however, plasmon wave vector k becomes $k = 2\pi n / L_G$ where L_G is the single gate length. This is clearly observed in Fig. 3.5.9(a) where the resonant peaks shift for the lower duty cycles.

Effect of Mobility on Focusing - A Comparison with Graphene Devices
Graphene has high electron mobility characteristics at room temperature which makes it a very attractive material for THz plasmonic applications. We investigated the response of the graphene based circular gratings to the incident THz radiation by modulating the electron mobility of the graphene. In our graphene lens design, a graphene layer is placed on a THz transparent substrate and covered by a thin layer of dielectric layer. On top of the thin dielectric layer, a circular grating structure is described as in GaN/AlGaN devices before. If we make an analogy with the Fig.1(b), sapphire layer is replaced instead of GaN layer, graphene layer is replaced instead of 2DEG, HfO_2 layer is replaced instead of AlGaN layer and circular grating structure is kept the same. Electron collision frequency and electron concentration used in our simulations are extracted from the recently published data in reference. Our simulation model is validated successfully by replicating the experimental data of THz transmission through graphene micro ribbons. The electron concentration is kept the same and the plasma collision frequency is modulated. As the plasma collision frequency increases, it corresponds to a decrease in plasma collision time or electron relaxation time.

Mobility of the electrons depends on electron relaxation time. The mobility used in simulations are 2,500 cm^2/V.s (CVD growth graphene on copper), 4,500 cm^2/V.s. (graphene on h-BN) 12,500cm^2/V.s (epitaxial growth graphene on SiC). The lower mobility causes the propagation loss to be dominant in the structure and lower the quality factor of the plasmons. Low quality factor
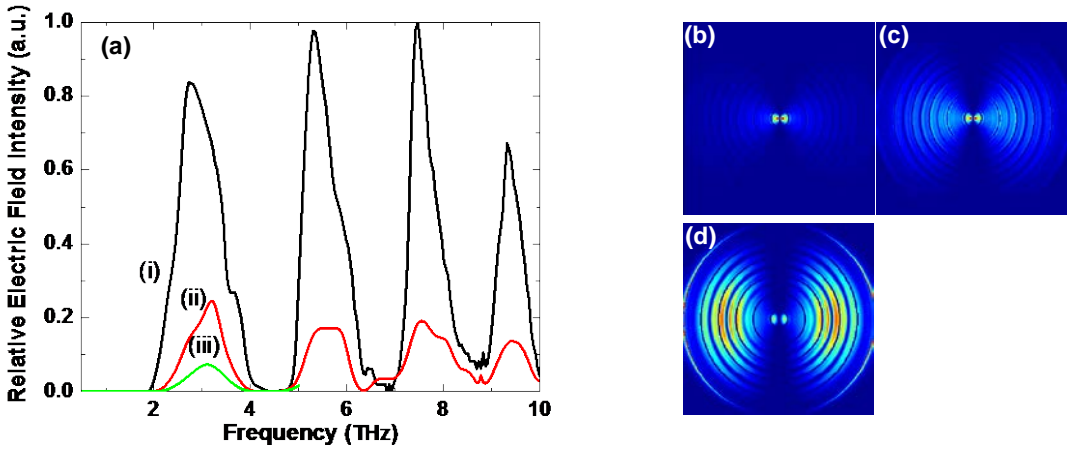
Figure 3.5.10: (a) Relative electric field intensity under the central disc vs. frequency for the graphene circular grating devices with different relaxation times of electrons in the channel. (i) μ=12,500 cm^2/V.s (ii) μ=4,500 cm^2/V.s (iii) μ=2,500 cm^2/V.s. Right panel shows the total electric field distribution in the circular gratings for (b) μ=12,500 cm^2/V.s (c) μ=4,500 cm^2/V.s (d) μ=2,500 cm^2/V.s

prevents the plasmons reaching from one gate to another and causes the loss of focusing ability of the circular grating structure. Fig. 3.5.10 (a) shows the electric field density ratios as a function of the incident THz radiation. The slightly visible shoulders on the peaks are attributed to the contribution of non-resonant absorption at the edges of the rings and could be mitigated with much finer mesh and longer computation time.

The high intensity peaks indicate the resonant plasmonic modes within the structure. As the mobility increases, the quality factor and the electric field intensity of the plasmons increases. The width of the first mode is decreasing with increasing mobility which indicates higher quality factor of the plasmonic mode. Total electric field distribution is shown in Fig. 3.5.10(b) for the device with graphene with highest electron mobility. A focusing effect can be observed for the highest mobility graphene. As the mobility decreases down to 4,500 cm^2/V.s, the focusing effect decreases as seen in Fig. 3.5.10(c) and the field density ratio goes down by a factor of 4. As the mobility goes down to 2,500 cm^2/V.s, the focusing effect cannot be observed that can be understood from Fig. 3.5.10(d). All these mobility values can still be used a polarization independent plasmonic tunable THz sensing because even at low mobility at the order of 2,000 cm^2/V.s, THz plasmons can be excited but they are unable to propagate long enough to form a standing wave. It is possible to improve the quality factor of the resonant modes by increasing mobility of the graphene layer. Temperature-dependent phonon-limited transport studies predict room-temperature intrinsic mobility reaching the values of above 100,000 cm^2 /V for graphene while room temperature electron mobility of 40,000 cm^2/Vs is reported for graphene on boron nitride substrates.

In summary, we analytically and numerically investigated circular gratings on GaN/AlGaN heterostructures and graphene with the capability of concentrating THz radiation into a region with λ/180 linear scale which translates to volumetric confinement of 3.8×10^8. The response of the concentrator devices is polarization independent due to their cylindrical symmetry. The electric field distribution over 2DEG/graphene layer shows highest electric field intensity peaks under the

central ring at resonant plasmonic modes that is a result of constructive interference of the plasmons. The focusing phenomena is strongly affected by the duty cycle where high duty cycled structures are able to focus plasmons better compared to the lower ones. Graphene active layer concentrator devices show higher quality factors for the plasmonic modes with their high mobility at room temperature which allows a more pronounced lens effect. Graphene devices with their potentially very high mobility could be effectively used for concentrators operating at room temperature in THz range as well as in the sub-THz range for many important applications.

3.5.3 Plasmonic Properties of Asymmetric Dual Grating Gate Plasmonic Crystals

Plasmonic terahertz oscillations in various types of field effect transistors (FETs) are used for THz detection, mixing, and generation. Plasmonic THz FET detectors are frequency tunable which makes them superior to the conventional detectors such as bolometers and pyroelectric detectors.

The 2DEG-based FETs support gated plasmons where electromagnetic fields of plasmons confined in between the 2DEG and the gate. FETs also support ungated plasmons where electromagnetic fields of plasmons are localized in the ungated regions. In an FET with periodically spaced gates, the grating gate supplies the necessary momentum in order to excite the plasmons by compensating the momentum mismatch between the THz waves in free space and the THz plasmons in the 2DEG channel.

Recently, highly sensitive terahertz detectors based on asymmetric dual-grating gate (ADGG) HEMTs have been demonstrated with 25kV/W record high responsivity but the plasmon dispersion in such structures has not been studied. In this study, in order to better understand the THz plasmons in ADGG HEMT, we calculated the dispersion relations for a 2DEG-structured lattice with one-dimensional (1D) translational symmetry, known as a 1D plasmonic crystal. The dispersion characteristics of plasmons reveals many important properties of the plasmons such as the localization of the plasmons, the electric field profile distribution, the group velocity etc. The charge distribution along the channel of the FET is especially important since they contribute to THz detection. Unlike uniform grating gate devices, ADGG HEMT device architecture has a geometry that cannot sustain a symmetric charge distribution. An asymmetric charge distribution can create a net dipole moment along the channel and result in a higher THz response. The THz-induced DC voltage response can be calculated by integrating the induced electric field distribution along the channel. Therefore, under-standing the field and charge distribution in the device and their effect on responsivity would allow design of better performing THz detectors. In this study we also investigated the absorption spectrum of the device since the response of the detector strongly depends on the absorption. The presented analyses of the plasmonic crystal dispersion are based on the optical properties of the THz plasmons in 2D cavities which are obtained using finite difference time domain (FDTD) method.
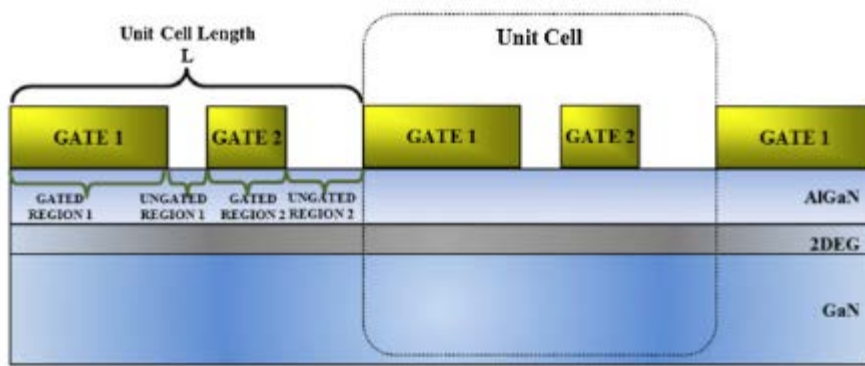
Figure 3.5.11: Schematic representation of an asymmetric grating gate plasmonic device showing the unit cell and the gated-ungated regions where the width of gated region 1 is 900 nm, width of ungated region 1 is 250nm, width of gated region 2 is 400nm, and width of ungated region 2 is 450 nm. The unit cell width is 2*m*m. The dielectric above the 2DEG is set to AlGaN and below is set to GaN.

A commercial FDTD simulation software was used in order to investigate the electromagnetic field profile of the plasmons and the dispersion of the plasmons in asymmetric grating gate structure. The structure is defined as AlGaN/GaN based HEMTs with a barrier layer of AlGaN and the 2DEG formed in the GaN. Fig. 3.5.11 shows the cross section of the simulated structure, where the unit cell includes 2 gates with different lengths with Bloch boundary conditions. The excitation was provided by a dipole source with a polarization perpendicular to the gratings. The simulation is repeated for different energy and momentum values. The plasmons are excited when the momentum and energy of the incident wave matches with the energy and momentum of the plasmons. The electric field profile of the excited plasmons is monitored in the gates, AlGaN, 2DEG and GaN regions. The 2DEG parameters are defined as a plasma material parameter, where plasma frequency and collision frequency are extracted from the previously reported experimental results for the electron concentration of 7.5×10^{12} cm^{-2} and the mobility of 40 000 cm^2/Vs at 4 K. Such a high mobility value which can be attained at cryogenic temperatures is necessary in order to excite high quality factor plasmons and to properly distinguish the plasmonic modes. For low mobility values, the modes are broadened and cannot be individually resolved since the full width half maximum of frequency represents the lifetime of the plasmons. The simulation is set to auto-stop when the total electric field in the simulation converges down to a small value, which is 6 orders of magnitude smaller than the incident field. The data is recorded for several simulations with different *k* vectors that is added to the Bloch boundary conditions with the largest *k* vector being half of the reciprocal lattice of the unit cell. Incident wave spectrum was selected to cover 0.1-5 THz range. The electric field profiles for each simulation were extracted to calculate the total electric field at each frequency and momentum value and mapped over a 2D graph by a custom code. It should be noted that due to the use of periodic boundary conditions, the presented results are for an infinite array of the unit cell described here accept for the responsivity measurement in Fig. 3.5.15.
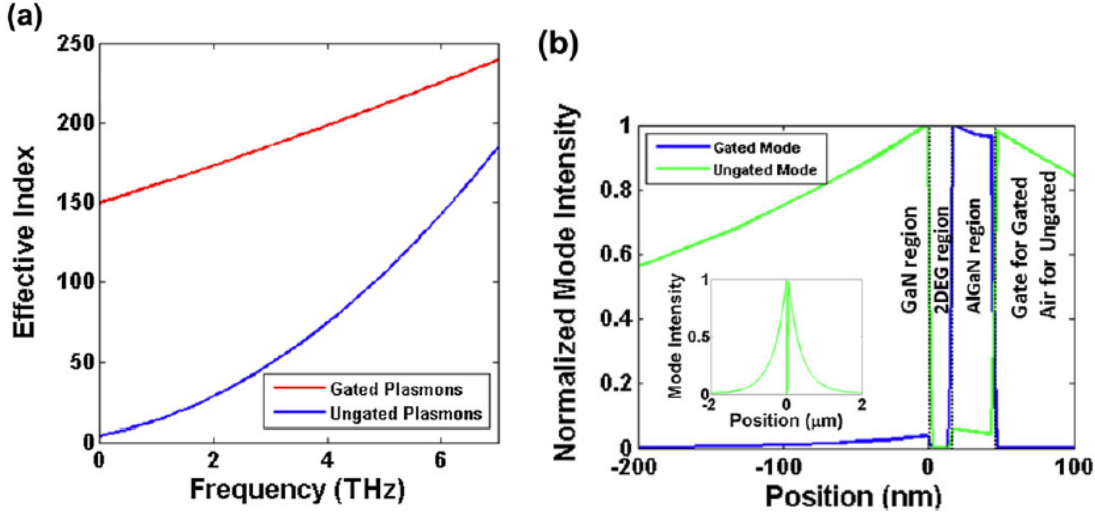
Figure 3.5.12: (a) Numerically calculated effective indices of plasmons at gated and ungated regions. (b) The mode profiles of gated and ungated plasmons at 2 THz. The inset is the extended ungated mode profile. The different material regions are separated with dashed black lines. The right-most region is considered as gate for gated modes and air for ungated modes.

The effective index of a resonant mode is a combination of gated and ungated plasmon effective indices since they are coupled and cannot be separated from each other. When we consider a uniform grating gate device with a very short gate where the limit of the gate length goes to zero, the effective index a resonant mode will be close to ungated mode. Conversely, in the long gate device where the limit of the gate goes to the periodicity, the effective index of the mode will be closer to the gated effective index of the plasmons. So, the effective index of a resonant mode is expected to be in the region between the gated effective index and ungated effective index shown in Fig. 3.5.12 (a). Also, for the short gates the effective index will be smaller compared to the longer gates. The effective indices (Fig. 3.5.12 (a)) are calculated via FDTD mode calculation method by taking the cross section of the gated and the ungated regions. The mode profile of the plasmons for gated and ungated regions are shown in Fig. 3.5.12 (b) for 2 THz. The gated plasmonic modes at lower frequencies are highly screened by the gate and tightly confined over the AlGaN region. Higher frequency modes tend to be closer to 2DEG with less screening resulting in smaller gate effect, which causes a dramatic index difference at lower frequencies. This effect can be observed in Fig. 3.5.12 (a), as the frequency increases, the effective index difference between the gated mode and ungated mode decreases. The effective index of plasmons under the gate is 15 times higher than the ungated plasmons at 1 THz.
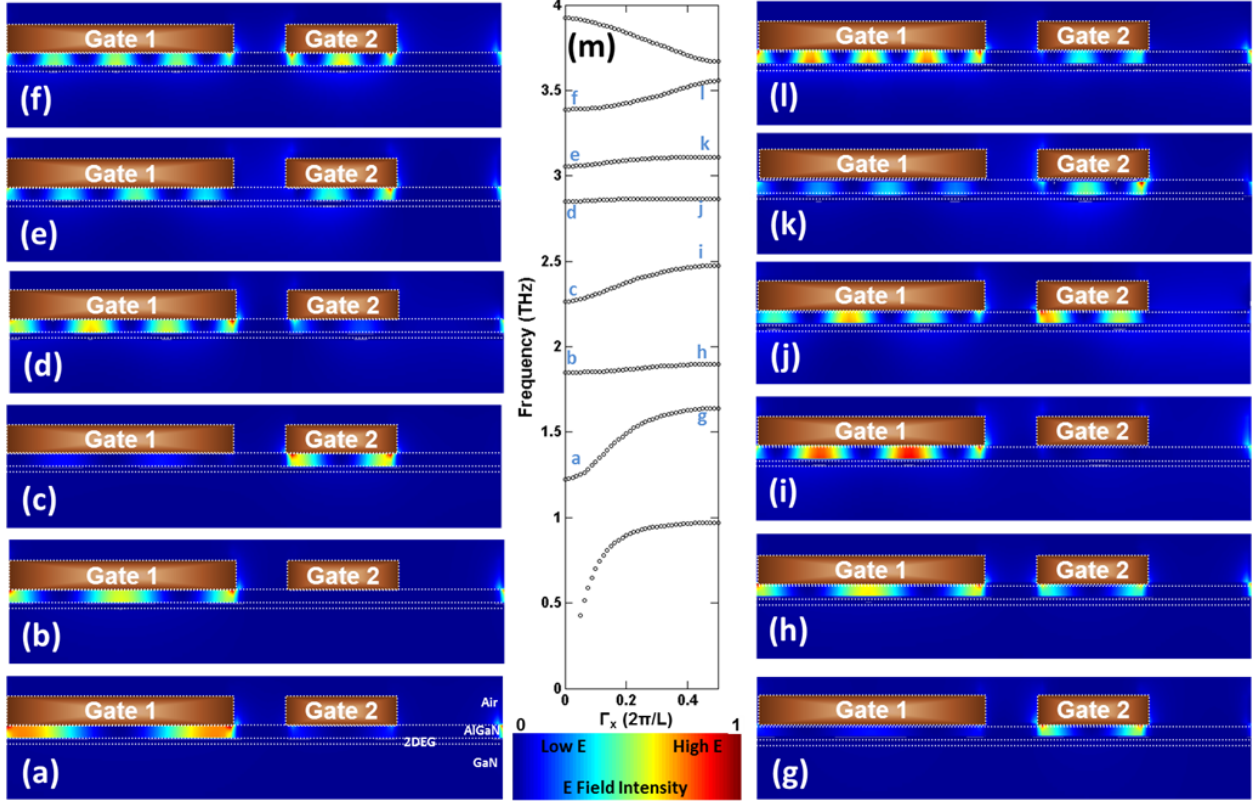
Figure 3.5.13 (a-l) Normalized Electric field distributions ($|E|^2$) at different wave vectors and energies. The modes on the left are zero momentum plasmonic modes; the modes on the right are half reciprocal lattice vector momentum plasmons. Red indicates the high electric fields and blue indicates the low electric field. The corresponding momentum-energy is indicated on the graph in blue letters. (m) The calculated dispersion of ADGG HEMT where x-axis is the momentum of the grating.

Fig. 3.5.12 shows the plasmonic dispersion characteristics calculated using FDTD method. The x-axis represents the plasmon momentum Γ_x in x direction where Γ_x at 0.5 is $G/2=n\pi/L$, G is the reciprocal lattice vector ($2\pi/L$), n is an integer; L is the unit cell length. The peak points are extracted using a custom code. The dispersion curves for the grating gated devices show that a band gap is opened up in several energy bands in which there are no propagating plasmons. The resulting dispersion curves are not similar to the uniform grating dispersion curves like having cavity like standing wave bands.

A periodic structure causes Bragg scattering of plasmons. This scattering results in forward and backward traveling waves, which forms a standing wave due to their constructive interference. If plasmon momentum is half of the reciprocal lattice vector G or 0, plasmons interfere constructively in the structure forming two standing wave profiles with different energy levels at the band edges. The high energetic plasmon standing wave profile, E_+, tends to localize over the lower index region, and the low energetic plasmon standing wave profile, E_-, tends to localize over the high index region. This is a result of the splitting of the bands at Brillion zones. If the energy of the plasmons falls between these two energy levels, plasmons interfere destructively resulting in no

83

propagation along the structure. This behaviour of plasmons causes formation of a band gap, which is known as the plasmonic band gap.

Fig. 3.5.13 (c) is an example for E_+ for which the mode is localized around the gated region 1 and (b) is an example for E_- for which the mode is localized around the gated region 2. Since the gated region 1 is wider than the gated region 2, the mode in the gated region 1 has a tighter confinement than the one in the gated region 2, which results in higher screening of plasmons and higher effective index of plasmons in the gated region 1.

The plasmonic mode distribution in Fig. 3.5.13 (b) has maxima under the gated region 1 while the maxima in Fig. 3.5.13 (c) is under the gated region 2. The modes corresponding to the 2nd branch (Fig. 3.5.13 (m)) are shown in Fig. 3 (a) and (g). The mode starts at gated region 1 and ends up in the gated region 2. Considering that the derivative of dispersion (*dw/dk*) is the group velocity, this branch corresponds to propagating plasmons with a non-zero group velocity and the mode maxima changes its location as the momentum changes. The 3rd branch has a semi-propagating behavior as its derivative (*dw/dk*) is smaller than the one of the 2nd branch. Hence, the mode profile at the lower side of the branch (point (b) in Fig. 3.5.13 (m)) is localized in the gated region 1 (Fig. 3.5.13 (b)) and as the momentum increases the mode profile does not totally relocate to the gated region 2. Instead, it partially shifts to the gated region 2. The same behavior is also observed for the 5th (Fig 3. (d) to (j)) and 6th (Fig 3.5.13. (e) to (k)) branches. Therefore, these plasmonic modes are weakly coupled localized modes. The 4th branch shows the same properties with the 2nd branch. The mode starts at the gated region 1 and totally shifts to the gated region 2 from (c) to (i). So these modes are the strongly coupled plasmonic modes. The observed behaviors of the branches are completely different than the ones for uniform grating gate devices.

The asymmetrical unit cell results in a non-uniform plasmonic mode distribution along the channel, which causes non-uniform charge distribution with dipoles along the channel. The unit cell behaves as a net dipole source and creates a potential difference between its two ends. Therefore, the entire device with several unit cell behaves like a collection of serially connected voltage sources which could yield high responsivity for an incident THz wave.

We also calculated the absorption and response of the periodic device using FDTD method. Since we use Bloch boundary conditions, the structure is considered as infinite number of unit cells. A perpendicular plane wave source was set up to illuminate the device from the top along with a monitor at the back of the source to record the reflected wave, another monitor at the bottom of the device buried inside the GaN layer to record the transmitted wave. We monitored the electric field in the 2DEG and integrated it along the *x* direction, (along the 2DEG channel) to calculate the voltage response of periodic structure. Fig. 3.5.14 (a) shows the THz absorption of the periodic structure as a function of incident wave frequency. The corresponding resonant plasmons distributions are shown in Fig. 3.5.13 a-f respectively. The momentum of the incident wave is set to zero in the direction of the grating momentum, and hence, the parallel component of the incident wave is zero. Seven different resonant modes are observed in the absorption spectrum with different amplitudes the maximum of which reached to 30%. This behavior is quite different from a typical absorption spectra for a uniform grating gate device where the absorption of the fundamental mode is the highest and absorption decreases with increasing mode number. Fig. 3.5.14 (b) also shows the response of a single unit device for the same spectral range along with

84

the absorption in semi-log scale. There is a correlation between the THz response and the absorption, as the absorption increases, the response also increases. The responsivity of one unit cell can reach higher than 10 kV/W; which is in agreement with the experimentally measured value of 25 kV/W for a similar ADGG HEMT in which they had multiple unit cells that should add up like a linearly connected voltage source that is why their responsivity is higher.
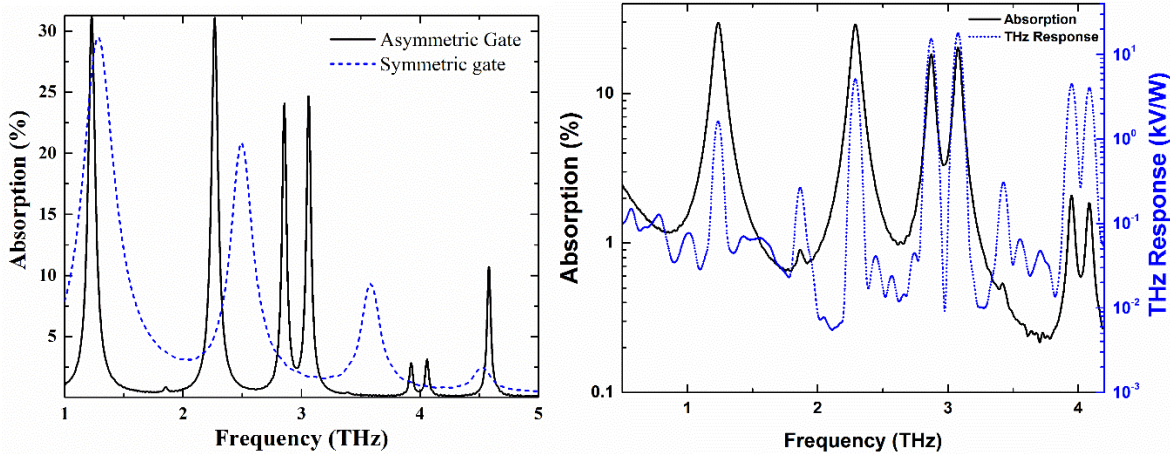
Figure 3.5.14: (a) The absorption comparisons of a uniform grating with 900 nm gate width and 100 nm slit width and the asymmetric grating gate structure discussed in this paper. (b) Calculated absorption of the incident plane wave over the device, y-axis in log scale and Calculated THz response of the device in y-axis log scale.

The non-uniform responses and absorptions of the resonant modes are caused by the asymmetric unit cell. In a grating gate device, the absorption depends on the dissipation losses and radiative losses of the modes. The dissipation loss is proportional with the frequency, as the frequency increases, the dissipation loss increases, and the radiative loss is proportional to the gate length to slit length ratio, as the ratio decreases, radiation loss increases. The two different gate length results in different amount of radiative loss and each plasmonic mode has different amount plasmonic confinement under the gate 1 and gate 2 which results in a different amount of radiative loss in each mode. Such a behavior causes non-uniform amount of absorption as a function of frequency. Fig. 3.5.14(a) also presents a comparison of the absorption of the ADGG device to a symmetric gate device.

In conclusion, we investigated the dispersion characteristics of an asymmetric dual-grating gate (ADGG) HEMT structure in detail using FDTD numerical methods. The dispersion of the structure presented several energy band gaps in which no propagation is allowed. The branches in the dispersion are completely different than the ones in dispersion of uniform grating devices. ADGG device can support tightly confined /weakly coupled behavior and propagating/strongly coupled plasmonic modes with asymmetrical charge distributions. This non-uniform charge distribution along the channel can result in high responsivity which makes the ADGG devices a promising candidate for tunable solid-sate THz plasmonic detectors.

3.5.4 Tunable THz Wave Absorption by Graphene-Assisted Plasmonic Metasurfaces based on Metallic Split Ring Resonators

A monolayer of carbon atoms in a honeycomb lattice orientation is well-known as "graphene" that has been introduced as a promising two-dimensional structure in designing optical nanoantennas, opto-electronic photodetectors, optical and terahertz (THz) modulators, photocatalyst, biological agents, quantum information processing, photonic metamaterials, light harvesters, and DNA sensors. Graphene yields excellent mechanical flexibility and perfect electro-optical features such as enormous electronic mobility and ultra-fast carrier dynamics. As a recent progress, a substrate of graphene layer and an array of plasmonic metallic nanostructures on top has been introduced as graphene plasmonics and widely employed in designing numerous types of plasmonic nanostructures such as photocurrent generation and light harvesting applications. Graphene plasmonics provides tremendous electromagnetic (EM) field confinement in subwavelength regime due to the broadband absorption property of graphene layer during light-matter interaction. The intensified EM field in doped graphene layers can be exploited as an alternative method instead of regular plasmon resonance excitation and localization techniques in noble metallic particles which suffer from dramatic ohmic losses and limited structural tunability. This unique ability of graphene originates from its charge carriers of zero effective mass (Dirac Fermions), which allows for long travel distances of EM wave without significant amount of scattering. Additionally, the linear dispersion of the two-dimensional (2D) Dirac Fermions yields extraordinary wideband tunability under various implementations, while this feature can be affected by its weak interaction with incoming light due to low carrier concentrations. Besides, due to lack of free charges, graphene is considered as a semi-metal substance. Technically, free carriers can be induced via chemical doping or electrical gating easily due to the inherent structural nature of graphene, and obtained free carriers in graphene is almost 0.01 per atom, or doping concentration of 1×10^{13} cm^{-2}, which is dramatically lower than regular metals. Thus, the two-dimensional property and semi-metallic behavior of graphene provides tremendous electrical tunability not as much as regular metals. However, this natural imperfection of graphene can be treated by employing metallic nanoscale structures in designing correlating nanoscale devices. For instance, graphene-metal compositional structures can be utilized in designing artificial metamaterials (MMs) as a platform for optimizing the light-matter interactions in nano and microscale dimensions.

Plasmonic MMs are promising artificial structures with unique properties beyond natural materials which consist of nano- and micro-sized metallic (dielectric) resonant building blocks or particles to support strong plasmon (EM) resonances in the optical and THz frequencies. As a specific case, employing plasmonic metallic structures in designing MMs allows for designing structures for various applications such as plasmonic photomixers, plasmonic biochemical sensing, broadband light bending, and coherent emission lensing. In recent years, MMs have witnessed remarkable developments, and the quality of these structures has been improved by using various techniques such as using different types of metallic arrangements as meta-atoms and utilizing high absorptive multilayer metasurfaces. Newly, graphene sheets have been utilized as a substrate layer in designing MM structures with supporting light-matter interactions in the THz frequencies. It is shown that for a finite graphene sheet, the absorption coefficient is emphasized by $\alpha = e^2/\hbar c \sim 1/137$ ($\alpha\pi \approx 2.3\%$), and also, the universal optical conductivity of graphene is almost $e^2/4\hbar$. In practical applications, graphene plasmons are able to confine to volumes in the range of $\sim\alpha^{-3}$ which is much

smaller than the diffraction limit and this facility allows for ultrastrong light-matter interaction. Moreover, more than the material and quality of metasurafces in designing a MM structure, the shape and orientation of the employed structures play a key role in EM field manipulation and confinement.

Evaluating the behavior and applications of numerous MMs, it is proved that THz-MMs are able to support sharp and antisymmetric Fano resonances (FRs) depending on the structural and chemical features of the employed metasurface and metallic or dielectric components. Technically, FR arises from the constructive and destructive interferences between a narrow and sharp discrete resonance and a wide spectral line. In addition, plasmon-induced transparency (PIT) has been newly introduced for plasmonic MMs which refers to the absorption cancellation of EM waves at certain frequencies (transparency) and being non-transparent otherwise. Technically, PIT includes coupling of appeared two opposite bright and dark resonator modes in a unit cell or meta-atom of a MM. The bright resonator here is a high radiative broad resonant mode, while the dark resonator is the non-radiative narrower resonant mode. A destructive interference between these opposite modes gives rise to formation of sharp resonant linewidth (narrow transparency window), termed as "Fano resonant" mode. The sharpness, position, and number of FRs are the major factors in determination the quality factor (Q-factor) of various MMs, specifically for sensing and switching purposes.

In this article, we report on multiple and sharp Fano dips arising from a tunable plasmonic MM comprising of Silver (Ag) concentric split ring resonators (CSRR) deposited on a multilayer metasurface including silicon and monolayer graphene (Si and C) layers. Herein, we describe the design of graphene plasmonic MM by defining the spectral response of the structure, numerically. Investigating the plasmon response of the THz MM, the unique features and functionalities of the structure such as strong polarization dependency, PIT, and double sharp FRs formation are introduced and discussed. Moreover, we examined the behavior of the MM with and without presence of graphene layer to describe the effect of this monolayer on the performance of the THz plasmonic MM.

Numerical modeling

The formation and excitations of plasmon resonant bright and dark modes and their interference are investigated using the finite-difference time-domain (FDTD) method (Commercial Lumerical simulations package 2015). In the simulation, to determine the plasmon response for the proposed plasmonic metamaterial, following simulation parameters were employed: The spatial cell sizes were set to $d_x=d_y=d_z=0.05$ μm, and 64 perfectly matched layers (PMLs) were the boundaries. Additionally, simulation time step was set to the 0.01 fs according to the Courant stability. The light source was a linear plane electric source with a pulse length of 2.6533 fs, offset time of 7.5231 fs, and with the intensity of 1 mW/μm^2. We assumed that periodic arrays of Ag-CSRR arrangements are deposited on a multilayer substrate composed of a lossless Si layer under a SiO$_2$ substrate with the permittivity of ε~11.6 and 2.05, respectively. The Ag particle was modeled as a lossy metal with a conductivity of $\sigma_{Ag}=6.30\times10^7$ S.m^{-1} at T=300 ºK. In our FDTD simulations and analysis, we exactly simulated the structure using experimental conditions data, including light reflection at the SiO$_2$/Si (metasurface) interface.

Theoretical calculations

To determine the absorption cross-sections and also, to quantify its percentage for the plasmonic MM, we utilized two-dimensional dyadic Green's functions (DGFs). Comparing the operation frequency (THz) and the overall size of the employed Ag-CSRRs ($d \ll f$, where f is the frequency of the incoming spectrum, and d is the outer radius of a CSRR unit), therefore, CSRR units can be described by DGFs theoretically. For analytical computations, we assumed the monochromatic time harmonic as: $\exp(-i\omega t)$, and the electric dipole moment as below:

$$p_{mn} = p \exp\left(ik_{xy}\left(r_{mn} - r\right)\right)$$

(3.5.4)

where mnth indicates the position of particles in an array, $\boldsymbol{p}$ is the total electric dipole moment for each one of Ag-CSRR units on the multilayer metasurface, the Bloch vector is defined by $k_{xy} = k_x\hat{x} + k_y\hat{y}$ and r_{mn} specifies the position of Ag-CSRRs on the metasurface as $r_{mn} = r + D_{CSRR}\left(m\hat{x} + n\hat{y}\right)$, in which $r = x\hat{x} + y\hat{y} + z\hat{z}$. Then, considering two-dimensional periodic DGFs that were proposed by Campione *et al.*, the total electric and magnetic fields in a MM system composed of plasmonic structures on a metasurface are given by:

$$E_{total}(r,k_{xy}) = E_{exc}(r) + E_{ref}(r) + \underline{G}^{\infty}_{ml}\left(r,k_{xy}\right)p$$

(3.5.5)

$$H_{total}(r,k_{xy}) = H_{exc}(r) + H_{ref}(r) + \underline{G}^{\infty}_{ml,H}\left(r,k_{xy}\right)p$$

(3.5.6)

where $\underline{G}^{\infty}_{ml}\left(r,k\right)$ and $\underline{G}^{\infty}_{ml,H}\left(r,k\right)$ are the multilayered electric (E) and magnetic (H) DGFs for the periodic array of particle arrangements correlated with the induced electric dipole moment to the electric and magnetic fields, respectively, E_{exc} and H_{exc} are the incoming electric and magnetic fields to excite plasmon resonant modes, E_{ref} and H_{ref} are the reflected part of the electric and magnetic incident optical power by multilayer metasurface. Therefore, for the metallic particles arrangements with the polarizability of α_{CSRR}, under EM field excitation with the incidence angle of φ, with the wavevector of $k_{xy} = k_x\hat{x} + k_y\hat{y}$, $E_{exc}(r) = \hat{z}E_{z,exc}\exp(ikr)$ and with "$j=1, 2, 3... M$" number of Ag-CSRR units, the absorption coefficient is defined by:

$$A = -k_0\sqrt{\varepsilon_{effective}}\left(\frac{k_0^3\sqrt{\varepsilon_{effective}}}{6\pi\varepsilon_0} + \text{Im}\left(\frac{1}{\alpha^{ee}_{CSRR}}\right)\right)\left(\varepsilon_0\varepsilon_{effective}\left|E_{exc}\right|^2 D_{CSRR,x}D_{CSRR,y}\cos\varphi\right)^{-1}\sum_{j=1}^{M}\left|p_j\right|^2 \quad (3.5.7)$$

where k_0 and ε_0 are the free space wavenumber ($k_0 = \omega\sqrt{\varepsilon_0\mu_0}$) and permittivity, respectively, $D_{CSRR,x}$ and $D_{CSRR,y}$ are the intercenter distance between proximal Ag-CSRR units in the x and y directions, respectively, and $\varepsilon_{effective}$ is the effective permittivity of MM composed of two dielectric and semiconductor layers and CSRR arrays which is driven by following equation:

$$\varepsilon_{effective} = 1 + \frac{k_0 H}{V_{CSRR}\varepsilon_0}\left(\text{Re}\left(\frac{1}{\alpha_{CSRR}^{ee}}\right)\tan\left(\frac{k_0(h+h_{CSRR})}{2}\right) - \frac{\eta_0\omega}{D_{CSRR,x}D_{CSRR,y}}\sin^2\left(\frac{k_0(h+h_{CSRR})}{2}\right)\right)^{-1} \quad (3.5.8)$$

where η_0 is the free space wave impedance $\eta_0 = \sqrt{\mu_0 / \varepsilon_0}$ (μ_0 is the permeability of the free space),

V_{CSRR} is the volume of an Ag-CSRR unit cell which is $V_{CSRR} = \frac{\pi h_{CSRR}}{2}\left((b^2 - a^2)\beta_1 + (d^2 - c^2)\beta_2\right)$, and

$(h+h_{CSRR})$ is the sum of metasurface and concentric rings heights. Both real and imaginary parts of effective permittivity are calculated and depicted in the next section. The polarizability of a concentric split nanoring resonator in an edge-coupled orientation was investigated analytically and experimentally by Marqués *et al.* and Capolino. Due to the structural similarity between proposed CSRR with the edge-coupled split nanoring resonator, the same mechanism can be utilized to define the physical features such as polarizability for proposed microscale structure. Accordingly, each one of the proposed CSRR systems acts as a *LC* circuit and the resonance frequency for this metallic microstructure is given by:

$$\omega_0^2 = \frac{2}{\pi L C_u R_{av}} \quad (3.5.9)$$

where, the capacity of the unoccupied spot between concentric nanorings is indicated by C_u, L is the total inductance of an Ag-CSRR unit (with ohmic losses) that can be computed by determining the magnetostatic energy for the total current intensity supported by the ring resonator, and $R_{av}=(a+d)/2$ expresses the average radius of the CSRR unit. Finally, summarizing the employed method by Capolino, the electric polarizability for a CSRR unit can be rewritten as a function of capacitance, conductivity, resonance frequencies, and inductance as below:

$$\alpha_{CSRR}^{ee} = \frac{16}{3\mu_0}\left(\frac{\pi R_{av}}{t_{av}h_{CSRR}\sigma_{Ag}}\right)\left[\frac{\omega_0^2}{\omega_{FRD}^2} - 1\right] \quad (3.5.10)$$

where t_{av} describes the average thickness of the rings as follows: $t_{av} = (d-c)(b-a)/2$, and ω_{FRD} is the Fano resonant dip frequency appeared in the amplitude transmission profile. In view of the importance of using noble metallic structures for THz-MMs, we adopt the experimental data from Huang *et al.*, which are well described at THz regime by the Drude model for Bulk conductivity as below:

$$\varepsilon(\omega) = 1 - \frac{\omega_p^2}{\omega(\omega + i\gamma)} \quad (3.5.11)$$

where ω is the angular frequency, ω_p is the plasma frequency (1.37×10^{16} rad/s), and $\gamma=2.73\times10^{13}$ rad/s.

Results and discussion

Figure 1(A) shows the geometrical parameters of a CSRR with two different split angles (β_1 and β_2), and these split angles provide required antisymmetric geometry to induce dark modes in the transmission amplitude spectra. The angle of split sections for both of the rings were set to be equal as $\beta_1=\beta_2$ (for details see Fig. 3.5.15(A)). Figure 3.5.15 (B) displays a three-dimensional schematic for the proposed plasmonic MM structure with the description of geometrical parameters inside composed of Si and SiO$_2$ layers. The direction of propagating vector, and incident magnetic and electric fields are indicated by arrows. The interparticle (center-to-center) distance between proximal CSRRs in x and y directions were set to 44 μm and 46 μm for $D_{CSRR,x}$ and $D_{CSRR,y}$, respectively (See the top view of MM in Fig. 3.5.15(C)). In other words, the edge-to-edge distance between proximal Ag-CSRRs in the x and y directions are 4 μm and 6 μm, respectively. In terms of chemical characteristics, we used metallic and dielectric materials with experimentally determined CRC and Palik constants, respectively.
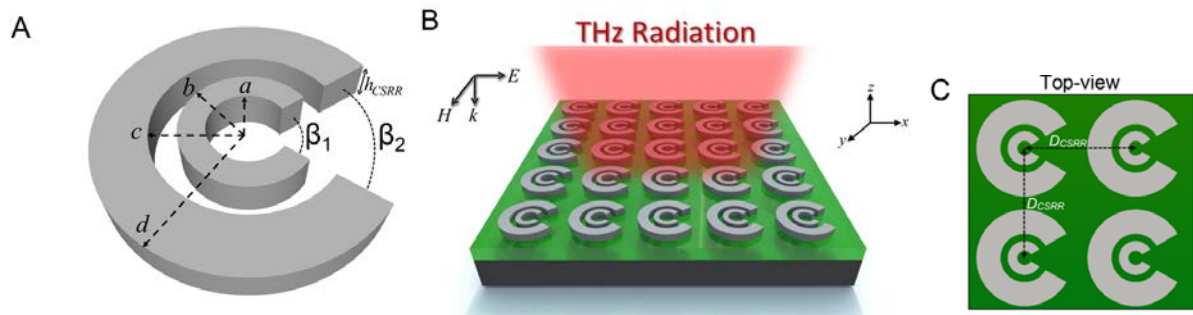

Figure 3.5.15: A) Schematic illustration of a single Ag-CSRR unit with the description for geometrical dimensions inside, B) schematic design of the plasmonic MM composed of Ag-CSRR units deposited on a multilayer metasurface consists of SiO$_2$@Si with the height of h, C) a top-view of MM which shows the interparticle distance parameters between proximal Ag-CSRR units ($D_{CSRR,x}$, $D_{CSRR,y}$).

Herein, we first examine the plasmon response of the proposed MM without graphene substrate. In this regime, periodic arrays of CSRRs are suited on a SiO$_2$@Si substrate with the overall thickness of h=900 nm (the height of Si is 500 nm and SiO$_2$ is 400 nm). Calculating the plasmon response for the structure, we plotted the transmission spectra "T" as a cross-sectional profile numerically which is shown in Fig. 3.5.16(A). According to the PIT mechanism, two distinct Fano dips are appeared at f=1.90 THz and 3.75 THz. Technically, in an isolated CSRR system, the outer split particle supports strong incident light-matter interaction (arising of the bright mode) and the inner split particle provide required dark resonant mode and the result of a destructive interference between these modes is the formation of pronounced Fano minima in the transmission spectra. Also, perfect adjustment of the split angles sizes leads to formation of strong dipolar and multipolar (quadrupolar) modes. Depicted inset diagram shows the applied electro-optic signal amplitude (V/m) over the beam delay time in picoseconds (ps) time scale to excite surface plasmon resonances in the proposed MM. Figure 3.5.16(B) exhibits calculated effective electric real and imaginary permittivities over the frequency variations for the proposed plasmonic THz-MM using numerical methods. Both plotted material parameters behave in a physically sound manner and due to the presence of Ag-CSRRs arrays on the metasurface with the absorptive behavior, hence, the imaginary permittivity is appeared with a distinct peak close to the secondary transmission window at f~3.60 THz correlating with the Fano dip.
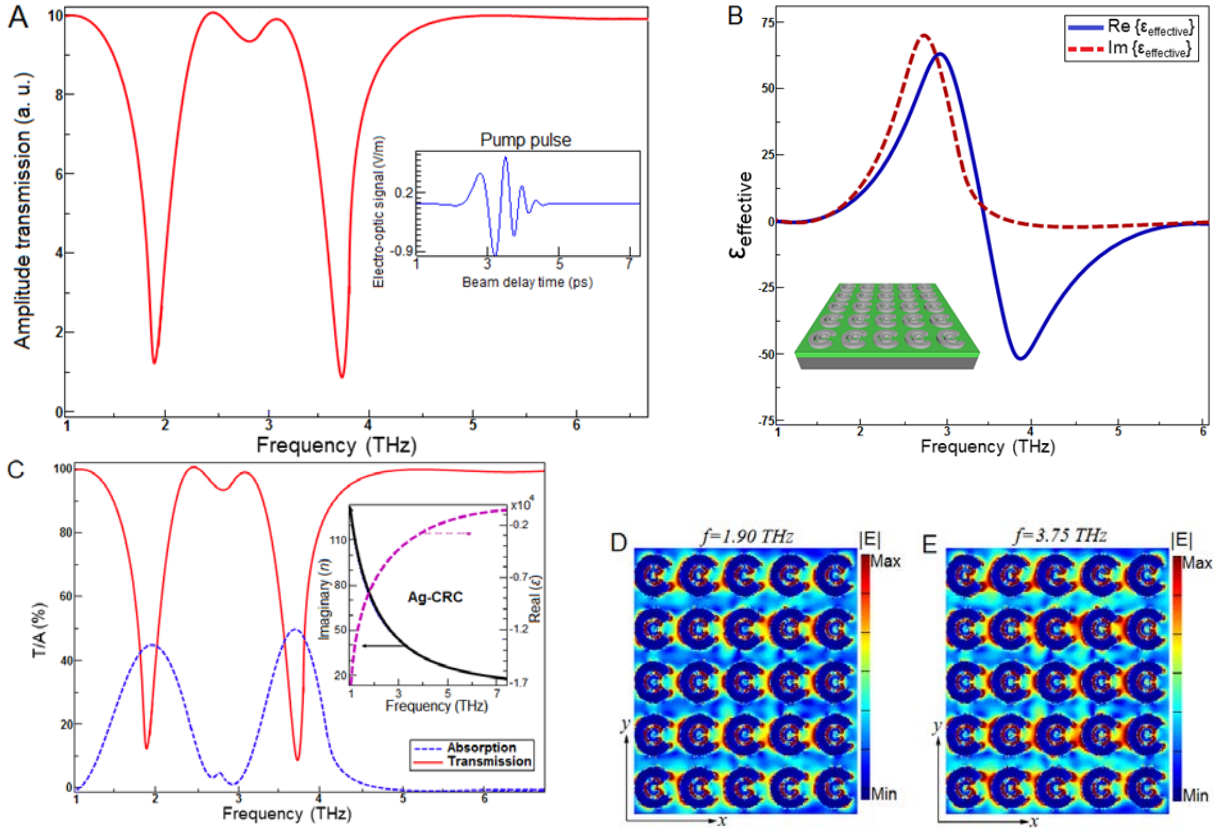
Figure 3.5.16:. A) Amplitude transmission spectra over the THz frequency for the plasmonic MM for CSRRs with the size of (*a/b/c/d*) = (2.5/7/10/20) μm and height of h_{CSRR}=350 nm. The inset shows the pump pulse or applied electro-optic signal over the beam delay in femtosecond, B) calculated effective real and imaginary permittivities for the plasmonic THz-MM, C) transmission and absorption coefficients spectra as a function of THz beam for the plasmonic MM. Inset is the real and imaginary parts of permittivity and refractive index of Ag with CRC constants for THz regime, D and E) two-dimensional *xy*-view snapshots for plasmon resonance excitation and coupling in a plasmonic MM for two different THz frequencies correlating with the Fano resonant modes.

Next, we quantified the percentage of the transmission *T* and absorption *A* factors for the plasmonic MM during illumination with a plane wave as an incident wave which propagates under normal incidence (*k*) with the electric (*E*) and magnetic (*H*) field polarized along the *x* and *y* directions, respectively. According to the plotted profile in Fig. 3.5.16(C), two distinct shoulders are appeared correspond to the position of Fano resonant dips (*f*=1.90 THz and 3.75 THz) which yields a broadband absorption facility in THz regime. As it was expected, the maximum percentage of absorbance is appeared at the position (frequency) of Fano resonance minimum due to accumulation of plasmon resonances by CSRRs arrays at this resonance frequency. Additionally, the absorptive property of Ag-CSRRs has an important contribution in optimizing the absorption ratio in this MM. As shown in the specular absorption spectra, we defined the absorption coefficient as approximately *A*(%)~47.9% at *f*=3.75 THz (the highest obtained peak) for the MM structure with geometrical dimensions that are explained in the figure legend. Comparing the performance of the examined THz-MM with analogous plasmonic or all-dielectric THz-MMs, the presented configuration provides supporting of sharp and double Fano resonant modes including broadband absorption property with high percentage. The inset diagram shows experimentally

determined CRC constants for real and imaginary parts of refractive index and permittivity for an isolated Ag metal which proves its strong absorption ability. To show the plasmon resonance excitation and coupling inside the proposed compositional MM, we extracted two-dimensional numerical snapshots at the Fano resonant mode frequencies which are displayed in Figs. 3.5.16(D) and 3.5.16(E). According to these simulation pictures, the maximum of plasmon resonance excitation is appeared at the split angles, and also in the spot between concentric rings in each one of the Ag-CSRR units which provides an ability to support strong Fano dips at the THz regime by the plasmonic MM.

Technically, geometrical parameters of the employed CSRR units play key roles in the quality, position, and percentage of the absorption and transmission profile. We have already explained the effect of split angles on the structures' performance. To show the effect of this parameter on the absorption efficiency and its percentage, we depicted the absorption profiles as a function of THz domain during modifications in both split angles (β_1 and β_2), separately in Figs. 3.5.17(A) and 3.5.17(B). To calculate these profiles, we assumed that during modifying one of split angles, the other one is kept fixed to 45°. Obviously, for both of the split angles, increasing the size of this parameter causes missing large area of the microstructure and the result of this modification is losing the ability to support strong incoming THz wave, hence, pronounced Fano resonant dips cannot be induced in the transmission profile effectively. In contrast, decreasing the angle of the gaps gives rise to support strong light-matter interactions, however, interestingly, this advantage includes losing formation of Fano dips due to the cancellation of required geometrical antisymmetric feature in the CSRRs to arise intense dark modes. Evaluating the effect of these split angles, the angle of the outer ring (β_2) plays major role in comparison to the inner ring split angle (β_1). This superior influence of β_2 directly related to the interaction of incoming THz wave and formation of bright mode, and also, its bigger size. Noticing in depicted diagrams for the absorption profiles in Figs. 3.5.17(A) and 3.5.17(B), decreasing the size of both split angles leads to blue-shift in the position of the absorption peak to the longer frequencies, and in contrast, by increasing the size of the split angles, we detected a red-shift of the absorption extremes to the shorter frequencies. The reason of this blue- and red-shifts is directly associated to the behavior of Fano dips during structural modifications, specifically for split angles.
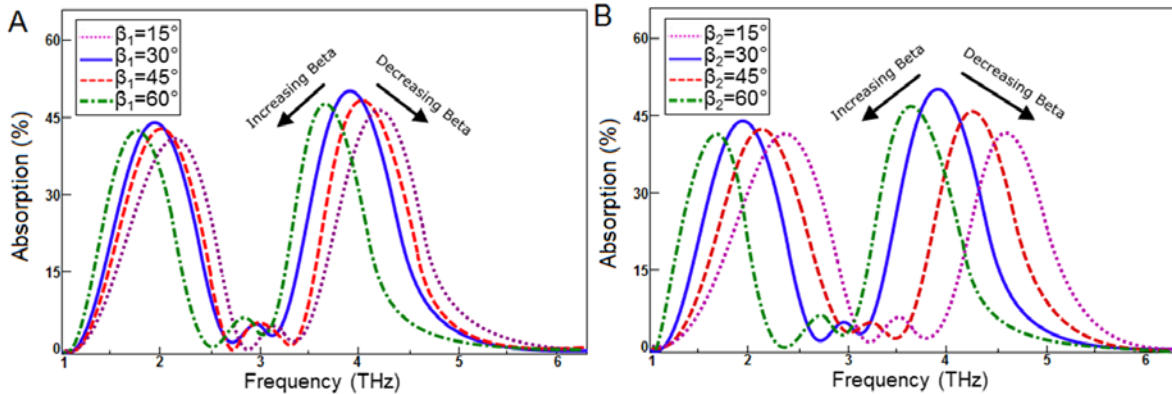

Fig. 3. A, B) Absorption spectra for THz-MM during modifications in the split angles sizes (β_1, β_2). The effect of modifications on the absorption coefficient is shown by arrows.

We plotted the transmission spectra for the proposed MM during variations in the split angles sizes in Figs. 3.5.18(A) and 3.5.18(B), numerically. Obviously, increasing (decreasing) the size of both split angles leads to red-shift (blue-shift) in the position of both Fano dips in the transmission profile. It is already explained that by increasing (decreasing) the size of split angles, the energy of dark modes decreases (increases) significantly and minor variations in these parameters causes significant alterations in the quality and position of Fano resonant dips. On the other hand, the geometrical and chemical properties of the utilized metasurface have a significant influence on the performance of MM which particularly changes the coefficient of the absorbed THz wave. Herein, we employed multilayer metasurfaces with perfectly defined thicknesses to enhance the performance of the plasmonic THz-MM as high as possible. To improve the performance and plasmon response of plasmonic structures includes MMs new methods have been utilized such as trapping the incoming light by using anisotropic slabs, gratings, and cladding, omnidirectional absorbers, and using a thin graphene layer as a substrate. The last mechanism has received great attraction due to its unique performance in a wide range of spectra. Generally, most of graphene sheets with variant doping yield high absorption ratio in the range of f=1 THz to 3 THz. Therefore, for the studied MM, placement of a monolayer thin graphene in designing the metasurface, the absorption ratio can be improved by keeping pronounced multiple Fano dips in the transmission profile. Recently, a mixture of dielectric substrates and graphene cut-wire sheets has been employed to increase the absorptance of optical energy with the percentage near to $A(\%)\sim 50\%$ includes formation of a deep minimum in the transmission profile at THz frequencies. However, the major problem with the performance of the graphene-based MMs is the narrow band absorption spectra in THz frequencies. Using lossy components such as metallic structures and multilayer metasurface are the major solution to enhance the absorption coefficient via accumulation and localization of plasmon resonant modes and inducing Fano dips.
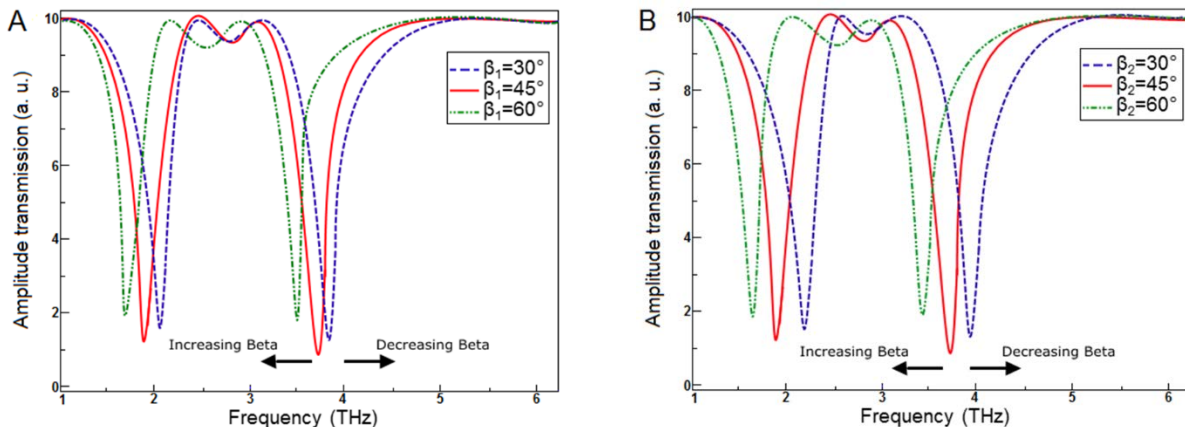
Figure 3.5.18: A, B) Amplitude transmission profile during modifications in the split angles sizes (β_1, β_2). The effect of modifications on the position of Fano dips is shown by arrows.

Comparing the achieved results for the proposed structure (composed of metallic microparticle arrangements and multilayer metasurface) with analogous MMs, the superior performance of the studied configuration in supporting sharp and narrow Fano dips in THz regime with broadband

absorption is clear. However, this performance is improvable using graphene layers in designing compositional metasurface. To this end, we covered the metasurface with a thin monolayer graphene sheet below the Ag-CSRRs arrays according to the proposed method by Fang *et al.* for a graphene plasmonic photodetector. Figure 3.5.19(A) shows a three-dimensional schematic diagram for the new graphene-plasmonic MM (G-PMM) with a three-layer substrate comprises of Si/SiO₂/C and the CSRRs are deposited on the metasurface with the interparticle distance same as prior MM. For graphene sheet with the thickness of 0.35 nm, using the proposed mechanism by random-phase approximation (RPA) method, the complex conductivity of graphene can be defined by ($\sigma_g(\omega)$):

$$\sigma_g(\omega) = \frac{ie^2 E_F}{\pi \hbar^2 \left(\omega + i\tau^{-1}\right)} + \frac{e^2}{4\hbar}\left(\theta\left(\hbar\omega - 2E_F\right) + \frac{i}{\pi}Log\left|\frac{\hbar\omega - 2E_F}{\hbar\omega + 2E_F}\right|\right) \qquad (3.5.12)$$

where the Fermi energy is defined by E_F and τ is the relaxation time ($\tau = \mu E_F / ev_F^2$), in which v_F is the Fermi velocity (10^6 ms⁻¹), and μ is the relaxation rate with the mobility of 10^4 cm²V⁻¹s⁻¹. In the equation above, the first term characterize the Drude model for heavily doped regions of graphene and also for frequencies below the Fermi energy. Using following equation: $E_F = \hbar v_F \sqrt{\pi|n|}$, we are able to control Fermi energy by electrostatic doping via adjusting charge carrier density (*n*). Herein, we used the proposed method by Fan *et al.* and Shen *et al.*, therefore, by assuming E_F=0.5eV, the complex surface conductivity (*α*) of graphene layer in our numerical studies was set to 58.7 GHzΩ⁻¹, with the relaxation time of exactly τ=5×10⁻¹³s, the permittivity is set to ε_g=2.5, the plasma resonance frequency is 1×10¹⁵ rad/s, and the plasma collision frequency is 5×10¹² rad/s. Figure 5(B) shows transmission spectra for the G-PMM structure in presence of a graphene layer during exposing by a transverse polarization mode (*φ*=0°). In this regime, two distinct and pronounced minima are appeared at *f*=1.70 THz and 3.25 THz. Obviously, a dramatic blue-shifted is performed in the position of both Fano dips to the shorter frequencies that is indicated inside the profile (compared in the profile for the presence and absence of graphene monolayer). This behavior of Fano resonant modes was originated from the high amount of power that is absorbed and accumulated due to the effect of graphene surface at shorter frequencies (*f*=1 THz-3 THz) and also, high absorptive Ag-CSRRs with ohmic losses. To understand the effect of the thin graphene layer on the absorption efficiency, we plotted the numerical results for the absorption spectra in Fig. 3.5.19(c), where a remarkable enhancement in the absorption percentage is performed (*A*(%)=62% at the highest peak position) at the declared Fano dip frequencies with a broadband property due to the presence of graphene. The inset shows the real and imaginary parts of permittivity and refractive index for the utilized graphene monolayer at THz frequencies. Accordingly, the maximum absorptive behavior of graphene can be performed in short THz frequencies (our results are in agreement with these profiles). Figures 3.5.19(D) and (E) exhibit the plasmon resonance excitation and localization in Ag-CSRRs and G-PMM by two-dimensional simulation snapshots at both Fano resonant frequencies. Comparing the latest snapshots with the earlier MM's simulation results, the effect of graphene sheet on the plasmon resonance localization and absorption is highly significant, and for the graphene-based configuration, we observed an EM field confinement in the offset spaces between Ag-CSRRs.
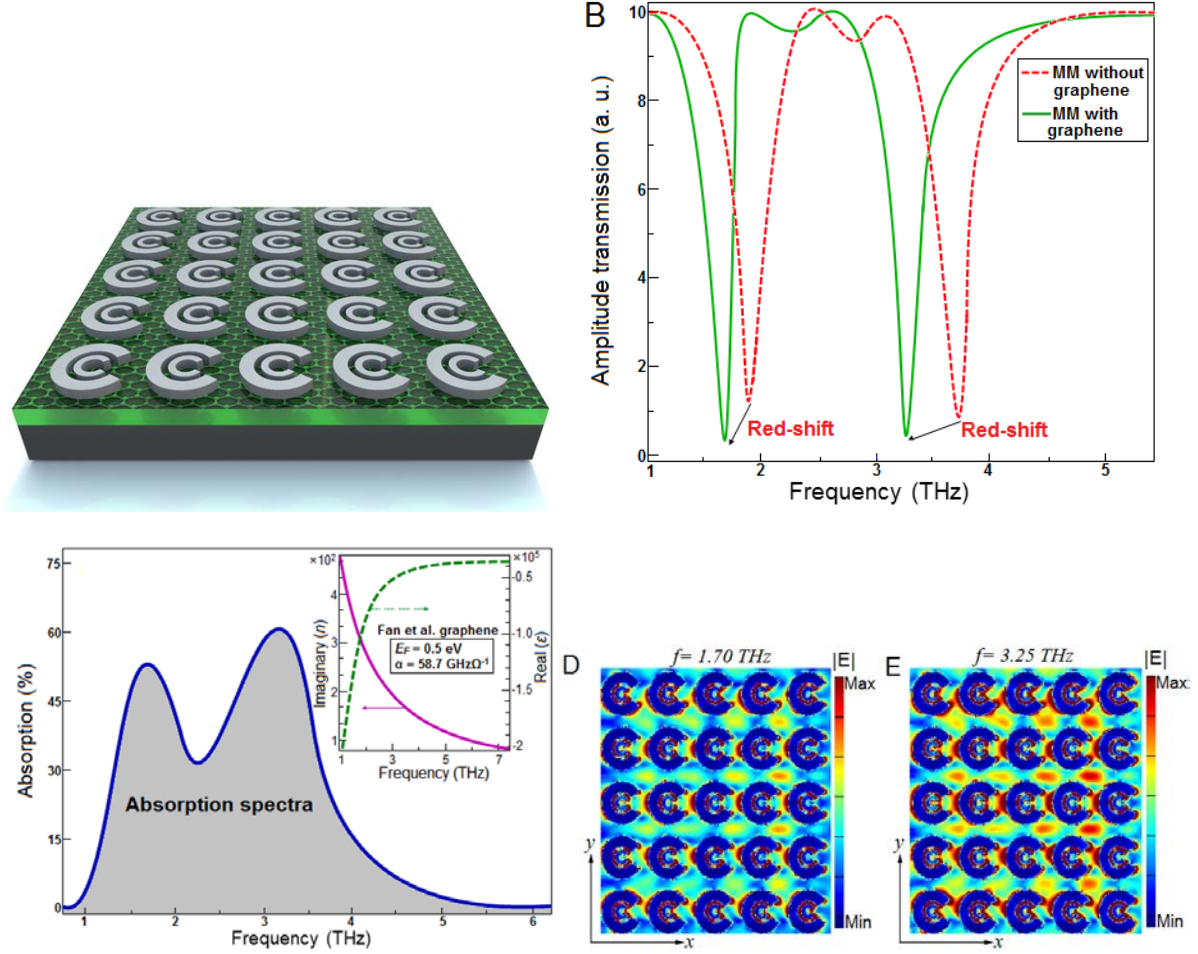
Figure 3.5.19: A) Schematic illustration of the G-PMM composed of Ag-CSRR units deposited on a multilayer metasurface consists of monolayer graphene@SiO$_2$@Si, B) amplitude transmission profile for the G-PMM includes comparison with the plasmonic MM for the position of Fano dips positions, C) absorption spectra for the G-PMM with broadband property. The inset shows the imaginary and real parts of refractive index and permittivities for the Fan *et al.* graphene in THz regime, D, E) two-dimensional *xy*-view snapshots for plasmon resonance excitation and coupling in a G-PMM for two different THz frequencies correlating with the Fano resonant modes.

Having discussed the effect of physical characteristics of graphene layer on the plasmon response of a G-PMM, we now begin our comparison of the optical properties of the proposed MM during employing different types of graphene monolayer based on experimentally obtained results. To this end, we applied three-different graphene sheets under the Ag-CSRR arrays to extract the transmission and absorptance profiles numerically. Papasimakis *et al.* have proposed a type of graphene with the dissipative loss of 33.4 Ω, and the dynamic conductivity was α=5.93×10^{10} Ω^{-1}s^{-1} and γ=1.98×10^{12} s^{-1}. Yan *et al.* have proposed different type of measurements for highly doped graphene and corresponding parameters were defined as: α=7.6×10^{10} Ω^{-1}s^{-1} and γ=9.8×10^{12} s^{-1}, with the dissipative loss as 129 Ω. The final data for graphene layer that we utilized here was obtained by Li *et al.* as α=1.99×10^{10} Ω^{-1}s^{-1} and γ=29.4×10^{12} s^{-1} with a noticeable dissipative loss factor as 1477 Ω. Figure 3.5.20(A) shows the absorption profile as a function of incoming

frequency during chemical modifications in the monolayer graphene for three different settings for graphene sheet by Papasimakis *et al.*, Yan *et al.*, and Li *et al.*. Obviously, by increasing the dissipative lossy component (ohmic loss), the absorption coefficient is increased dramatically and for the G-PMM with Li *et al.* graphene layer, we defined the absorption percentage as approximately $A(\%) \sim 67\%$. Nevertheless, a dramatic blue-shift to the shorter spectra in the position of absorption extremes is performed due to the absorptive behavior of graphene at short THz regime. To understand the effect of chemical variations in the graphene layer, we plotted the transmission amplitude spectra as a comparative diagram (see Fig. 3.5.20(B)), and by increasing the dissipative losses of graphene sheet, a substantial red-shift in the position of Fano dips is recorded (sharper dip at $f=3$ THz for Li *et al.* graphene). In addition, it should be underlined that during the red-shift, the Fano resonant dips become sharper and deeper. Figure 3.5.20(C) contains three simulation E-field maps of the proposed G-PMM for three different kinds of graphene sheets at the Fano dip frequencies (The accumulation of incident THz wave for the MM with Li *et al.* graphene is obvious in the snapshot).
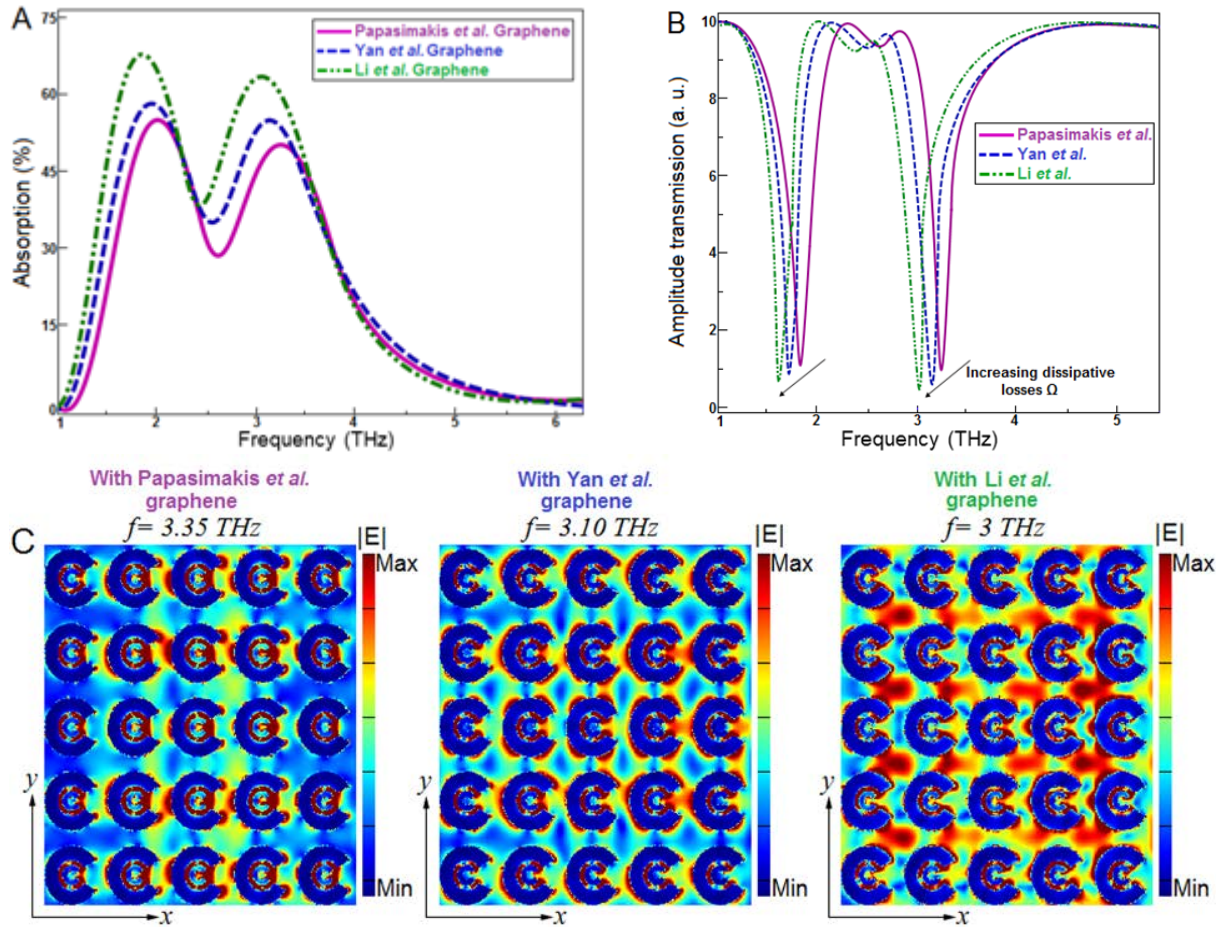

Figure 3.5.20: A, B) Absorption and transmission spectra for three different graphene sheets (based on achieved data by different researchers for graphene analytically and experimentally) that are utilized in designing the G-PMM. C) E-field maps of the proposed G-PMM for three different kinds of graphene sheets at the Fano dip frequencies.

Let us proceed to examine the polarization-dependency of the proposed MMs in different regimes. This feature can be utilized in designing ultrafast THz Fanoswitches and many other applications that are highly sensitive to the polarization angle of the incoming light. In all of the prior simulations, we utilized a THz wave to illuminate the MMs with an incidence angle of $\varphi=0°$ (Transverse polarization mode: *T*-mode), and almost perfect absorption was happened for this polarization with a minor percentage of reflection. For the incident spectrum (THz wave) with the polarization angle of $\varphi=0°$ (Longitudinal polarization mode: *L*-mode), we expect an oppose behavior which means disappearing of Fano dips and reducing the absorption coefficient and as a results increasing the reflectance. Technically, due to presence of antisymmetric Ag-CSRR units, a strong polarization-dependency is expected for all of the MMs with or without graphene sheet. In terms of structural properties, the split angle plays fundamental role here to realize desired polarizations-dependency. For the incoming THz wave with *T*-mode, the split area is in transverse condition during light-matter interaction that encourages formation of strong dark modes in the microstructure (according to PIT mechanism), therefore, sharp Fano dips were performed in transmittance profiles. Increasing the polarization angle from $\varphi=0°$ to $90°$ will help us to understand the polarization-dependency by plotting the transmission spectra for the MM. Figures. 3.5.21(A) and (B) show the polarization angle variations ($\varphi=0°$, 30°, 45°, 60°, and 90°) for the plasmonic MM without graphene sheet in metasurface and a G-PMM with Li *et al*. graphene under Ag-CSRR arrays. Obviously, for both of the structures, increasing the polarization angle gives rise to disappearing of Fano dips, and finally, for the *L*-mode ($\varphi=90°$) Fano dips are completely disappeared and a high quality transmission is revealed for plasmonic MM, and for the G-PMM, small and shallow dips remained due to presence of graphene layer in the multilayer metasurface. As a specific case, for graphene-based MM, the small percentage of absorption is negligible in practical applications that can be assumed as a loss factor for switching applications.
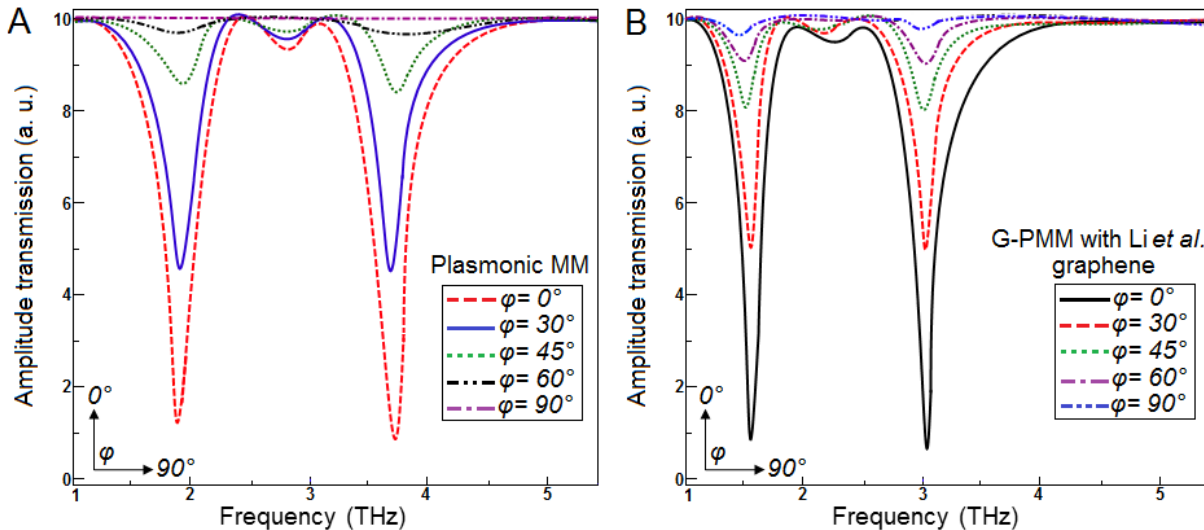

Figure 3.5.21: A, B) Amplitude transmission spectra for both plasmonic MM and G-P MM (with Li *et al*. graphene) during variations in the incident polarization angle (φ), respectively.

In conclusion, we have developed highly efficient plasmonic MMs that are able to operate ultrasharp Fano resonant modes in THz frequencies. Employing Ag-CSRR structures in periodic arrays along *x* and *y* directions that are deposited on a multilayer metasurface, we extracted the effective components for the proposed MM in THz regime by plotting the transmission profile and quantifying the absorption coefficient. The antisymmetric orientation of CSRRs allows for supporting strong Fano resonant modes via interference of dark and bright modes generated during light-matter interactions. Then, we enhanced the absorptance coefficient with the placement of a thin monolayer graphene sheet under the metallic structures and above the metasurface to use its broadband feature in optimizing the performance of the plasmonic THz-MM. Modifications in the chemical features of the graphene sheet substrate provide a method to improve the Fano resonant dips quality and absorption coefficient based on theoretically and experimentally achieved data for graphene by different research groups. Ultimately, we changed the polarization angle of the incident light from the transverse to the longitudinal mode to examine the polarization-dependency of the structure. It is shown that by increasing the size of the polarization angle, both of the Fano dips disappeared in the transmission profile. Loosing Fano dips directly led to dramatic decrement in the absorption percentage in plasmonic MM and graphene-based MM and using this mechanism, we verified the strong polarization-dependency of the structure.

3.6 Highly Sensitive Wide Bandwidth Photodetector Based on Internal Photoemission in CVD Grown P-Type MoS₂/Graphene Schottky Junction

Graphene, a semi-metallic, two-dimensional (2D) material with a single atomic thickness has been the most widely researched material owing to its superior electrical, mechanical and optical properties such as high carrier mobility ($\approx 200, 000$ cm^{2}V^{-1}s^{-1}), high mechanical strength, flexibility, transparency, and high absorption rate (2.30% of incident light per each layer) among many other properties. Further, gapless nature of graphene enables charge carrier generation over a wide energy spectrum from ultra violet (UV) to terahertz (THz) making it a unique material for photonics and optoelectronics during the recent past. Making use of the unique capabilities of graphene, many studies have been performed over the past decade to demonstrate highly efficient graphene photodetectors (GPDs) from visible to infrared (IR) range. Despite the many favorable properties, factors such as low absorption due to single layer nature of graphene limited the responsivity of conventional GPDs to few tens of mAW^{-1}. Alternative methods such as colloidal quantum dots, microcavities or plasmonic nanostructures have been used to improve the responsivity of the GPDs but these devices were found to respond to very limited wavelengths of light. On the other hand, 2D semiconductor transition metal dichalcogenides (sTMDs) materials have also been widely used for photodetector applications. Atomically thin sTMDs provide a wide range of advantages in optoelectronics when compared to their bulk counterparts owing to their high transparency, flexibility and tunable bandgap. In particular, MoS₂ is a unique semiconductor material whose bulk counterpart has an indirect-gap of 1.20 eV but when reduced to a monolayer, it changes into direct bandgap material with a bandgap of 1.80 eV due to quantum confinement. This results in higher absorption coefficient and efficient electron-hole pair generation under photo excitation in monolayer MoS₂. A 10^4 fold enhancement of luminescence quantum yield for monolayer MoS₂ compared with bulk MoS₂ has been observed. There are several reports on the fabrication of MoS₂ based photodetectors. The first phototransistor based on monolayer MoS₂ showed a relatively poor photo responsivity of 7.50 mAW^{-1}. Choi *et al*. used multilayer MoS₂ to achieve 100 mAW^{-1} photo responsivity, showing an improvement over the first phototransistor but

still low compared to GPDs. Since then, much progress has been made and more recently, phototransistors with responsivities ranging from few hundreds of mAW^{-1} to hundreds of AW^{-1} were reported. However, the reported MoS$_2$ based photodetectors are limited by narrow wavelength range and long response times.

To further improve the properties of graphene and MoS$_2$-based photodetectors, it is imperative to design new device structures like composites, heterostructures or functionally graded thin films. Numerous efforts have been made to combine the properties of TMDs and graphene by assembling graphene with other 2D crystals to create multifunctional high-performance hybrid devices. One of the hybrid structures includes the combination of graphene and MoS$_2$ in the form of thin film heterostructures. Coupling graphene with MoS$_2$ can produce a hybrid material that can utilize the high photon absorption capability in MoS$_2$ and high electron mobility in graphene to realize a highly efficient photodetector as shown by Wenjing Zhang *et al* who have achieved a high responsivity of 1.2 x 10^7 A/W by applying a gate voltage of -10 V at 690 nm laser illumination by simply stacking n-type monolayer MoS$_2$ over graphene. In the present study, we assembled few layers of graphene with few layers of *p*-type MoS$_2$ to form a simple MoS$_2$/graphene Schottky junction photodiode. We found that *p*-type MoS$_2$ provides a much lower Schottky barrier height with graphene with a broad spectral range of detection.

Fabrication of MoS$_2$/Graphene Junction

MoS$_2$/graphene junction devices were fabricated by growing atomically thin MoS$_2$ film on Si/SiO$_2$ substrates followed by the transfer of graphene. For MoS$_2$ deposition, the first step involves the sputtering of Mo thin films on (100) oriented *n*-type (As doped, resistivity < 0.005 Ω.cm) silicon substrates coated with 300 nm thick SiO$_2$ layer. High purity (99.99%) Mo metal target of 50 mm diameter was used for sputtering Mo thin films. In second step, magnetron sputtered Mo/SiO$_2$/Si films were subsequently placed in a low-pressure chemical vapor deposition (LPCVD) system (Graphene Square CVD) and sulfurization was proceeded at 600°C for 30 min. The detail of MoS$_2$ synthesis can be found in our recent report. Polycrystalline copper foils (Nimrod Hall, 99.9% purity, 25μm thick) was used as the substrates for graphene growth. The Cu foil was electro-polished using a home-built electrochemistry cell followed by rinsing in methanol and deionized water solution (1:1), and then gently blown with compressed nitrogen for drying. The cleaned Cu foil was loaded into the low-pressure thermal CVD system. The reaction chamber was evacuated to ~0.1 mTorr and refilled with 2.5 sccm of pure H$_2$. The temperature was increased to 1000^{0}C within 40 min and then annealed for 1 h. After annealing, 20 sccm of CH$_4$ and 2.5 sccm of H$_2$ were introduced into the chamber for graphene growth at 1000^{0}C under the pressure of 5 Torr for a certain growth time. After the growth, the CH$_4$ flow was turned off and the chamber was cooled down under H$_2$ environment. The graphene transfer method used was as follows: (1) PMMA (MicroChem Corp. 495 PMMA A2) solution was spin-coated onto the graphene/Cu foil at 5000 rpm for 1 min, followed by drying the sample in the air; (2) the Cu foil was etched with metal etchant (type I, Transene company, INC.), resulting in the PMMA/graphene film floating to the top of the etchant solution; (3) the PMMA/graphene film was washed in a beaker containing deionized water, and floated on 10 % HCl solution for 10 min, and transferred to a beaker with deionized water for another wash (done 3×); (4)the film was transferred to a beaker with deionized water for another wash and this process was repeated three times; (5) the film was then finally scooped onto a Si/SiO2/MoS$_2$ substrate with the PMMA side up and dried in the air; (6) the PMMA layer was removed by immersing the sample in a large volume of acetone; (7) the sample was

dried with compressed nitrogen. Figure 3.6.1a shows the schematic of the MoS_2/graphene photodetector device structure simply formed by a manual stacking of a graphene onto MoS_2. 50 nm thick Au/Ti metal contacts were deposited by electron beam evaporation after using a shadow mask. The shadow masks were carefully prepared using a laser writer so as to maintain the contact area and position accurately. The deposited contacts were later annealed at 350^0C for 30 minutes.

Structural & Electrical Characterization

Figure 3.6.2a shows the schematic of the studied photodiode. Sputtering-CVD technique was used to synthesize few layers of MoS_2 as described by Choi *et al.* while CVD process is used to synthesize graphene. Figure 3.6.2b shows the optical microscope image depicting the color contrast over the four different regions; (1) SiO_2 (2) MoS_2 (3) Graphene and (4) MoS_2/graphene junction (MGJ). Atomic force microscopy (AFM) was used to study the thickness and the interface of MoS_2 and graphene. Figures 3.6.2c and 3.6.2e show the thickness measured using AFM. We observed that the average thickness of MoS_2 layer is 2 nm and that of graphene is 5 nm, which suggests that as grown MoS_2 was about 3-4 layers thick. Raman spectroscopy is a widely used method to determine the number of layers, quality and defects present in these 2D materials.
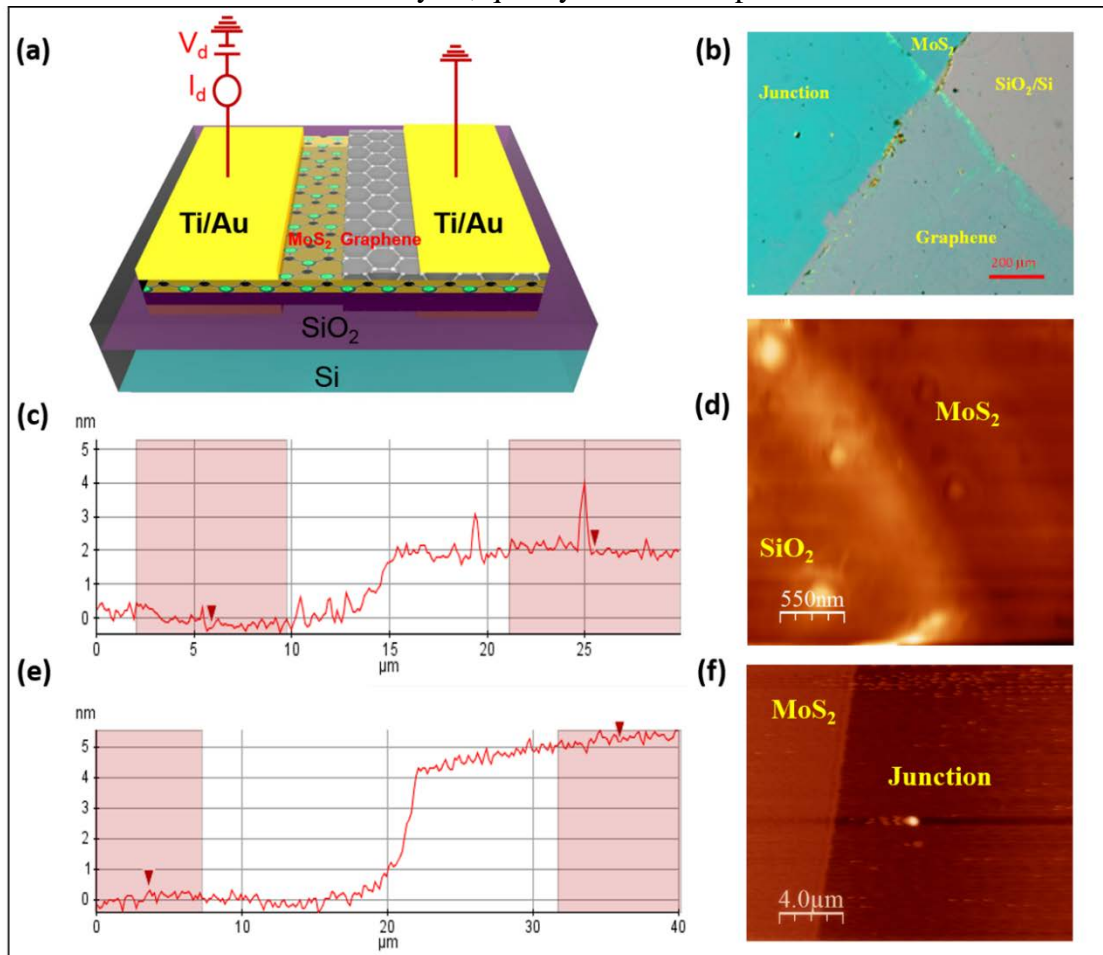

Figure 3.6.2. (a) Schematic of p-type MoS_2/graphene junction device (b) Optical image of MoS_2/graphene junction with individual areas clearly visible (c) AFM height profile showing height of MoS_2 (d) AFM image of MoS_2-SiO_2 interface (e) Thickness of graphene at MoS_2/graphene junction (f) AFM image of MoS_2/graphene junction

Figure 3.6.3a shows the Raman spectra of MoS_2 and graphene, measured over SiO_2 and junction regions using a 532 nm excitation laser line. We observed strong peaks at 379.77 cm^{-1} and 403.52 cm^{-1} corresponding to the in plane E^1_{2g} mode and out-of-plane A_{1g} mode of MoS_2, respectively. The peak frequency difference of 23.75 cm^{-1} between the two modes indicates that as grown MoS_2 is 4-5 layers thick, which is in agreement with the previously reported results and also with our results obtained by AFM height analysis. Raman spectra of graphene on SiO_2 evident the formation of 2D and 'G' characteristics peaks at 2666.83 cm^{-1} and 1580.16 cm^{-1}, respectively, which is consistent with the previous reports on few layer graphene. However, a red peak shift of $\approx$3.8 cm^{-1} was observed in the 2D peak of graphene when Raman spectra was taken at the junction. The observed peak shift could be attributed to an increase in hole concentration at the MoS_2/graphene junction. This is a common phenomenon for p-type semiconductor-metal Schottky junction where holes travel from the p-type semiconductor to metal as their Fermi levels are aligned. Figure 3.6.3b shows photoluminescence (PL) spectrum measured at room temperature. Peak 'A' associated with excitonic transitions at the 'K' point of Brillouin zone is observed at 1.85 eV while peak 'I' at 1.40 eV corresponding to indirect gap which is prominent in bulk MoS_2 is almost negligible confirming that the fabricated device is formed by few layers of MoS_2. We also observe a strong emission at 1.75 eV which has been attributed to radiative recombination of neutral excitons bound to defects (X^0) caused by Sulfur (S) vacancies.

The conduction behavior of MoS_2 films deposited on Si/SiO_2 substrates was determined by fabricating field effect transistor (FET) devices with 50 nm thick Au as source and drain electrodes, 300 nm thick SiO_2 served as the dielectric layer, while doped silicon was used as the back gate. The output and transfer characteristics of our MoS_2 FET confirms a p-type conduction behavior with a field effect mobility of $\approx$12.24 cm^{2}V^{-1}s^{-1} which is higher than mechanically exfoliated and CVD grown MoS_2 FETs on Si/SiO_2 substrates and $I_{on/off}$ ratio of $\approx$10^6. The origin of p-type conduction in MoS_2/SiO_2 system is not known yet, however, Douli et al. in their studies showed that a p-type conduction in MoS_2 films on SiO_2 substrates could be due to the presence of localized trap states arising from impurities or defects within the oxide substrate or at the interface with the conducting channel, can redefine the effective Fermi level of the hybrid system to make it either n-type or p-type. The trap states might have originated from the immobile ionic charges, SiO_2 surface oxygen dangling bonds or foreign impurities presented at the SiO_2/MoS_2 interface during MoS_2 synthesis. The defects present at the SiO_2 and MoS_2 interface could also be due to the Mo diffusion into SiO_2 when it was sulfurized in the CVD furnace at the high temperature of 600 °C.
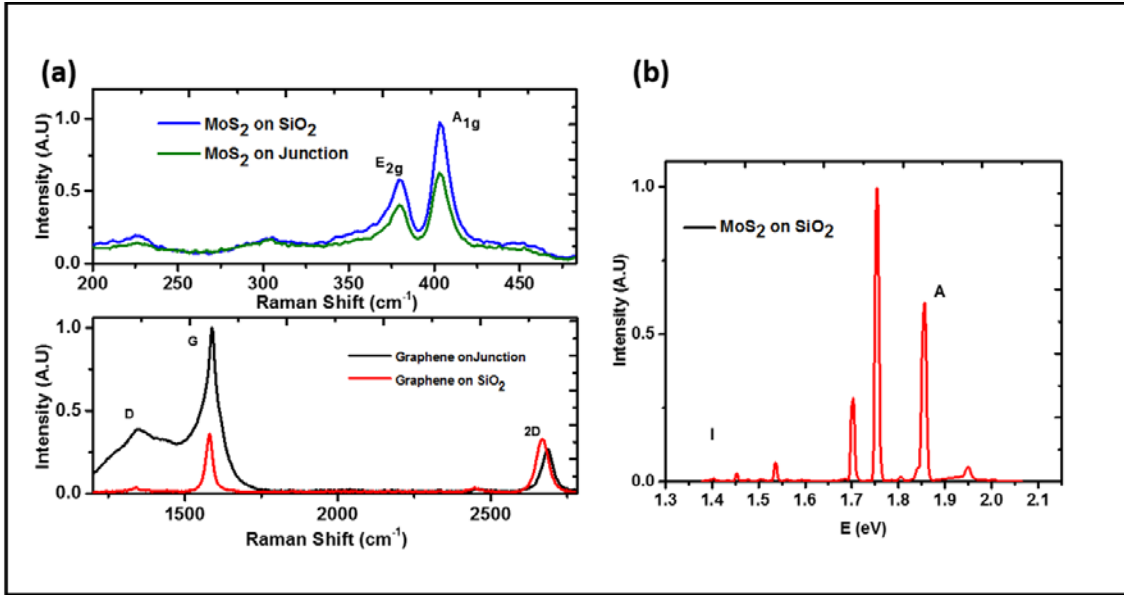
Figure 3.6.3. (a) Raman spectrum of MoS₂ and Graphene on SiO₂ and junction (b) Photoluminescence of MoS₂ on SiO₂ showing sharp peaks at 1.7, 1.75 and 1.85 eV, and smaller ones at 1.4 and 1.55eV.

When a semi-metallic graphene is assembled over semiconducting MoS₂ a Schottky junction like behavior is expected. The schematic of carrier transport at MoS₂/graphene junction under forward and reverse bias is shown in Figure 3.6.4a. In Figure 3.6.4b the current-voltage (J-V) characteristics measured at MoS₂/graphene is displayed. As can be seen from the J-V plot and the |log (J)| vs. V plot shown in the inset, the junction shows a clear rectification as exponentially increasing current passes in the forward bias while there is strong resistance in the reverse bias which prevents flow of holes from graphene to MoS₂. From the current-voltage and the Raman measurement results showing an influx of holes in to graphene from MoS₂ at the junction, it can be concluded that a Schottky barrier junction (SBJ) similar to a metal-semiconductor junction is formed between graphene and MoS₂. However, we observe that the current never reaches a complete saturation in reverse bias unlike an ideal metal-semiconductor Schottky junction. This is due to the bias dependent Fermi level observed in graphene which results in a variable Schottky barrier height (SBH) at different bias voltages. Recently Tongay *et al*. have proposed a model for the current observed in graphene – semiconductor junctions taking into account the change in graphene Fermi level with applied bias. The current in the Schottky diode is given by

$$J(V) = A*T^2 \exp(-\frac{e\Phi^0{}_{SBH} + e\Delta\Phi_{SBH}(V)}{k_BT})[\exp(\frac{eV}{k_BT}) - 1] \qquad (3.6.1)$$

Where $A*$ is Richardson's constant, $\Phi^0{}_{SBH}$ is Schottky barrier height (SBH) at zero bias and $e\Delta\Phi_{SBH}(V)$ is the difference in Schottky barrier height due to change in the Fermi level of Graphene with applied bias and is given by

$$e\Delta\Phi_{SBH}(V) = -(\Delta E_F^G(V)) = \hbar V_F[\sqrt{\pi(n_0 - n_{induced})} - \sqrt{\pi n_0}] = -\frac{1}{2}\hbar v_F\sqrt{\frac{\pi\varepsilon_s\varepsilon_0 N_A(V_0 + V_R)}{2en_0}} \quad (3.6.2)$$

where N_A is acceptor concentration in the semiconductor, V_0 is the built-in voltage, V_R reverse bias voltage and n_0 the carrier density in graphene. The modified saturation current is

$$J_s(V) = A^*T^2 \exp(-\frac{e\Phi_{SBH}^0 + e\Delta\Phi_{SBH}(V)}{k_B T}) \quad (3.6.3)$$

Zero bias Schottky barrier height (Φ_{SBH}^0) was measured from the temperature dependent J-V measurements carried at four different temperatures and capacitance- voltage (C-V measurements were used to measure acceptor concentration N_A and built in voltage V_0. The change in current ($|J|$) with temperature is shown in Figure 4c which shows that the current increases with temperature in both bias directions. The value of Φ_{SBH}^0 can be obtained from the slope of Richardson's plot given by

$$\Phi_{SBH}^0 = \frac{V_1}{n} - \frac{k}{q}\frac{\partial[\ln(I/T^2)]}{\partial(1/T)} \quad (3.6.4)$$

We measured the Φ_{SBH}^0 of MGJ at $V_1 = 0.3$ V to be 139.20 meV where the ideality factor 'n' is obtained from intercept of the linear region of the *J-V* plot and measured to be 1.86 while Richardson's constant A* is 0.70 x 10^{-6} A cm^{-2} K^{-2}. The greater than unity value of the ideality factor can be attributed to enhanced image-force lowering across the MGJ and Schottky-barrier inhomogeneity. Capacitance-Voltage measurements are used to obtain built – in voltage (V_0) and doping density values, from Schottky-Mott relationship. When square of inverse of capacitance ($1/C^2$ (cm^{4}F^{-2})) plotted against applied voltage in reverse bias, ($1/C^2$) varies linearly with applied bias before saturating this can be extrapolated to intersect the abscissa to obtain built-in potential $V_0 = (\Phi_{MoS_2} - \Phi_{Gr})$ and the slope of the linear region gives the doping density (N_A) of MoS$_2$. From Figure 3.6.4d we can see that the measured values hold the linearity in reverse bias. We measured V_0 and N_A values to be 280 mV and 6.64 x 10^{21} cm^{-3} (3.32 x 10^{15} cm^{-2}) respectively. By considering the work function of graphene from literature to be 4.50 eV, the work function of *p*-type MoS$_2$ is found to be 4.78 eV. Experimental and theoretical values of reverse current obtained from the analytical model developed shown in Figure 4e closely match each other.
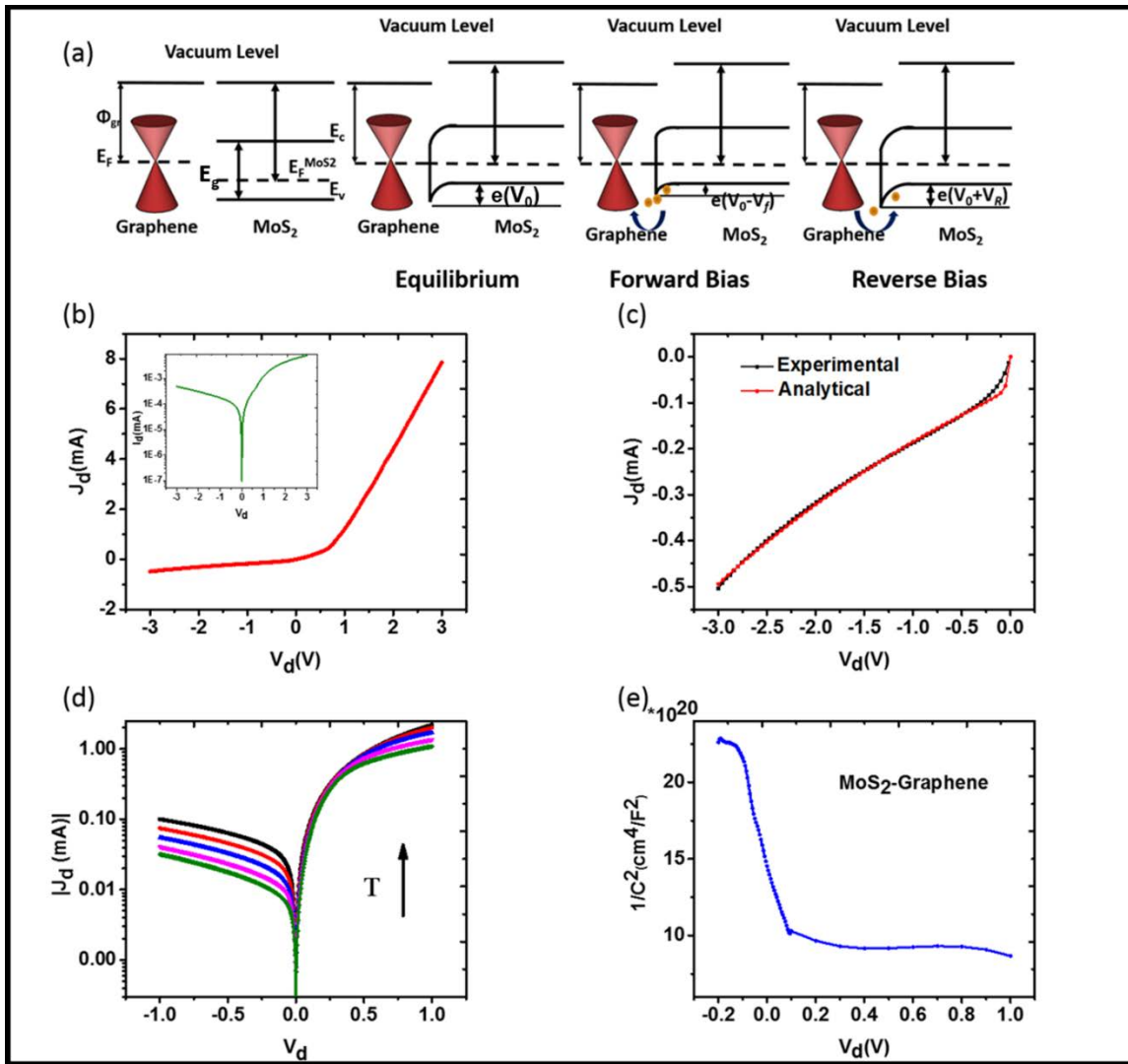
Figure 3.6.4 (a) Energy level alignment for MoS_2/ graphene structure, band diagram at junction in equilibrium, forward bias and reverse bias with carrier flow (b) J-V curve showing rectification under reverse bias and exponentially increasing current in forward bias (inset: Absolute value of J-V plotted in logarithmic scale) (c) J-V at different temperatures showing an increase in J with increase in temperature (d) $1/C^2$ plotted against voltage (e) Reverse current from experimental and analytical model

MoS_2/Graphene Photodetector

One of the most interesting application of Schottky diodes is their use as photodetectors. MoS_2/graphene hybrid structure would be an excellent material for photo-detection as both materials show high photosensitivity. Graphene being a gapless material exhibits sensitivity to light over a wide range of wavelengths from visible light to mid and far infrared. High electron mobility and high absorption would also contribute towards high responsivity in graphene. On the other hand, atomically thin MoS_2 has shown some interesting optical phenomenon such as 10^4 fold increase in photoluminescence when compared to bulk MoS_2 and significant responsivity in visible light. By Stacking both MoS_2 and graphene together to form Schottky junction, we would be able to harness these features of both materials to build high performing photodetectors. In general Schottky photodiodes operates in two modes: (1) Energy gap excitation where electron-hole pairs

are generated by band to band excitation in the semiconductor when energy of photon is greater than the band gap of semiconductor $hv > E_g$ and (2) Internal photoemission which is observed when the incident light energy is greater than the Schottky barrier energy and smaller than the bandgap of semiconductor $(\Phi_{SBH} < hv < E_g)$ resulting in photo emission of carriers from metal surface close to the junction which are then driven towards the semiconductor over the Schottky barrier due to the electric field in the junction. This leads to a wide spectral range of detection based on the SBH values obtained. Both schemes are explained in figure 5b. A Schottky barrier photodiode is conventionally operated in reverse bias where the increase in barrier results in very small reverse current and hence any increase in current by the photocurrent can be detected with a high sensitivity. This makes it easy to exactly measure the photocurrent generated. The expression for diode current is given by

$$J(V) = A*T^2[\exp(\frac{eV}{k_BT}) - 1] - J_{op} \qquad (3.6.5)$$

where J_{op} is the photon induced current equal to $R*P_{op}$ where R be the responsivity of the photodiode and P_{op} is the power of incident light, the first part of the equation is the current equation in ideal Schottky diode. By replacing the diode current term with the modified Schottky diode current presented in equation (3.6.1), we can write the diode current equation as

$$J(V) = A*T^2 \exp(-\frac{e\Phi^0_{SBH} + e\Delta\Phi_{SBH}(V)}{k_BT})[\exp(\frac{eV}{k_BT}) - 1] - J_{op} \qquad (3.6.6)$$

In order to study the operation of the photodiode in both modes we have studied the performance of the device in a wide spectral range from 400 nm to 1500 nm. The spectral response 'R' of the device measured at 2 V reverse bias is shown in figure 4d. When the diode is operated in energy gap excitation mode where $hv > E_g^{MoS_2}$ a maximum photo responsivity of $R_{max} = 0.52$ AW^{-1} is observed at 590 nm. Beyond 670.00 nm, where the incident photon energy is smaller than $E_g^{MoS_2}$ the photo current is due to internal photo emission in Graphene where photo generated holes move towards MoS$_2$. We find that the responsivity actually increases from 980 nm reaching a maximum value of 1.26 AW^{-1} at 1440 nm before starting to fall. The obtained responsivity is not the highest but higher than many state of the art devices. A comparison of the MoS$_2$/graphene photo detectors is provided in table 1 of supplementary data. This increase in responsivity follows the increase in photoconductivity observed in graphene which is shown in Figure 3.6.5 (e). This kind of increased optical conductivity in graphene has been observed in intra band conductivity in earlier studies.
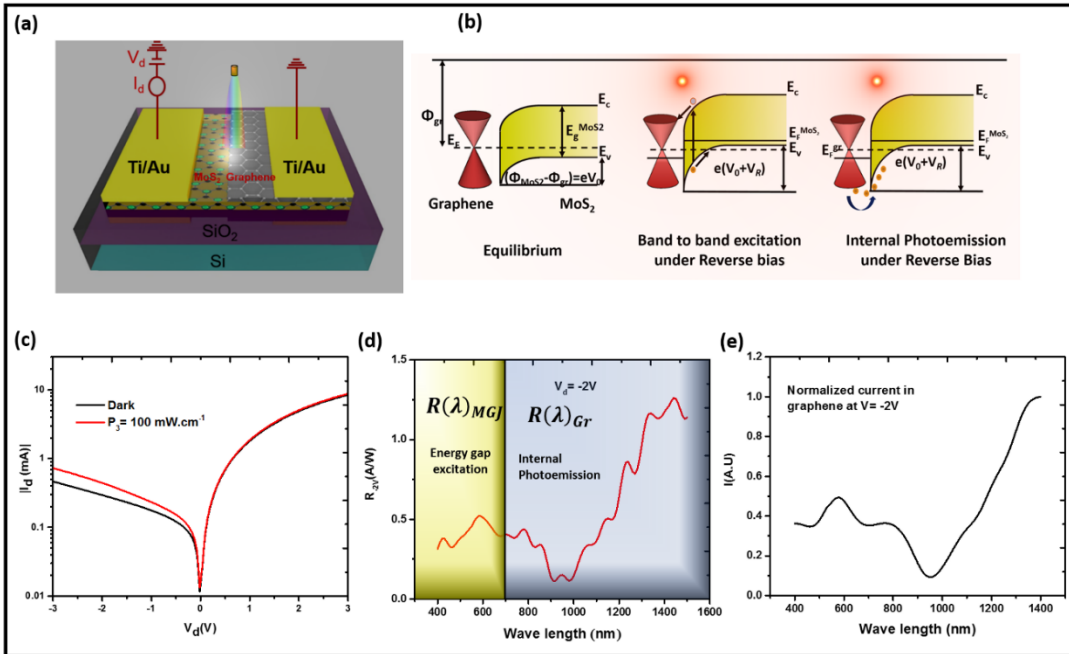
Figure 3.6.5: (a) MGPD under illumination (b) Illustration of photocurrent generation in a Schottky diode under illumination (c) J-V at dark and under 100 mW/cm^2 illumination (d) Photo responsivity of MGPD at different wavelengths (Spectral Response) (e) Photoconductivity of graphene.

One of the most important detector characteristics is the noise equivalent power (NEP) which represents the lowest input power giving a unit signal/ noise ratio. In a Schottky junction photodetector, both Johnson noise which is due to thermal noise associated with the resistance and shot noise which is associated with the overall current contribute towards the overall noise. The Johnson noise current i_j is given by $i_j = \sqrt{\dfrac{4kBT}{R_{eq}}}$ where k is the Boltzman constant, T is the absolute temperature and R_{eq} is the equivalent resistance. The R_{eq} is obtained from the slope of I-V of MGPD at -2 V measured in dark. For R_{eq} of 5.83 MΩ and for normalized bandwidth (B) at room temperature the Johnson noise i_j is 1.68 pA. The shot noise is given by $i_s = \sqrt{2q(I_{ph} + I_d)B}$ where I_{ph} is photo current and I_d is dark current. The measured shot noise current at -2V is 11.2 pA at 1400 nm. The total noise current i_n is 11.3 pA and the NEP which is the ratio of i_n and the responsivity is calculated. We obtain a minimum NEP of 7.8 x 10^{-12} W/√Hz and corresponding detectivity of 4.2 x 10^{10} cm.√ Hz/W at 1400 nm. The measured NEP of MGPD is less than typical Si photodetectors.

Characterization Tools: Atomic force microscopy (Parks NX-10) and Raman spectroscopy (Bay Spec spectrometer) were employed to measure the thickness of MoS$_2$ and graphene layers. In order to determine the conduction in MoS$_2$, electrical measurements were performed at room temperature using an Agilent B2912A precision source/measure unit (2 ch, 10 fA, 210V, 3A DC/10.5A Pulse) connected to a probe station with 20µm size tungsten probes. Room temperature photoluminescence (PL) using He-Cd laser line at 325 nm and 10 mW laser power and visible

spectroscopy were employed to characterize the quality of MoS$_2$/graphene heterostructure. Spectral response measurement system QEX10 from PV Measurements Inc. which houses a Xenon arc lamp was used to measure the spectral response of the MoS$_2$/graphene photodetectors. The optical power of the xenon lamp at different wavelengths was measured using multifunction optical meter from Newport. The responsivity of the MGPD was calculated by taking the ratio of photocurrent density and power density at every 10 nm between 400 nm and 1500 nm.

In conclusion, we succeeded in fabricating a high bandwidth photodetectors by stacking few layers of p-type MoS$_2$ over few layers of graphene to form Schottky junction photodiode. Stable optical properties of MoS$_2$ and high carrier mobility in graphene contribute to efficient charge separation at the junction. Apart from the impressive charge carrier properties, graphene also exhibits a wide bandwidth absorption which allows for the photodiode to operate in both energy gap excitation mode and internal photo emission mode, there by extending the detection range to higher wavelengths which is not reported in earlier MoS$_2$/graphene Schottky junctions. From the spectral response, we find that the fabricated device performs well over a wide range of wavelengths from visible region to mid infrared region with internal photo emission in graphene playing a major role in extending the range of the device. We have studied the junction characteristics and presented the underlying phenomenon of charge transfer in 2D MoS$_2$/graphene Schottky junction. CVD process is used in growing large area MoS$_2$ and graphene which along with the simplicity of fabrication can be easily integrated with metal oxide semiconductor (CMOS) technology.

4. List of the Publications and Presetnations

4.1 Papers Published in Peer-Reviewed Journals

1. M. Karabiyik, C. Al-Amin, and N. Pala, "Graphene-Based Periodic Gate Field Effect Transistor Structures for Terahertz Applications", Nanoscience and Nanotechnology Letters, Vol. 5, 754–757, 2013

2. M. Karabiyik, C. Al-Amin, and N. Pala, "Deep Sub-wavelength Multimode Tunable In-Plane Plasmonic Lenses Operating at Terahertz Frequencies", IEEE Transactions on Terahertz Science and Technology, Vol. 3, Issue: 5, pp.1-8 (2013) DOI: 10.1109/TTHZ.2013.2273415

3. C. Al-Amin, M. Karabiyik, R. Sinha and N. Pala, "Improving High Frequency Characteristics of Graphene FETs by Field Control", IEEE Electron Device Letters, Vol. 34, Issue: 9, pp.1193-1195 (2013) DOI: 10.1109/LED.2013.2272071

4. S. Das, D. Lahiri, D.-Y. Lee, A. Agarwal, W. Choi, "Measurements of the adhesion energy of graphene to metallic substrates", Carbon, 59, pp. 121-129 (2013) doi:10.1016/j.carbon.2013.02.063

5. C. Al-Amin, M. Karabiyik, P.K. Vabbina, R. Sinha, N. Pala, "Field controlled RF Graphene FETs with improved high frequency performance", Solid-State Electronics, Volume 95, Pages 36–41, (2014) doi:10.1016/j.sse.2014.03.003

6. P. K. Vabbina, M. Karabiyik, C. Al-Amin, N. Pala, S. Das, W. Choi, T. Saxena and M. Shur, "Controlled Synthesis of Single-Crystalline ZnO Nanoflakes on Arbitrary Substrates at Ambient Conditions", Particle & Particle Systems Characterization, Volume 31, Issue 2, pages 190–194, (2014) DOI: 10.1002/ppsc.201300208

7. D. Choi, C. Kuru, C. Choi, K. Noh, S. Hong, S. Das, W. Choi and S. Jin, "Nanopatterned Graphene Field Effect Transistor Fabricated Using Block Co-polymer Lithography", Materials Research Letters vol. 2, no. 3 (2014): 131-139. DOI:10.1080/21663831.2013.876676

8. S. Das, M. Kim, J-W Lee and W. Choi, "Synthesis, Properties and Applications of 2-D Materials: A Comprehensive Review", Critical Reviews in Solid State and Materials Sciences, vol.39, no.4, pp. 231-252, (2014) DOI:10.1080/10408436.2013.836075

9. S. Das, D. Lahiri, A. Agarwal and W. Choi, "Interfacial bonding characteristics between graphene and dielectric substrate", Nanotechnology, vol. 25, no.4, p.045707 (2014) doi:10.1088/09574484/25/4/045707

10. P.K. Vabbina, A. Kaushik, N. Pokhrel, S. Bhansali, N. Pala, "Electrochemical cortisol immunosensors based on sonochemically synthesized zincoxide 1D nanorodsand 2D nanoflakes", Biosensors and Bioelectronics, 63 124–130, (2015) doi:10.1016/j.bios.2014.07.026

11. P.K. Vabbina, N. Choudhary, C. Al-Amin, R. Sinha, M. Karabiyik, S. Das, W. Choi and N. Pala, "Highly Sensitive Wide Bandwidth Photodetector Based on Internal Photoemission in CVD Grown Monolayer P-Type MoS2/Graphene Schottky Junction", ACS Appl. Mater. Interfaces, 7 (28), pp 15206–15213, (2015) DOI:10.1021/acsami.5b00887

12. D. Choi , C. Kuru , C. Choi , K.e Noh , S. Hwang , W. Choi , and S. Jin, "Unusually high optical transparency in hexagonal nanopatterned graphene with enhanced conductivity by

chemical doping." Small, vol. 11, no. 26, pp. 3143-3152, (2015) DOI:10.1002/smll.201402784

13. M. Karabiyik, A. Ahmadivand, R. Sinha, C. Al-Amin, P. Kiran Vabbina, S. Kaya, G. Rupper, S. Rudin, M. Shur, N. Pala "Optical Properties of Plasmons in Asymmetric Dual Grating Gate Plasmonic Crystals", Physica Status Solidi (b), Vol. 253, Nr. 4, pp. 605-788 (2016) (Featured on the cover of the issue) doi:10.1002/pssb.201552609

14. C. Al-Amin, P.K. Vabbina, M. Karabiyik, R. Sinha, C. Wang, and N. Pala "Bandgap engineering of single layer graphene by randomly distributed nanoparticles", Journal of Material Science: Materials in Electronics, 2016, doi:10.1007/s10854-016-4722-z

15. Chowdhury Al-Amin , Mustafa Karabiyik, Phani Kiran Vabbina, Raju Sinha and Nezih Pala "Graphene FETs with Low-Resistance Hybrid Contacts for Improved High Frequency Performance", Nanomaterials, 6 (5), 86 (2016) doi:10.3390/nano6050086

4.2 Manuscripts submitted, but not published
1. Sookhyun Hwang, Eunho Cha, Wonbong Choi "Nanoscale probing of phonon-interface scattering in CVD-grown graphene", (in submission)

2. C. Al-Amin, M. Karabiyik and N. Pala, "Fabrication of Graphene Field-Effect Transistor with Field Controlling Electrodes to Improve fT", Microelectronic Engineering, Accepted

3. A. Ahmadivand, R. Sinha, M. Karabiyik, and N. Pala, "Tunable THz Wave Absorption by Graphene-Assisted Plasmonic Metasurfaces based on Metallic Split Ring Resonators", Journal of Nanoparticle Research, Submitted-under review

4.3 Presentations
1. Mustafa Karabiyik ; Chowdhury Al-Amin and Nezih Pala, " Numerical analysis of terahertz plasmonic ring resonators ", Proc. SPIE 8716, Terahertz Physics, Devices, and Systems VII: Advanced Applications in Industry and Defense, 87160I (May 31, 2013); doi:10.1117/12.2016548

2. Chowdhury Al-Amin, Raju Sinha, Nezih Pala, Wonbong Choi, "Novel graphene FETs with field-controlling electrodes to improve RF performance", Proc. SPIE 9083, Micro- and Nanotechnology Sensors, Systems, and Applications VI, 90832W (June 25, 2014); doi:10.1117/12.2050985

3. Phani Kiran Vabbina; Ajeet Kaushik; Kathryn Tracy; Shekhar Bhansali; Nezih Pala, "Zinc oxide nanostructures for electrochemical cortisol biosensing, Proc. SPIE 9107, Smart Biomedical and Physiological Sensor Technology XI, 91070U (May 22, 2014); doi:10.1117/12.2051156

4. Mustafa Karabiyik; Raju Sinha; Chowdhury Al-Amin; Gregory C. Dyer; Nezih Pala; Michael S. Shur, "Dispersion studies in THz plasmonic devices with cavities", Proc. SPIE 9102, Terahertz Physics, Devices, and Systems VIII: Advanced Applications in Industry and Defense, 91020K (21 May 2014); doi: 10.1117/12.2053447

5. Chowdhury Al-Amin, Mustafa Karabiyik, Raju Sinha, Nezih Pala, "Lowering contact resistance of graphene FETs with capacitive extension of ohmic contacts for enhanced RF performance", in Micro- and Nanotechnology Sensors, Systems, and Applications VII, Thomas George; Achyut K. Dutta; M. Saif Islam, Editors, Proceedings of SPIE Vol. 9467 (SPIE, Bellingham, WA 2015), 94672U.

6. Chowdhury G. Al-Amin ; Phani Kiran Vabbina ; Mustafa Karabiyik ; Raju Sinha ; Nezih Pala; Bandgap engineering of graphene decorated with randomly distributed ZnO nano-seed", Proc. SPIE 9836, Micro- and Nanotechnology Sensors, Systems, and Applications VIII, 98362V (May 25, 2016); doi:10.1117/12.2222835.